The International Journal of Robotics Research
0(0):1–37

DOI: 10.1177/02783649261445462
journals.sagepub.com/home/ijr/
SAGE

Grounding the Three-Dimensional Divergent Component of Motion: Geometric Analysis of Contact and Dynamic Stability and Its Application to Humanoid Push Recovery

Robert Schuller[1,3], George Mesesan[1,3], Johannes Englsberger[1], Christian Ott[1,2], Jinoh Lee[1,4], and Alin Albu-Schäffer[1,3]

Abstract

The three-dimensional divergent component of motion (3D-DCM) framework has been successfully utilized to generate center of mass (CoM) trajectories for various locomotion types. While the 3D-DCM encodes the CoM dynamics, it relies on the contact forces between the robot's end effectors and the environment to realize the intended motion. In the original formulation of the 3D-DCM, the feasibility of contact forces concerning contact constraints is assumed, but a comprehensive analysis of this assumption is lacking. In this work, we address this gap by extending the 3D-DCM framework to incorporate contact constraints and dynamic stability of the system. This is achieved by encoding feasible CoM forces as geometric sets. We derive an analytical relationship that characterizes how these sets can be modulated by humanoid push recovery strategies. Building on these insights, we propose a push recovery algorithm that integrates ankle, hip, height-variation, and stepping strategies. The proposed method is evaluated through extensive experiments with the humanoid robot TORO, including scenarios of force-disturbed balancing, walking, and multi-contact configurations.

Keywords

Humanoid locomotion, divergent component of motion (DCM), contact stability, dynamic stability, push recovery.

1. Introduction

1.1. Motivation

Locomotion and balance of legged robots are challenging problems due to the nonlinear dynamics of the system and the typically underactuated free-floating base of the robot. One approach that has been proven successful in the research community focuses on the center of mass (CoM) dynamics, which captures the most important aspects of the underlying system's dynamics. Many motion generation methods utilize *simplified models*, such as the linear inverted pendulum (LIP) (Kajita et al. 2001), or *template models*, such as the spring-loaded inverted pendulum (SLIP) (Geyer et al. 2006). Other methods are based on the instantaneous capture point (ICP) (Pratt et al. 2012), or the three-dimensional divergent component of motion (3D-DCM) (Englsberger et al. 2015). As it is directly derived from the CoM dynamics, the 3D-DCM represents an intrinsic property of the multi-body dynamics, rather than a simplified or template model.

One popular motion generation approach is based on the zero moment point (ZMP) (Vukobratović and Stepanenko 1972), which was developed to address the challenge of bipedal walking on horizontal ground. When assuming a constant angular momentum and a fixed CoM height, the relation between the CoM and ZMP simplifies to the LIP mode. These assumptions motivated the development of methods that do not necessitate zero torque about the CoM or CoM motions restricted to a horizontal plane. The 3D-DCM framework (Englsberger et al. 2015) addresses these shortcomings by proposing a method for motion planning and control. By introducing the enhanced centroidal moment pivot (eCMP), a point that encodes the direction and magnitude of external forces acting on the CoM, the linear CoM dynamics are decoupled on all three axes, enabling locomotion on arbitrary terrain.

Using the 3D-DCM framework, CoM trajectories for locomotion on non-planar and uneven terrain can be computed in closed form (Mesesan et al. 2018). The 3D-DCM framework has been successfully applied to multi-contact locomotion (Mesesan et al. 2017; Zambella et al. 2023), highly dynamic motions (Schuller et al. 2026), stair climbing (Mesesan et al. 2025), as well as running and jumping (Mesesan et al. 2023). To reduce complexity during motion planning, it is commonly assumed that the torque about the CoM is zero. However, this assumption is not

[1]Institute of Robotics and Mechatronics, German Aerospace Center (DLR), 82234 Wessling, Germany
[2]Automation and Control Institute, Faculty of Electrical Engineering and Information Technology, TU Wien, A-1040 Vienna, Austria
[3]School of Computation, Information and Technology, Technical University of Munich (TUM), 85748 Garching, Germany
[4]Department of Mechanical Engineering, KAIST, Daejeon 34141, South Korea

Corresponding author:
Robert Schuller, Institute of Robotics and Mechatronics, German Aerospace Center (DLR), Muenchener Str. 20, 82234 Wessling, Germany
Email: robert.schuller@dlr.de

a necessity; as demonstrated by Schuller et al. (2022), a torque about the CoM can be incorporated into 3D-DCM-based motion planning to enhance walking robustness. Additionally, it is assumed that the translational friction in the contacts is sufficient to generate the forces required to follow the generated trajectories. Under these assumptions, the motion planning problem is reduced to finding eCMP trajectories that are located within the contact area (the convex hull of all ground contacts (Vukobratović and Stepanenko 1972)) of the robot.

Furthermore, Englsberger et al. (2015) introduced a DCM tracking controller to stabilize the diverging DCM dynamics without influencing the converging CoM dynamics. The controller outputs a commanded eCMP position, which leads to an asymptotically converging DCM error. In this work, we refer to *dynamic stability* if the condition of a converging DCM error is fulfilled. This property is especially important when the system is perturbed by external disturbances. However, the DCM controller does not consider whether the commanded eCMP can be realized by the end effectors, especially w.r.t. the contact constraints. One essential requirement for stable legged balancing and locomotion is that the end effectors in contact do not move relative to the environment, generally referred to as *contact stability*. A contact-stable eCMP position would ensure that the following contact constraints are fulfilled:

- Center of pressure (CoP) constraint
- Translational Coulomb friction constraint
- Rotational Coulomb friction constraint

A violation of contact stability could cause the contact to tilt when the CoP constraint is violated, slide when the translational force is too high, or twist if the rotational Coulomb friction is not sufficient. Since the eCMP encodes the external forces acting on the CoM, resulting from the contact wrenches of the individual end effectors, it naturally connects to the contact constraints.

Despite these successes of the 3D-DCM in motion planning and control in legged locomotion, it is still an open research question on how to compute feasible eCMP positions that ensure both *contact stability* and *dynamic stability* without introducing simplifying assumptions. Solving this problem enables more dynamic, more robust, and less conservative motions by incorporating the actual contact and dynamic constraints into the planning and control processes.

1.2. Related Work

The literature on contact and dynamic stability in legged systems, as well as the research field focused on how humanoid robots respond to disturbances, commonly referred to as *push recovery*, is extensive. Although not exhaustive, we provide an overview of the most relevant literature related to our research question.

1.2.1. Contact Stability. The literature on *feasible regions* addresses the question of which motions, particularly CoM motions, can be executed without violating contact constraints. Some studies also consider kinematic joint or torque limits (Orsolino et al. 2020).

An established approach to ensure contact stability is to verify that the ZMP lies within the support area. The ZMP is a point that encodes the CoM position and acceleration and has been widely used in bipedal locomotion as a stability criterion (Kajita et al. 2003). However, the ZMP criterion has some limitations: it only applies when all contacts are coplanar and does not account for the translational and rotational friction limits in the contacts.

Drawing inspiration from computational geometry, researchers introduced the gravito-inertial wrench encoding full contact stability (Takao et al. 2003; Hirukawa et al. 2006; Caron et al. 2015a). This method maps friction limits, defined at the contacts, to the 6D space of the centroidal wrench and verifies whether the sum of the gravitational and inertial wrenches applied at the CoM falls within the polyhedral convex cone of the contact wrenches. The contact wrench cone (CWC) (Caron et al. 2015b) represents the projection of all contact forces within their respective friction cones and indicates the feasible wrenches for which the contact constraints are satisfied. Dai and Tedrake (2016) use the CWC as a generalized ZMP criterion to assess the robot's dynamic stability. The limitation of these approaches is that the geometrically intuitive criterion of the ZMP being an element of the support area is replaced by an abstract and less intuitive 6D wrench cone.

To tackle this problem, Caron et al. (2017) define the so-called *full ZMP support area*, which must lie within a 2D projection of the convex polyhedral wrench cone. The authors extend the definition of the ZMP in the sense that all points on a line connecting the CoP and the CoM are ZMPs. The relation between the CoP and the original ZMP is discussed by Sardain and Bessonnet (2004). The ZMP, as an element of the full ZMP support area, is used to verify multi-contact stability. Furthermore, Caron and Kheddar (2017) consider a floating-base inverted pendulum model and characterize the contact stability conditions for the friction and CoP constraints by analytically deriving the corresponding sets under the assumption of constant angular momentum.

The aforementioned approaches (Caron et al. 2017; Caron and Kheddar 2017) use the instantaneous CoM position as input and determine the feasible region of CoM accelerations. In contrast, the methods presented below take potential CoM accelerations as input and compute feasible regions for CoM positions.

Audren and Kheddar (2018) introduce the so-called robust stability region under contact constraints for multi-contact scenarios, which is a 3D set of feasible CoM positions, assuming a set of previously provided CoM accelerations from disturbances or control inputs. Abdalla et al. (2023) introduce a 2D reachable region w.r.t. contact constraints, joint kinematic, and torque limits for CoM positions projected on an arbitrary plane considering the actual CoM acceleration of the current state. The authors use an iterative projection algorithm to compute a convex hull approximation of the feasible region.

1.2.2. Dynamic Stability. In addition to contact stability, *dynamic stability* must be ensured for stable legged locomotion. The research area of *capture regions* examines legged stability from the perspective of where to step next to maintain balance during locomotion (Pratt et al. 2006; Koolen et al. 2012). One direction of research is the *capturability analysis* of the state of legged systems. The N-step capturability is based on the 3D LIP model with flywheel (Pratt et al. 2006) and is the system's ability to come to a stop without falling while taking a maximum of N steps (Koolen et al. 2012). Zero-step capturability refers to the problem of coming to a stop without changing the current contact configuration of the robot (Del Prete et al. 2018).

A further research direction leverages the concept of *hybrid zero dynamics* (HZD) to design controllers for periodic walking motions in bipedal robots, with provable stability of the system (Grizzle et al. 2001). An HZD-based controller is used by Sreenath et al. (2011) to develop an asymptotically stable walking gait, utilizing the compliance of the robot's drivetrain to enhance energy efficiency.

1.2.3. Push Recovery. Biomechanical studies of human motion (Horak and Nashner 1986; Maki and McIlroy 1997; Runge et al. 1999; Pijnappels et al. 2010; Cheng et al. 2018) have identified several reaction strategies in response to pushes or other disturbances: the ankle, hip, height-variation, and step strategies.

Well-established in the push recovery literature are the *ankle strategy*, which features a shifting of the CoP within the contact area while maintaining a fixed upper-body posture, and the *hip strategy*, which induces angular momentum, typically by moving the upper body (Horak and Nashner 1986; Runge et al. 1999; Pijnappels et al. 2010). Moreover, the *height-variation strategy* moves the CoM upward to increase the normal contact forces (Cheng et al. 2018). A further reaction strategy is extending the area of support by changing the contact configuration, for example by taking a step or grasping a fixed object; in legged locomotion, this is commonly referred to as *step strategy*. In contrast to the traditional view, studies indicate that the step strategy is not necessarily the reaction strategy of last resort but is initiated early in the push recovery process of humans (Maki and McIlroy 1997).

The research field of humanoid push recovery draws inspiration from human motion studies. For *balancing* applications, numerous approaches employ combinations of the aforementioned strategies (Atkeson and Stephens 2007; Hinata and Nenchev 2018). Most push recovery algorithms for balancing integrate a combination of ankle and hip strategies (Hyon et al. 2009). Typically, the ankle strategy is employed until saturation, and if required for balance, the hip strategy is activated as well (Schuller et al. 2021). Hofmann et al. (2009) introduce a CoM controller that prioritizes linear momentum tasks over angular momentum regulation when faced with significant external disturbances. Lee and Goswami (2012) presented a momentum-based balance controller that accounts for contact constraints while generating feasible momenta. van Hofslot et al. (2019) and Liu et al. (2021) demonstrate that the height-variation strategy can also be an effective method for balance recovery.

For *walking* scenarios, the literature naturally emphasizes a combination of ankle and step strategy, often integrated with step time adjustment. Many approaches leverage simplified or template models to decrease complexity. Aftab et al. (2012) employed a nonlinear model predictive control (MPC) scheme to integrate ankle, hip, and step strategies with step time adjustment, utilizing a LIP model with a flywheel, while Shafiee et al. (2019) present a DCM-based step time and position adjustment for single support phases, using an exponential interpolation of the ZMP trajectory. Kim et al. (2023) presented an MPC for the DCM dynamics to optimize the next footstep position in single and double support phases.

Khadiv et al. (2020) proposed a walking controller that adapts the next step's position and timing. This approach does not require explicit control of the CoP or CoM position. Jeong et al. (2019) exploit the analytical solution of the DCM dynamics in combination with a LIP plus flywheel model for their walking controller. This controller includes ankle, hip, and step strategies, along with step time adjustment. Recently, Choe et al. (2023) extended this work using a nonlinear MPC approach, enabling the simultaneous activation of all strategies.

The work of Griffin et al. (2023) introduces a walking controller that incorporates an ankle, hip, and step strategy with time adjustment, placing particular emphasis on cross-over step recovery. Mesesan et al. (2021) present an analytical algorithm for step position adjustment applicable to both single and double support phases, utilizing the closed-form solution of the DCM dynamics. Recently, Egle et al. (2023) extended this approach by formulating a QP problem with variable phase timing. To reduce complexity, the methods mentioned above commonly use the robot's foot area in single support or a combinatorial variant of both foot areas in double support as the contact area for the ankle strategy, while neglecting Coulomb friction constraints. However, these assumptions for contact stability are incomplete, as we will discuss in this work.

1.3. Contributions of the Article

In this work, we extend the 3D-DCM framework by incorporating contact constraints and dynamic stability of the system. Through a geometric analysis of these constraints, we derive a mathematical formulation that defines individual contact constraints and dynamic stability in terms of sets of feasible eCMP positions. Additionally, we analyze how these sets are modulated by variations in angular momentum or CoM height. Building on these insights, we develop a push recovery strategy for humanoid robots to maintain balance in the presence of external disturbances. The algorithm stabilizes the DCM using a DCM tracking controller while also ensuring that the commanded eCMP provides both contact and dynamic stability. We propose a novel combination of ankle, hip, height-variation, and step strategies for both balancing scenarios, including multi-contact configurations and walking scenarios in single and double support phases.

The presented geometric framework not only facilitates the design of push recovery algorithms but also provides a tool for post-hoc analysis of motions, i.e., the examination and evaluation of motions after they have been executed. This capability is particularly beneficial in the domain of black-box algorithms, as it introduces an element of explainability to popular reinforcement learning methods. In particular, it addresses the question: "Why did the robot react the way it did to the disturbance?"

The main contributions of this work are:

- we derive a geometric interpretation of contact and dynamic stability based on the 3D-DCM framework and analyze how the corresponding eCMP sets can be modulated in the context of humanoid push recovery by variations in angular momentum or CoM height;
- we propose a push recovery algorithm with a combination of ankle, hip, height-variation, and step strategies. The proposed approach is evaluated in various experiments with the humanoid robot TORO (Englsberger et al. 2014), including force-disturbed balancing, walking, and multi-contact scenarios.

The rest of the work is structured as follows: Section 2 covers the fundamentals of contact constraints and the main concepts of the 3D-DCM framework. Section 3 introduces a geometric analysis of contact and dynamic stability, followed by an analysis of how these sets can be modulated in the context of humanoid push recovery in Section 4. Section 5 presents an algorithm for scheduling reaction strategies based on the insights of the geometric analysis of contact and dynamic stability. Extensive experiments demonstrating the capabilities of the proposed push recovery method are provided in Section 6. The advantages and limitations of the proposed method are discussed in Section 7. Finally, Section 8 concludes the work.

2. Fundamentals and Preliminaries

In this section, we present the centroidal dynamics of a free-floating base system and a contact constraint formulation to ensure contact stability. Additionally, we provide the main results from our previous work on the 3D-DCM framework (Englsberger et al. 2015; Mesesan et al. 2018; Schuller et al. 2022).

2.1. Centroidal Dynamics

The momentum balance principle states that the rate of change of the centroidal translational $\boldsymbol{p}_c \in \mathbb{R}^3$ and angular momentum $\boldsymbol{l}_c \in \mathbb{R}^3$ is equal to the sum of all CoM-mapped contact forces $\boldsymbol{f}_i \in \mathbb{R}^3$ and contact torques $\boldsymbol{\tau}_i \in \mathbb{R}^3$ of the $p \in \mathbb{N}$ contacts

$$\begin{pmatrix} \dot{\boldsymbol{p}}_c \\ \dot{\boldsymbol{l}}_c \end{pmatrix} = \begin{pmatrix} m\boldsymbol{g} \\ \boldsymbol{0} \end{pmatrix} + \sum_{i=1}^{p} \begin{pmatrix} \boldsymbol{f}_i \\ \boldsymbol{f}_i \times \boldsymbol{x}_{ic} + \boldsymbol{\tau}_i \end{pmatrix}, \tag{1}$$

where $\boldsymbol{x}_{ic} = \boldsymbol{x} - \boldsymbol{x}_i$ is the vector from the i-th contact position $\boldsymbol{x}_i \in \mathbb{R}^3$ to the CoM position $\boldsymbol{x} \in \mathbb{R}^3$. The total mass of the robot is m, and $\boldsymbol{g} = (0, 0, -g)^T$ is the vector of gravitational acceleration with g being the gravitational constant. The momentum variables are expressed in a frame located at the CoM position and aligned with the world frame. The contact wrench of the i-th contact is $\boldsymbol{w}_i = (\boldsymbol{f}_i^T, \boldsymbol{\tau}_i^T)^T$ and acts at the respective end effector frame, which has the position $\boldsymbol{x}_i$ and is aligned with the world frame.

2.2. Contact Model

In the context of legged locomotion, the contact points are usually defined at the end effectors of the system. Since the nature of legged locomotion involves establishing and breaking contacts, the end effectors are not fixed to the environment. To prevent unintentional motion between the end effector and the contact surface, contact constraints are formulated to limit the forces and torques transferred during contact.

We assume that all contacts between the robot and the environment are flat, with the contact surface of the i-th contact being denoted by $\mathcal{S}_i \subset \mathbb{R}^3$. The corresponding contact normal $\boldsymbol{n}_i \in \mathbb{R}^3$ is perpendicular to $\mathcal{S}_i$, pointing away from the environment. For end effectors that can only push against the contact surface and not pull, a constraint representing the unilaterality of the contact is formulated as follows:

$$\boldsymbol{n}_i \cdot \boldsymbol{f}_i \geq f_{\perp,i}^{min}, \tag{2}$$

where $f_{\perp,i}^{min} \geq 0$ realizes a minimum perpendicular force exerted on the environment.

To prevent translational slippage of the end effector, Coulomb's model for translational static friction is implemented via

$$||\boldsymbol{n}_i \times (\boldsymbol{f}_i \times \boldsymbol{n}_i)||_2 \leq \mu_i(\boldsymbol{n}_i \cdot \boldsymbol{f}_i) \tag{3}$$

with $\mu_i \geq 0$ being the friction coefficient of the i-th contact.

Furthermore, to prevent the end effector from tilting, the CoP $\boldsymbol{p}_i \in \mathbb{R}^3$ (Popovic et al. 2005) must remain strictly within the contact area $\mathcal{S}_i$

$$\boldsymbol{p}_i = \frac{\boldsymbol{n}_i \times \boldsymbol{\tau}_i}{\boldsymbol{n}_i \cdot \boldsymbol{f}_i} + \boldsymbol{x}_i \in \mathcal{S}_i. \tag{4}$$

If the torque in the direction of the contact normal is not constrained, rotational slippage around the contact normal may occur. To avoid this scenario, corresponding constraints are added

$$\tau_{\perp,i}^{min} \leq \boldsymbol{n}_i \cdot \boldsymbol{\tau}_i \leq \tau_{\perp,i}^{max}, \tag{5}$$

where $\tau_{\perp,i}^{min}$ and $\tau_{\perp,i}^{max}$ are the lower and upper limits for the perpendicular contact torque, respectively. As pointed out by Caron et al. (2015b) and Henze (2020), $\tau_{\perp,i}^{min}$ and $\tau_{\perp,i}^{max}$ are not constant values but are functions of the other elements of the contact wrench.

Assuming rectangular contact areas, Caron et al. (2015b) present a constraint formulation for the upper and lower limits of the perpendicular contact torque in (5). A rectangular contact area with the length of $2\,p_x^{max}$ and width of $2\,p_y^{max}$ is considered, where p_x^{max} and p_y^{max} represent the maximum allowable CoP deviation in x- and y-direction, respectively. Starting from a base vector parametrization at the four corner points and corresponding linearized friction cones, eight inequality constraints can be derived leading to upper and lower limits for the perpendicular contact torque. The derivation can be found in Appendix B.

The proposed limits can be expressed as eight half-space constraints:

$$0 \geq \boldsymbol{f}_i \cdot \boldsymbol{\kappa}_1 + \boldsymbol{\tau}_i \cdot \boldsymbol{\kappa}_2 \tag{6}$$

$$0 \geq \boldsymbol{f}_i \cdot \boldsymbol{\kappa}_1 - \boldsymbol{\tau}_i \cdot \boldsymbol{\kappa}_2 \tag{7}$$

with

$$\boldsymbol{\kappa}_1 = \boldsymbol{R}_i \begin{pmatrix} \sigma_1 p_y^{max} \\ \sigma_2 p_x^{max} \\ -\tilde{\mu}(p_x^{max} + p_y^{max}) \end{pmatrix} \tag{8}$$

and

$$\boldsymbol{\kappa}_2 = \boldsymbol{R}_i \begin{pmatrix} \sigma_1 \tilde{\mu} \\ \sigma_2 \tilde{\mu} \\ 1 \end{pmatrix}, \tag{9}$$

where $\sigma_1 \in \{-1, 1\}$ and $\sigma_2 \in \{-1, 1\}$ result from the four contact point locations. Here, $\tilde{\mu} = \frac{1}{\sqrt{2}}\mu$ is the friction parameter of the pyramidal inner approximation of the friction cone (Henze et al. 2016). We define for each contact an orthonormal frame composed of the normal $\boldsymbol{n}_i$ and two tangent vectors $\boldsymbol{t}_{xi} \in \mathbb{R}^3$ and $\boldsymbol{t}_{yi} \in \mathbb{R}^3$, which are aligned with the edges of the rectangle contact area. Consequently, the rotation matrix $\boldsymbol{R}_i = (\boldsymbol{t}_{xi},\ \boldsymbol{t}_{yi},\ \boldsymbol{n}_i)$ transforms coordinates from contact to world frame.

Note that the eight inequality constraints on the contact wrench in (6) and (7) express the same condition as the perpendicular contact torque formulation in (5). The constraints in (6) correspond to $\tau_{\perp,i}^{max}$, while (7) results in $\tau_{\perp,i}^{min}$.

There are various approaches to formulating contact constraints. One popular approach is the base vectors parametrization, which describes the wrenches applied to the environment by defining contact forces at the vertices of the contact area (Caron et al. 2017). This method divides a single surface contact into several point contacts and applies only the translational Coulomb friction constraint (3) to each contact force. A drawback of this method is that it requires a larger set of coordinates and only indirectly incorporates CoP and rotational friction constraints. As a result, it lacks interpretability in addressing the three types of contact stability violations: tilting, sliding, and twisting. Therefore, we choose the six-dimensional contact wrench parametrization because it features a minimal set of coordinates to describe the forces and torques transferred in a contact (Henze 2020).

2.3. 3D-DCM Framework

The core idea of the 3D-DCM is to reformulate the CoM dynamics by representing the CoM velocity $\dot{\boldsymbol{x}} \in \mathbb{R}^3$ and acceleration $\ddot{\boldsymbol{x}} \in \mathbb{R}^3$ vectors as 3D points. These points can then be utilized for generating reference trajectories or for the geometrical interpretation of contact and dynamic stability.

2.3.1. Fundamentals of 3D-DCM. According to Newton's second law, the motion of the CoM follows the second-order dynamics:

$$\ddot{\boldsymbol{x}} = \frac{1}{m}\boldsymbol{f} + \boldsymbol{g}, \tag{10}$$

which results from rewriting the translational elements of the centroidal dynamics in (1). The sum of all external forces acting at the CoM is summarized in

$$\boldsymbol{f} = \sum_{i=1}^{p} \boldsymbol{f}_i. \tag{11}$$

To transform the second-order CoM dynamics (10) into two first-order systems, Englsberger et al. (2015) introduced the 3D-DCM $\boldsymbol{\xi} \in \mathbb{R}^3$. The DCM is defined as the linear combination of the CoM position and velocity, see Figure 1,

$$\boldsymbol{\xi} = \boldsymbol{x} + b\dot{\boldsymbol{x}}. \tag{12}$$

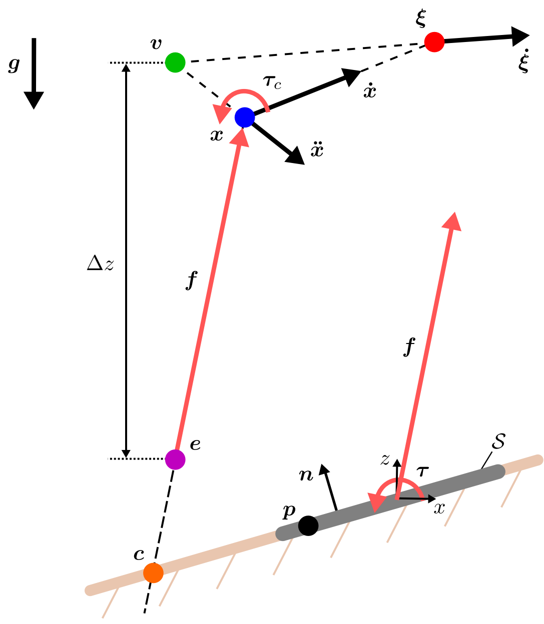

Figure 1. Relations of the points defined in the 3D-DCM framework: CoM ($\boldsymbol{x}$), DCM ($\boldsymbol{\xi}$), VRP ($\boldsymbol{v}$), and eCMP ($\boldsymbol{e}$). Additionally, the CMP ($\boldsymbol{c}$) and the CoP ($\boldsymbol{p}$) are depicted. The contact torque ($\boldsymbol{\tau}$) and force ($\boldsymbol{f}$), as well as the torque about the CoM ($\boldsymbol{\tau}_c$) are illustrated. The contact area ($\mathcal{S}$) and normal ($\boldsymbol{n}$) specify the contact between the robot and the environment. The vector of gravitational acceleration is represented by $\boldsymbol{g}$.

Here, $b = \sqrt{\frac{\Delta z}{g}}$ is the DCM time constant, and $\Delta z > 0$ is a free motion parameter, typically chosen as the average CoM height above the ground for walking scenarios. The unstable first-order dynamics of the DCM are reformulated as

$$\dot{\boldsymbol{\xi}} = \frac{1}{b}(\boldsymbol{\xi} - \boldsymbol{v}) \tag{13}$$

with $\boldsymbol{v} \in \mathbb{R}^3$ being the virtual repellent point (VRP), encoding the direction and magnitude of the CoM acceleration

$$\boldsymbol{v} = \boldsymbol{x} - b^2\ddot{\boldsymbol{x}}. \tag{14}$$

By reordering (12), we obtain the stable CoM dynamics w.r.t. the DCM

$$\dot{\boldsymbol{x}} = -\frac{1}{b}(\boldsymbol{x} - \boldsymbol{\xi}). \tag{15}$$

Note that the CoM follows the DCM while the DCM diverges from the VRP. To encode the direction and magnitude of the external forces acting on the CoM, the eCMP $\boldsymbol{e} \in \mathbb{R}^3$ is introduced by Englsberger et al. (2015) as

$$\boldsymbol{f} = \frac{m}{b^2}(\boldsymbol{x} - \boldsymbol{e}). \tag{16}$$

Unlike previous works, we consider the eCMP rather than the VRP as the control input of the 3D-DCM framework, since it directly relates to the external forces the robot generates in interaction with the environment. Note that, unlike the VRP, the eCMP does not include the gravitational force acting on the CoM

$$\boldsymbol{e} = \boldsymbol{x} - b^2(\ddot{\boldsymbol{x}} - \boldsymbol{g}) = \boldsymbol{x} - \frac{b^2}{m}\boldsymbol{f}. \tag{17}$$

Combining (10), (14), and (16), we obtain the following relation:

$$\boldsymbol{v} = \boldsymbol{e} + (0,\ 0,\ \Delta z)^T, \tag{18}$$

indicating that the VRP is only separated from the eCMP by a vertical offset Δz. Unlike the centroidal momentum pivot (CMP) (Popovic et al. 2005) $\boldsymbol{c} \in \mathbb{R}^3$, the eCMP is not constrained to be within the plane of the contact surface.

2.3.2. 3D-DCM Reference Trajectory Generation. Below, we briefly review our prior work on DCM reference trajectory generation for locomotion (Englsberger et al. 2015; Mesesan et al. 2018; Mesesan et al. 2023). First, we define a sequence of k eCMP waypoints $\{\boldsymbol{e}_1, \ldots, \boldsymbol{e}_k\}$ based on the desired footsteps. An eCMP trajectory is obtained by temporally interpolating between the corresponding waypoints. Afterward, we compute the corresponding DCM trajectory backward in time, starting at the end of the motion. Note that the DCM dynamics (13) become stable with reverse time flow (Englsberger et al. 2015). To obtain the final CoM reference trajectory, we solve the linear differential equation of the CoM dynamics (15), based on the computed DCM trajectory, forward in time.

The resulting DCM reference trajectory $\boldsymbol{\xi}^d$ can be analytically computed as a function of the eCMP waypoints and the final DCM position $\boldsymbol{\xi}_k$, as given by the following closed-form expression:

$$\boldsymbol{\xi}^{d,T}(t) = \boldsymbol{C}_\xi(t)\big[\boldsymbol{e}_1,\ \boldsymbol{e}_2,\ \boldsymbol{e}_3,\ \ldots,\ \boldsymbol{e}_k,\ \boldsymbol{\xi}_k\big]^T + (0, 0, \Delta z). \tag{19}$$

The coefficient matrix $\boldsymbol{C}_\xi(t) \in \mathbb{R}^{1\times(k+1)}$ is computed based on the transition timings of the eCMP waypoint interpolations and the DCM time constant b. For computational details, please refer to Mesesan et al. (2018) and Schuller et al. (2022). In our previous works, VRP waypoints were used instead of eCMP waypoints to compute the DCM reference. In the notation that follows, the time dependence of quantities is omitted for simplicity.

Note that the average CoM height above the ground Δz, and consequently the DCM time constant b, can vary across different locomotion scenarios. To ensure that the eCMP remains on the ground with the contact forces focused at the contact point, and to preserve a closed-form solution for the DCM and CoM trajectories, a piecewise-constant interpolation of Δz and b can be employed. For more details, please refer to Mesesan et al. (2023).

2.3.3. 3D-DCM Tracking Controller. To follow the generated reference trajectory, we use the DCM control law presented by Englsberger et al. (2015). Since the first-order CoM dynamics (15) is stable, it is sufficient to formulate a control law for stabilizing the DCM dynamics (13), which is inherently unstable. To track the desired DCM trajectory $\boldsymbol{\xi}^d$, the following desired closed-loop dynamics is introduced:

$$\Delta\dot{\boldsymbol{\xi}} = -\boldsymbol{K}_\xi \Delta\boldsymbol{\xi} \tag{20}$$

with the DCM control gain matrix $\boldsymbol{K}_\xi \in \mathbb{R}^{3\times3}$ being diagonal and positive definite. The deviation of the DCM from its reference trajectory is denoted by $\Delta\boldsymbol{\xi} = \boldsymbol{\xi} - \boldsymbol{\xi}^d$.

We obtain the final control law for the commanded VRP by substituting (13) for desired and actual states into (20)

$$\boldsymbol{v}^{cmd} = \boldsymbol{v}^d + (\boldsymbol{I}_{3\times3} + b\boldsymbol{K}_\xi)\Delta\boldsymbol{\xi}. \tag{21}$$

Based on (18), the equation can be equivalently expressed for the commanded and desired eCMP as

$$\boldsymbol{e}^{cmd} = \boldsymbol{e}^d + (\boldsymbol{I}_{3\times3} + b\boldsymbol{K}_\xi)\Delta\boldsymbol{\xi}. \tag{22}$$

Note that in the absence of disturbances, a reverse time-generated DCM reference trajectory can be followed by a pure feedforward controller ($\boldsymbol{e}^{cmd} = \boldsymbol{e}^d$). To account for perturbations, the feedback component of the controller is required to stabilize the DCM dynamics.

By combining (16) and (22), the desired external force acting on the CoM is obtained, which is typically realized by a whole-body controller.

3. Geometric Analysis of eCMP Sets under Contact and Dynamic Stability Constraints

We relate the 3D-DCM quantities to the contact model described in Section 2.2 by deriving 3D sets of feasible eCMP positions, i.e., positions encoding force vectors acting at the CoM, which result from the respective constraints. The analytically derived geometric interpretation offers insight into how the constraints shape the feasible sets and provides interpretability for a problem that is typically addressed by a numerical solver, which usually outputs a result without further intuition. Geometric insights can enhance trajectory design and allow for active modulation of the feasible sets by providing a deeper understanding of contact and dynamic stability.

In addition to the three feasible eCMP sets that we will derive from the contact constraints (CoP, translational, and rotational friction), we introduce a fourth set that relates to the DCM error dynamics. If all four sets intersect, an eCMP solution exists that leads to a converging DCM error while maintaining contact stability. We refer to this intersection set as the *recovering eCMP set*.

The 3D sets of feasible eCMP positions will be defined as a function of the CoM position, contact area, and torque about the CoM. These sets indicate which external CoM forces (encoded as eCMP positions) can be realized for the given state and contact constraints.

We simplify notation by assuming that there is only one contact between the robot and the environment to avoid the force distribution problem across multiple end effectors. Consequently, the index i indicating the specific contact is omitted. We also assume that the world and contact frames coincide, i.e., $\boldsymbol{x}_i = \boldsymbol{0}$ and $\boldsymbol{x}_{ic} = \boldsymbol{x}$. The following derived relations also hold for an arbitrarily located world frame; however, in that case, the vector $\boldsymbol{x}_i$ would also appear.

3.1. CoP Constraint

In order to connect the 3D-DCM framework with the CoP constraint ($\boldsymbol{p} \in \mathcal{S}$), which prevents the contact from tilting, we derive a general relationship among the CoP, eCMP, and the contact wrench. Recalling the relation for the CoP in (4) and substituting the definition of the contact torque from (1),

$$\boldsymbol{\tau} = \boldsymbol{x} \times \boldsymbol{f} + \boldsymbol{\tau}_c \tag{23}$$

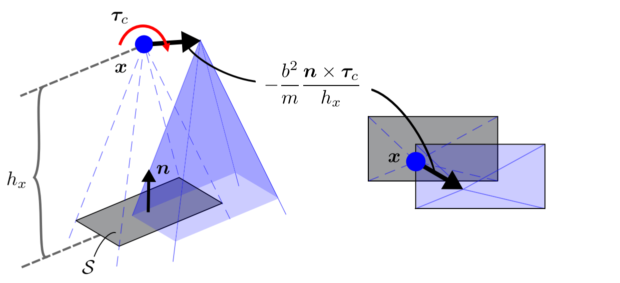

Figure 2. Set of feasible eCMP positions based on the CoP constraint ($\boldsymbol{p} \in \mathcal{S}$) shown in a 3D view (left) and a top-down view (right). The cone is shifted parallel to the contact surface as a result of a torque about the CoM. The dashed lines indicate the cone given a constant angular momentum ($\boldsymbol{\tau}_c = \boldsymbol{0}$). The gray area illustrates the rectangular contact area of the robot.

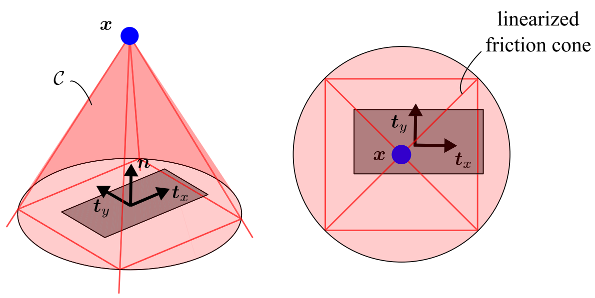

Figure 3. Set of feasible eCMP positions resulting from the translational friction constraint shown in a 3D view (left) and a top-down view (right). The actual friction cone and its inner pyramidal approximation are indicated.

with $\dot{\boldsymbol{l}}_c = \boldsymbol{\tau}_c$ being the torque about the CoM, we obtain

$$\begin{aligned}\boldsymbol{p} &= \frac{(\boldsymbol{n}\cdot\boldsymbol{f})\boldsymbol{x} - (\boldsymbol{n}\cdot\boldsymbol{x})\boldsymbol{f} + \boldsymbol{n}\times\boldsymbol{\tau}_c}{\boldsymbol{n}\cdot\boldsymbol{f}} \\ &= \boldsymbol{x} - \frac{\boldsymbol{n}\cdot\boldsymbol{x}}{\boldsymbol{n}\cdot\boldsymbol{f}}\boldsymbol{f} + \frac{\boldsymbol{n}\times\boldsymbol{\tau}_c}{\boldsymbol{n}\cdot\boldsymbol{f}},\end{aligned} \tag{24}$$

which expresses the CoP as a function of the CoM position $\boldsymbol{x}$, external force $\boldsymbol{f}$, and torque about the CoM $\boldsymbol{\tau}_c$ (Caron et al. 2017). By combining (16) and (24), we obtain a relationship between the CoP and eCMP by substituting the external force vector

$$\boldsymbol{p} = \boldsymbol{x} - \frac{\boldsymbol{n}\cdot\boldsymbol{x}}{\boldsymbol{n}\cdot(\boldsymbol{x}-\boldsymbol{e})}(\boldsymbol{x}-\boldsymbol{e}) + \frac{b^2(\boldsymbol{n}\times\boldsymbol{\tau}_c)}{m(\boldsymbol{n}\cdot(\boldsymbol{x}-\boldsymbol{e}))}. \tag{25}$$

To express the CoP constraint as eCMP set membership, we reorder (25):

$$\boldsymbol{e} = \left(1 - \frac{\boldsymbol{n}\cdot\boldsymbol{e}}{\boldsymbol{n}\cdot\boldsymbol{x}}\right)\boldsymbol{p} + \frac{\boldsymbol{n}\cdot\boldsymbol{e}}{\boldsymbol{n}\cdot\boldsymbol{x}}\boldsymbol{x} - \frac{b^2(\boldsymbol{n}\times\boldsymbol{\tau}_c)}{m(\boldsymbol{n}\cdot\boldsymbol{x})}. \tag{26}$$

Following the idea of Caron et al. (2017), we introduce $h_e = \boldsymbol{n}\cdot\boldsymbol{e}$ and $h_x = \boldsymbol{n}\cdot\boldsymbol{x}$ as the perpendicular height of the eCMP and CoM above the contact surface, respectively. To ensure contact unilaterally, the following relation must hold

$$h_e \leq h_x, \tag{27}$$

i.e., the eCMP must be located below the CoM w.r.t. the contact surface to ensure that the end effector is pushing against the environment. Then, we substitute the perpendicular heights of the eCMP and CoM into (26)

$$\boldsymbol{e} = \left(1 - \frac{h_e}{h_x}\right)\boldsymbol{p} + \frac{h_e}{h_x}\boldsymbol{x} - \frac{b^2}{m}\frac{\boldsymbol{n}\times\boldsymbol{\tau}_c}{h_x}. \tag{28}$$

From the unilateral constraint (27), we derive that $\frac{h_e}{h_x} \leq 1$. Assuming $\boldsymbol{\tau}_c = \boldsymbol{0}$, the eCMP is located on a ray with its origin at the CoM position and intersecting the CoP position, see Figure 2,

$$\boldsymbol{e} \in \left\{\boldsymbol{x} + \alpha(\boldsymbol{p}-\boldsymbol{x}) \;\middle|\; \boldsymbol{p}\in\mathcal{S}, \alpha \geq 0\right\}. \tag{29}$$

Depending on the torque about the CoM, the origin of the ray is shifted by a factor of $-\frac{b^2}{m}\frac{\boldsymbol{n}\times\boldsymbol{\tau}_c}{h_x}$, while its direction vector $(\boldsymbol{p}-\boldsymbol{x})$ remains unchanged. The direction of the shift is parallel to the contact surface because the term $\boldsymbol{n}\times\boldsymbol{\tau}_c$ projects the torque about the CoM onto a plane perpendicular to $\boldsymbol{n}$, the contact surface normal. Since $\boldsymbol{p}$ is an element of $\mathcal{S}$, the rays are aggregated in a conical hull[1]

$$\boldsymbol{e} \in \left\{\boldsymbol{x} - \frac{b^2}{m}\frac{\boldsymbol{n}\times\boldsymbol{\tau}_c}{h_x} + \boldsymbol{e}' \;\middle|\; \boldsymbol{e}' \in \operatorname{cone}(\mathcal{S}-\boldsymbol{x})\right\}. \tag{30}$$

In conclusion, to fulfill the CoP constraint, the eCMP needs to belong to a cone[2] spanned from the CoM to the vertices of the contact area. The cone is shifted parallel to the contact surface based on the torque about the CoM.

3.2. Coulomb Friction Constraint (translational)

By inserting the eCMP definition (16) into the translational friction constraint (3), which prevents the contact from sliding, we obtain the following relationship:

$$||\boldsymbol{n}\times((\boldsymbol{x}-\boldsymbol{e})\times\boldsymbol{n})||_2 \leq \mu(\boldsymbol{n}\cdot(\boldsymbol{x}-\boldsymbol{e})). \tag{31}$$

Accordingly, the norm of the parallel component of the eCMP-CoM vector w.r.t. the contact surface needs to be less than or equal to the perpendicular component of the eCMP-CoM vector multiplied by the friction coefficient. The geometrical interpretation is that the eCMP must lie within a cone $\mathcal{C} \subset \mathbb{R}^3$ whose apex is at the CoM position, with its face directed toward the contact surface and its axis aligned with the contact normal vector $\boldsymbol{n}$ (Caron and Kheddar 2017)

$$\boldsymbol{e} \in \{\boldsymbol{x} + \boldsymbol{e}' \mid \boldsymbol{e}' \in \mathcal{C}\} \tag{32}$$

with

$$\mathcal{C} = \left\{\boldsymbol{e}' \in \mathbb{R}^3 \mid ||\boldsymbol{n}\times(\boldsymbol{e}'\times\boldsymbol{n})||_2 \leq -\mu(\boldsymbol{n}\cdot\boldsymbol{e}')\right\}. \tag{33}$$

Coulomb friction is typically linearized by an inner approximation through a square-based pyramid, see Figure 3. The linearized translational friction constraint can be formulated for the eCMP in the direction of the two tangent vectors $\boldsymbol{t}_x$ and $\boldsymbol{t}_y$ independently of each other

$$\begin{aligned}-\tilde{\mu}(\boldsymbol{n}\cdot(\boldsymbol{x}-\boldsymbol{e})) + \boldsymbol{t}_x\cdot\boldsymbol{x} \leq \boldsymbol{t}_x\cdot\boldsymbol{e} \leq \tilde{\mu}(\boldsymbol{n}\cdot(\boldsymbol{x}-\boldsymbol{e})) + \boldsymbol{t}_x\cdot\boldsymbol{x}, \\ -\tilde{\mu}(\boldsymbol{n}\cdot(\boldsymbol{x}-\boldsymbol{e})) + \boldsymbol{t}_y\cdot\boldsymbol{x} \leq \boldsymbol{t}_y\cdot\boldsymbol{e} \leq \tilde{\mu}(\boldsymbol{n}\cdot(\boldsymbol{x}-\boldsymbol{e})) + \boldsymbol{t}_y\cdot\boldsymbol{x}.\end{aligned} \tag{34}$$

Consequently, the eCMP must lie within a cone whose apex is at the CoM position and spans to the vertices of the base of the reverse pyramid

$$\boldsymbol{e} \in \left\{\boldsymbol{x} + \boldsymbol{e}' \mid \boldsymbol{e}' \in \operatorname{cone}\left(\{-\boldsymbol{n} \pm \tilde{\mu}\boldsymbol{t}_x \pm \tilde{\mu}\boldsymbol{t}_y\}\right)\right\}. \tag{35}$$

3.3. Coulomb Friction Constraint (rotational)

The set of eCMP positions that satisfy the rotational friction constraint for rectangular contacts, which prevents the contact from twisting, can be derived from the eight inequality constraints in (6) and (7). The four constraints in (6) render a set for the upper limit of perpendicular contact torque $\tau_{\perp}^{max}$, while the four constraints in (7) define a set for the lower limit of perpendicular contact torque $\tau_{\perp}^{min}$. By substituting the contact force using the eCMP definition (16) and the contact torque with its relation to the CoM torque (23), and then isolating the eCMP, we obtain

$$\boldsymbol{e} \cdot \underbrace{(\boldsymbol{\kappa}_1 + \boldsymbol{\kappa}_2 \times \boldsymbol{x})}_{\boldsymbol{n}_u} \geq \frac{b^2}{m} \boldsymbol{\tau}_c \cdot \boldsymbol{\kappa}_2 + \boldsymbol{x} \cdot \boldsymbol{\kappa}_1 \tag{36}$$

for the upper limit (6), and

$$\boldsymbol{e} \cdot \underbrace{(\boldsymbol{\kappa}_1 - \boldsymbol{\kappa}_2 \times \boldsymbol{x})}_{\boldsymbol{n}_l} \geq -\frac{b^2}{m} \boldsymbol{\tau}_c \cdot \boldsymbol{\kappa}_2 + \boldsymbol{x} \cdot \boldsymbol{\kappa}_1 \tag{37}$$

for the lower limit (7) of the perpendicular contact torque. Again, (36) and (37) include four half-space inequalities each, resulting from all permutations of the signs in $\boldsymbol{\kappa}_1$ and $\boldsymbol{\kappa}_2$. Each inequality constraint defines a plane, with the plane normal $\boldsymbol{n}_u$ for the upper limit or $\boldsymbol{n}_l$ for the lower limit. These planes define a half-space within which the eCMP must be located to satisfy the rotational friction constraint.

In the following, we will derive a geometric interpretation of these constraints. We focus our analysis on the four inequality constraints for the upper limit defined in (36); however, the same observations hold for the constraints in (37) as well.

We will demonstrate that all four planes in (36) intersect at a single point. Assuming constant angular momentum ($\boldsymbol{\tau}_c = \boldsymbol{0}$), this point is the CoM position. It can be verified that the CoM is an element of each of the four planes, by reformulating (36) as an equality constraint and choosing $\boldsymbol{e} = \boldsymbol{x}$ and $\boldsymbol{\tau}_c = \boldsymbol{0}$,

$$\begin{aligned} \boldsymbol{x} \cdot \underbrace{(\boldsymbol{\kappa}_1 + \boldsymbol{\kappa}_2 \times \boldsymbol{x})}_{\boldsymbol{n}_u} &= \boldsymbol{x} \cdot \boldsymbol{\kappa}_1, \\ \boldsymbol{x} \cdot \boldsymbol{\kappa}_1 + \underbrace{\boldsymbol{x} \cdot (\boldsymbol{\kappa}_2 \times \boldsymbol{x})}_{=0} &= \boldsymbol{x} \cdot \boldsymbol{\kappa}_1. \end{aligned} \tag{38}$$

Consequently, all planes resulting from the inequality constraint (36) intersect at the CoM position when the angular momentum is constant.

In addition, for $\boldsymbol{\tau}_c = \boldsymbol{0}$, each plane contains one vertex of the contact area and one corner of the friction pyramid intersecting the contact surface plane. We introduce the four vertices of the rectangular contact area as

$$\boldsymbol{p}^{ver} = \boldsymbol{n} \times \boldsymbol{\kappa}_1, \; \forall \sigma_1, \sigma_2, \tag{39}$$

which can be expressed as a function of the signs of σ_1 and σ_2 and the maximum extent of the surface area in x- and y-direction. The specific selection of the signs relates to the structure of $\boldsymbol{\kappa}_1$. To verify that each plane contains one element of $\boldsymbol{p}^{ver}$, we choose $\boldsymbol{e} = \boldsymbol{p}^{ver}$ and $\boldsymbol{\tau}_c = \boldsymbol{0}$ in the equality constraints derived from (36). For the lower limit in (37), we choose $\boldsymbol{e} = -\boldsymbol{p}^{ver}$.

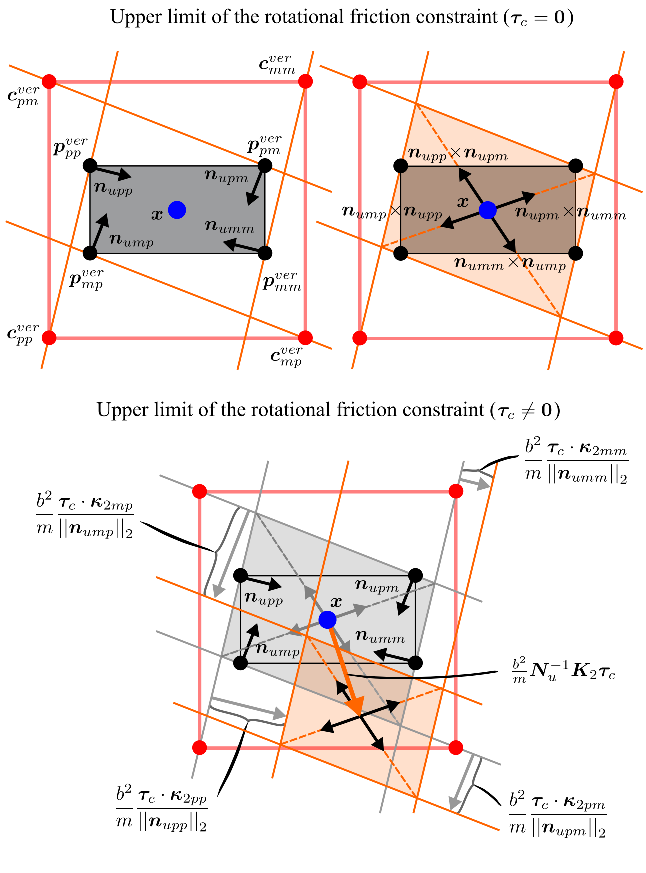

Figure 4. Top-down view of the upper limit of the rotational friction constraint. All quantities are expressed in the plane of the contact surface. In the upper two figures, a constant angular momentum ($\boldsymbol{\tau}_c = \boldsymbol{0}$) is assumed. Both figures show the same state of the robot but are separated into two figures for clarity of the presentation. The figure in the lower row visualizes the influence of a non-constant angular momentum ($\boldsymbol{\tau}_c \neq \boldsymbol{0}$) on all quantities. The black dots indicate the vertices of the contact area ($\boldsymbol{p}^{ver}$), and the red dots represent the vertices of the friction pyramid ($\boldsymbol{c}^{ver}$). The blue dot ($\boldsymbol{x}$) is the CoM position. The planes resulting from (36) with their normals $\boldsymbol{n}_{u\bullet\bullet}$ are visualized as orange lines. It can be verified that each plane intersects one vertex of the contact area and the friction pyramid. The line of intersection of two neighboring planes (dotted orange lines) is parallel to the cross-product of the respective plane normals. The orange area represents the set of feasible eCMP positions resulting from the upper limit of the rotational friction constraint. The gray arrows indicate the displacements of all points on the individual planes along their normal vectors as a function of the torque about the CoM ($\frac{b^2}{m}\boldsymbol{\tau}_c \cdot \boldsymbol{\kappa}_{2\bullet\bullet})/||\boldsymbol{n}_{u\bullet\bullet}||_2$. The displacement of the cone's apex ($\frac{b^2}{m}\boldsymbol{N}_u^{-1}\boldsymbol{K}_2\boldsymbol{\tau}_c$) is illustrated by the orange arrow.

Finally, we demonstrate that each plane in (36) also contains one vertex of the friction pyramid intersecting the plane of the contact area. These vertices of the friction pyramid are computed as

$$\boldsymbol{c}^{ver} = \boldsymbol{x} - (\boldsymbol{n} \cdot \boldsymbol{x})\boldsymbol{\kappa}_2, \; \forall \sigma_1, \sigma_2. \tag{40}$$

By choosing $\boldsymbol{e} = \boldsymbol{c}^{ver}$ and $\boldsymbol{\tau}_c = \boldsymbol{0}$ in the plane equations resulting from (36), it can be verified that each plane intersects one vertex of the friction pyramid, see Figure 4 for the upper limit and Figure 5 for the lower limit.

In (38), we verified that all planes intersect at the CoM position for a constant angular momentum. Now we will demonstrate that their intersection set forms a cone with

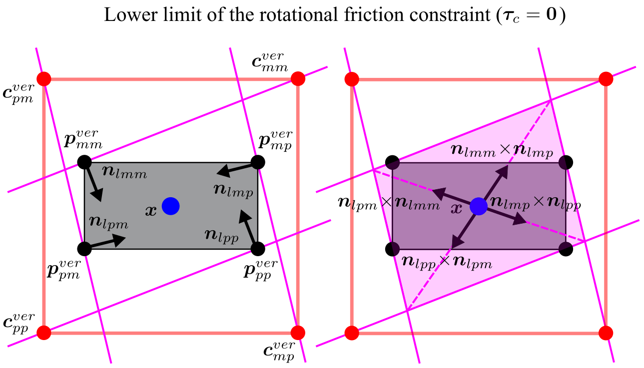

Figure 5. Top-down view of the lower limit of the rotational friction constraint corresponding to the upper row in Figure 4. All quantities of the lower limit (37) are shown in magenta. Note the different arrangement of the contact area vertices.

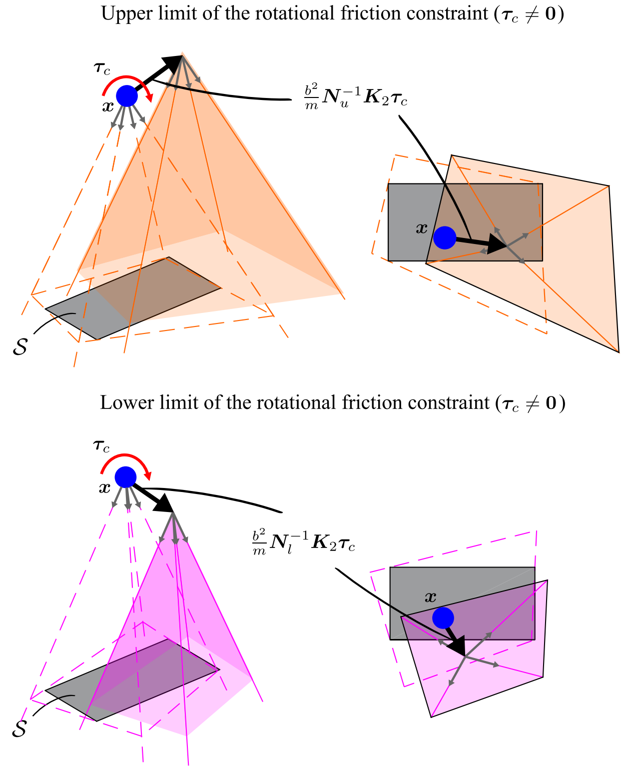

Figure 6. Set of feasible eCMP positions based on the rotational friction constraint shown in a 3D view (left) and a top-down view (right). The cones with quadrilateral bases, corresponding to the upper and lower perpendicular contact torque limits ($\tau_\perp^{max}$ and $\tau_\perp^{min}$), are shifted as a result of a torque about the CoM. The dashed lines indicate the cones for a state of constant angular momentum.

a quadrilateral base, assuming a sufficiently large friction coefficient $\tilde{\mu}$. We discuss the question of sufficiently large friction later in this section. In addition to identifying the apex of the cone as the CoM position, we need to derive the vectors that span the cone. Generally, the intersection of two planes forms a line that is perpendicular to the normal vectors of both planes. For example, we select two plane normals from (36), $\boldsymbol{n}_{upp}$ and $\boldsymbol{n}_{upm}$. The indices indicate the sign (plus or minus) of σ_1 and σ_2 in $\boldsymbol{\kappa}_1$ and $\boldsymbol{\kappa}_2$, e.g., $\boldsymbol{n}_{upp}$ corresponds to $\sigma_1 = \sigma_2 = 1$. The line of intersection between these two planes is parallel to the vector $\boldsymbol{n}_{upp} \times \boldsymbol{n}_{upm}$, which is orthogonal to both plane normals. The final cone is spanned by the four intersection rays of neighboring planes[3], i.e., we only take the cross product of plane normals that differ in either σ_1 or σ_2. Finally, by assuming $\boldsymbol{\tau}_c = \mathbf{0}$, we can conclude that the resulting intersection set from (36) resembles a cone with a quadrilateral base, projected from the CoM position towards the contact surface.

In the next step, we want to analyze how a torque about the CoM modulates the aforementioned cone. Since the plane normals $\boldsymbol{n}_u$ do not depend on $\boldsymbol{\tau}_c$, their cross-products, which span the cone and determine its internal angles, are independent of the torque about the CoM. However, a non-zero $\boldsymbol{\tau}_c$ shifts the planes defined in (36) along their normal vectors $\boldsymbol{n}_u$ by the distance $(\frac{b^2}{m}\boldsymbol{\tau}_c \cdot \boldsymbol{\kappa}_2)/||\boldsymbol{n}_u||_2$. For the resulting cone, this corresponds to a shift of its apex, while the internal angles are preserved, see Figure 6. This displacement of the cone's apex $\boldsymbol{x}^{dis} \in \mathbb{R}^3$ from the CoM position can be computed as a function of $\boldsymbol{\tau}_c$. Since all planes intersect at the apex position, we choose $\boldsymbol{e} = \boldsymbol{x} + \boldsymbol{x}^{dis}$ and concatenate three arbitrary plane equations defined in (36), as follows:

$$\underbrace{\begin{bmatrix} \boldsymbol{n}_{upp}^T \\ \boldsymbol{n}_{upm}^T \\ \boldsymbol{n}_{ump}^T \end{bmatrix}}_{\boldsymbol{N}_u} (\boldsymbol{x} + \boldsymbol{x}^{dis}) = \frac{b^2}{m} \underbrace{\begin{bmatrix} \boldsymbol{\kappa}_{2pp}^T \\ \boldsymbol{\kappa}_{2pm}^T \\ \boldsymbol{\kappa}_{2mp}^T \end{bmatrix}}_{\boldsymbol{K}_2} \boldsymbol{\tau}_c + \underbrace{\begin{bmatrix} \boldsymbol{\kappa}_{1pp}^T \\ \boldsymbol{\kappa}_{1pm}^T \\ \boldsymbol{\kappa}_{1mp}^T \end{bmatrix}}_{\boldsymbol{K}_1} \boldsymbol{x} \tag{41}$$

and solve for the apex displacement from the CoM position

$$\boldsymbol{x}^{dis} = \frac{b^2}{m} \boldsymbol{N}_u^{-1} \boldsymbol{K}_2 \boldsymbol{\tau}_c. \tag{42}$$

It can be verified by evaluating the scalar triple product that $\boldsymbol{N}_u \boldsymbol{x} = \boldsymbol{K}_1 \boldsymbol{x}$. Consequently, the cone's apex is shifted as a function of $\boldsymbol{\tau}_c$ in the direction defined by the matrix $\boldsymbol{N}_u^{-1}\boldsymbol{K}_2$ and is generally not aligned with the axes of the contact frame. Finally, the constraint for the upper perpendicular contact torque limit (36) can be expressed as set membership

$$\boldsymbol{e} \in \Big\{ \boldsymbol{x} + \frac{b^2}{m} \boldsymbol{N}_u^{-1} \boldsymbol{K}_2 \boldsymbol{\tau}_c + \boldsymbol{e}' \;\Big|\; \boldsymbol{e}' \in \operatorname{cone}\Big(\{ \boldsymbol{n}_{upp} \times \boldsymbol{n}_{upm},\ \boldsymbol{n}_{upm} \times \boldsymbol{n}_{umm},\ \boldsymbol{n}_{umm} \times \boldsymbol{n}_{ump},\ \boldsymbol{n}_{ump} \times \boldsymbol{n}_{upp} \} \Big) \Big\}. \tag{43}$$

The eCMP must belong to the conical hull of the cross-products of the plane normals $\boldsymbol{n}_{u\bullet\bullet}$ ($\bullet \in \{p, m\}$) with its apex at the CoM position, shifted based on the torque about the CoM.

A second set membership with the same properties results from the lower limit in (37)

$$\boldsymbol{e} \in \Big\{ \boldsymbol{x} + \frac{b^2}{m} \boldsymbol{N}_l^{-1} \boldsymbol{K}_2 \boldsymbol{\tau}_c + \boldsymbol{e}' \;\Big|\; \boldsymbol{e}' \in \operatorname{cone}\Big(\{ \boldsymbol{n}_{lpp} \times \boldsymbol{n}_{lpm},\ \boldsymbol{n}_{lpm} \times \boldsymbol{n}_{lmm},\ \boldsymbol{n}_{lmm} \times \boldsymbol{n}_{lmp},\ \boldsymbol{n}_{lmp} \times \boldsymbol{n}_{lpp} \} \Big) \Big\}. \tag{44}$$

The final eCMP set corresponding to the rotational friction constraints is determined by the intersection set of the two cones (43) and (44), see Figure 6.

Note that, assuming constant angular momentum, it can be shown that the intersection set resulting from the CoP and translational friction constraints is a subset of the rotational friction constraint set as pointed out by Caron and Kheddar (2017); however, this property does not necessarily hold for $\boldsymbol{\tau}_c \neq \mathbf{0}$. A detailed proof is beyond the scope of this work.

3.4. Instantaneous DCM Error Convergence

In addition to the three introduced sets resulting from the contact constraints (CoP, translational, and rotational friction), we want to derive a fourth set corresponding to dynamic stability. In this work, dynamic stability refers to the properties of the DCM dynamics. A system is dynamically stable for a given state if the DCM error is converging at that instant, i.e., if it exhibits *instantaneous DCM error convergence*. Note that, unlike the previous sets, the eCMP set corresponding to dynamic stability is independent of contact constraints and depends solely on the DCM dynamics.

To formalize the condition of dynamic stability, we introduce a quadratic error function

$$V = \frac{1}{2}\Delta\boldsymbol{\xi} \cdot \Delta\boldsymbol{\xi} \tag{45}$$

with its time derivative

$$\dot{V} = \Delta\boldsymbol{\xi} \cdot \Delta\dot{\boldsymbol{\xi}}. \tag{46}$$

Instantaneous DCM error convergence for a given state is ensured when the dot product of the DCM position error and DCM velocity error is negative, i.e., $\dot{V} < 0$. This implies that the DCM position error at the next instance of time is smaller than the current one. Consequently, we can identify feasible eCMP positions that ensure dynamic stability. We reformulate the DCM dynamics (13) in error space and insert the VRP to eCMP relation (18) to obtain

$$\Delta\dot{\boldsymbol{\xi}} = \frac{1}{b}(\Delta\boldsymbol{\xi} - \Delta\boldsymbol{e}), \tag{47}$$

introducing the eCMP offset $\Delta\boldsymbol{e} = \boldsymbol{e} - \boldsymbol{e}^d$. Inserting (47) into the time derivative of the quadratic error function (46) leads to

$$\dot{V} = \frac{1}{b}(\Delta\boldsymbol{\xi} \cdot \Delta\boldsymbol{\xi} - \Delta\boldsymbol{\xi} \cdot \Delta\boldsymbol{e}) < 0. \tag{48}$$

We use the dynamic stability constraint ($\dot{V} < 0$) to derive a geometrical interpretation in the form of feasible eCMP positions that ensure this condition. By reformulating (48), we obtain the following inequality constraint for the eCMP position

$$\frac{\Delta\boldsymbol{\xi}}{||\Delta\boldsymbol{\xi}||_2} \cdot \Delta\boldsymbol{e} > ||\Delta\boldsymbol{\xi}||_2, \tag{49}$$

which ensures instantaneous DCM error convergence for a given absolute DCM error $||\Delta\boldsymbol{\xi}||_2 > 0$. The geometrical meaning is that the projection of the eCMP offset along the normalized direction of the DCM error needs to be larger than the norm of the DCM error, see Figure 7.

For the set of eCMPs that ensure instantaneous convergence of the DCM error, we conclude that the eCMP

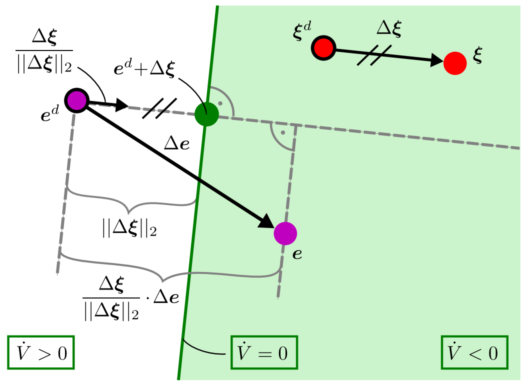

Figure 7. The set of eCMP positions corresponding to instantaneous DCM error convergence is represented by the green area. The view is oriented perpendicular to the DCM error vector ($\Delta\boldsymbol{\xi}$) and an example eCMP position ($\boldsymbol{e}$) is chosen for illustration. The quantities encircled in black represent the desired values. The plane that defines the half-space of eCMP positions that lead to $\dot{V} < 0$, i.e., instantaneous convergence of the DCM error, passes through the point $\boldsymbol{e}^d + \Delta\boldsymbol{\xi}$ (green dot) and has a normal vector parallel to the DCM error vector. This plane is visualized by the dark green line. All eCMP points on this plane result in $\dot{V} = 0$, indicating a marginally stable DCM error. The dot product of the normalized DCM error $\Delta\boldsymbol{\xi}/||\Delta\boldsymbol{\xi}||_2$ and the eCMP offset $\Delta\boldsymbol{e} = \boldsymbol{e} - \boldsymbol{e}^d$ represents the projection of $\boldsymbol{e}$ along the direction of $\boldsymbol{\xi}$. If this dot product is greater than the norm of the DCM error ($||\Delta\boldsymbol{\xi}||_2$), the eCMP $\boldsymbol{e}$ is located in the half-space that ensures instantaneous DCM error convergence.

needs to be located such that a plane, which contains the point $\boldsymbol{e}^d + \Delta\boldsymbol{\xi}$ and is orthogonal to $\Delta\boldsymbol{\xi}$, intersects a line segment between the actual eCMP $\boldsymbol{e}$ and the desired one $\boldsymbol{e}^d$. All points on this plane correspond to $\dot{V} = 0$. By expressing (49) as set membership, we obtain

$$\boldsymbol{e} \in \{\boldsymbol{e}^d + \Delta\boldsymbol{\xi} + \boldsymbol{e}' \mid \boldsymbol{e}' \in \mathbb{R}^3,\ \Delta\boldsymbol{\xi} \cdot \boldsymbol{e}' > 0\}. \tag{50}$$

For the particular choice of the DCM controller presented in Section 2.3.3, it can be easily verified that the commanded eCMP from the proposed control law in (22) fulfills the conditions for instantaneous DCM error convergence. By expanding (22), we obtain:

$$\boldsymbol{e}^{cmd} = \boldsymbol{e}^d + \Delta\boldsymbol{\xi} + b\boldsymbol{K}_\xi \Delta\boldsymbol{\xi}. \tag{51}$$

Since the DCM control gain matrix $\boldsymbol{K}_\xi$ is diagonal and positive definite, it can be verified that $\Delta\boldsymbol{\xi} \cdot b\boldsymbol{K}_\xi \Delta\boldsymbol{\xi} > 0$. Therefore, $\boldsymbol{e}^{cmd}$ always belongs to the set defined in (50).

Assuming the diagonal elements of $\boldsymbol{K}_\xi$ are identical, the commanded eCMP is located on a ray with its origin at $\boldsymbol{e}^d + \Delta\boldsymbol{\xi}$ and in direction of $\Delta\boldsymbol{\xi}$ (purple dotted line in Figure 8). The distance between the desired and the commanded eCMP depends on the values of $\boldsymbol{K}_\xi$. With increasing $\boldsymbol{K}_\xi$, the distance increases as well as the convergence rate of the DCM error (47). For $\boldsymbol{K}_\xi = \mathbf{0}$ the commanded eCMP coincides with the point $\boldsymbol{e}^d + \Delta\boldsymbol{\xi}$ and the DCM error is marginally stable, see Figure 8.

For balancing, dynamic stability can be related to 0-step capturability (Del Prete et al. 2018), which implies that the robot can come to a stop without altering the contact configuration. In tracking scenarios, dynamic stability determines whether the DCM tracking error, resulting from deviations of a desired trajectory, is converging for a given

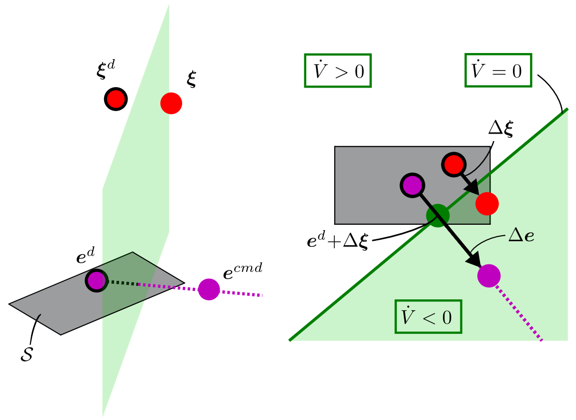

Figure 8. Set of eCMP positions ensuring an instantaneous DCM error convergence shown in a 3D view (left) and a top-down view (right). The quantities encircled in black represent the desired values. The purple dotted line results from the DCM control law (22) for varying values of $\boldsymbol{K}_\xi$ assuming the diagonal elements of $\boldsymbol{K}_\xi$ are identical and positive.

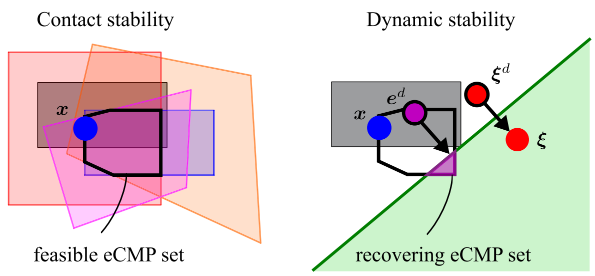

Figure 9. Top-down view illustrating the feasible and recovering eCMP sets. Left: Feasible eCMP sets of the CoP constraint (blue), the translational friction constraint (red), and the upper (orange) and lower (magenta) limits of the rotational friction constraint. The resulting feasible eCMP set, which ensures contact stability, is the intersection of these sets and is highlighted in black. Right: eCMP positions that ensure instantaneous DCM error convergence (green) and their intersection with the resulting feasible eCMP set, highlighted in purple. All eCMP positions within this recovering eCMP set ensure both contact and dynamic stability.

state. This analysis is independent of contact stability or the properties of the desired trajectory, focusing solely on deriving a set of eCMP positions that ensure instantaneous DCM error convergence.

3.5. *Feasible and Recovering eCMP Set*

First, we derived three independent sets of feasible eCMP positions w.r.t. the CoP, translational friction, and rotational friction constraints. The intersection of these three sets is referred to as the resulting *feasible eCMP set*. All eCMP positions within this set ensure contact stability for a given state. In addition, we derived a fourth set corresponding to dynamic stability that ensures instantaneous DCM error convergence. The intersection of all four sets is referred to as the *recovering eCMP set*, see Figure 9.

If this set is not empty for a given state, a feasible eCMP position exists, i.e., an external CoM force, that can be generated within the contact constraints of the end effectors. Furthermore, this eCMP position ensures that the DCM error is converging for that particular state. If the recovering eCMP set is not empty throughout an entire trajectory, the trajectory can be considered to exhibit both contact and dynamic stability.

4. Modulation of eCMP Sets

To ensure stable locomotion, the commanded eCMP must be within the recovering eCMP set. However, there are scenarios, such as after a disturbance, where the recovering eCMP set is empty, i.e., the eCMP cannot be placed in such a way that the contact stability is maintained and the DCM error is converging simultaneously. In such cases, the individual eCMP sets can be modulated, for example, by applying a torque about the CoM or varying the eCMP height in order to obtain an intersection solution, where the resulting eCMP satisfies contact and dynamic stability.

In general locomotion scenarios, the direction parallel to the gravitational vector is less critical for contact and dynamic stability, as gravity naturally retains the CoM in the proximity of the contact area. The forces the robot can generate in the direction parallel to the gravitational vector are typically much larger than those it can generate perpendicular to it. However, contact constraints impose an upper limit on the horizontal forces the robot can exert on the environment.

Therefore, we reformulate the eCMP sets derived in Section 3 for the horizontal eCMP position (in xy-direction) as a function of the vertical component of the eCMP ($\boldsymbol{e}_z$) and the torque about the CoM ($\boldsymbol{\tau}_c$). These two quantities serve as input parameters for modulating the horizontal eCMP sets, with the aim of extending the resulting feasible eCMP set and recovering eCMP set in a desired direction.

4.1. *Horizontal eCMP sets*

In the following, we reformulate the eCMP sets corresponding to contact stability ((30), (35), (43), and (44)), and the eCMP set associated with dynamic stability (50) in the horizontal plane. The 3D sets from Section 3 reduce to 2D sets for the horizontal eCMP $\boldsymbol{e}_{xy} \in \mathbb{R}^2$. The 2D set represents a cross-section of the 3D set at the height of $\boldsymbol{e}_z$. Note that the reduction to a 2D set is not an assumption made to simplify the problem. The 2D set can be defined at an arbitrary height and therefore necessitates the use of the 3D-DCM formulation.

In order to simplify notation and explicitly formulate $\boldsymbol{e}_{xy}$ as a function of $\boldsymbol{e}_z$, we assume in this section that the world frame is located in the plane of the contact surface and that the contact normal is opposite to the gravitational vector, $\boldsymbol{n} = (0, 0, 1)^T$. Moreover, we assume that the vectors $\boldsymbol{t}_x$ and $\boldsymbol{t}_y$ are aligned with the x- and y-axes of the world frame, i.e., $\boldsymbol{t}_x = (1, 0, 0)^T$ and $\boldsymbol{t}_y = (0, 1, 0)^T$. While the presented relations still hold without these assumptions, they become less intuitive.

CoP Constraint: The eCMP set corresponding to the CoP constraint (30) can be expressed as

$$\begin{aligned} \boldsymbol{e}_{xy} \in \bigg\{ & \Big(1 - \frac{\boldsymbol{e}_z}{\boldsymbol{x}_z}\Big)\boldsymbol{p}_{xy} + \frac{\boldsymbol{e}_z}{\boldsymbol{x}_z}\boldsymbol{x}_{xy} \\ & - \frac{b^2}{m\boldsymbol{x}_z}(-\boldsymbol{\tau}_{c,y}, \boldsymbol{\tau}_{c,x})^T \;\Big|\; \boldsymbol{p}_{xy} \in \mathcal{S}_{xy} \bigg\}, \end{aligned} \tag{52}$$

where the CoP needs to be within the contact area, $\boldsymbol{p}_{xy} \in \mathcal{S}_{xy}$.

Translational Friction Constraint: Moreover, the linearized translational friction constraint (35) reduces to

$$\boldsymbol{e}_{xy} \in \left\{ \boldsymbol{x}_{xy} + \boldsymbol{e}' \,\middle|\, \boldsymbol{e}' \in \operatorname{conv}\left(\left\{ \tilde{\mu}(\boldsymbol{x}_z - \boldsymbol{e}_z)(\pm 1, \pm 1)^T \right\} \right) \right\}, \tag{53}$$

where the convex hull[4] is formed by the vertices of the friction pyramid at the height of the vertical eCMP position. Here, $2\tilde{\mu}(\boldsymbol{x}_z - \boldsymbol{e}_z)$ represents the edge length of the square cross-section of the friction pyramid and the horizontal plane at the height of $\boldsymbol{e}_z$.

Rotational Friction Constraint: To simplify the notation, we introduce the following auxiliary variables, which represent the vectors that span the cone of the rotational friction constraint set in (43)

$$\begin{aligned} \boldsymbol{n}_{u1} &= \boldsymbol{n}_{upp} \times \boldsymbol{n}_{upm}, \quad \boldsymbol{n}_{u2} = \boldsymbol{n}_{upm} \times \boldsymbol{n}_{umm}, \\ \boldsymbol{n}_{u3} &= \boldsymbol{n}_{umm} \times \boldsymbol{n}_{ump}, \, \boldsymbol{n}_{u4} = \boldsymbol{n}_{ump} \times \boldsymbol{n}_{upp}. \end{aligned} \tag{54}$$

The horizontal eCMP set can be expressed as follows:

$$\boldsymbol{e}_{xy} \in \left\{ \boldsymbol{x}_{xy} + \frac{b^2}{m}(\boldsymbol{N}_u^{-1}\boldsymbol{K}_2\boldsymbol{\tau}_c)_{xy} + \boldsymbol{e}' \,\middle|\, \boldsymbol{e}' \in \eta_u \operatorname{conv}\left(\left\{ \frac{\boldsymbol{n}_{u1,xy}}{\boldsymbol{n}_{u1,z}}, \frac{\boldsymbol{n}_{u2,xy}}{\boldsymbol{n}_{u2,z}}, \frac{\boldsymbol{n}_{u3,xy}}{\boldsymbol{n}_{u3,z}}, \frac{\boldsymbol{n}_{u4,xy}}{\boldsymbol{n}_{u4,z}} \right\} \right) \right\}. \tag{55}$$

The scalar η_u scales the convex set of cone-spanning vectors projected onto a horizontal plane, depending on the height of $\boldsymbol{e}_z$ and the torque about the CoM $\boldsymbol{\tau}_c$

$$\eta_u = \boldsymbol{e}_z - \boldsymbol{x}_z - \frac{b^2}{m}(\boldsymbol{N}_u^{-1}\boldsymbol{K}_2\boldsymbol{\tau}_c)_z. \tag{56}$$

We only present the eCMP set corresponding to the upper limit of the perpendicular contact torque. The eCMP set corresponding to the lower limit (44) can be derived equivalently.

Instantaneous DCM Error Convergence Constraint: Finally, the eCMP set, which ensures dynamic stability (50), can be expressed for the horizontal plane as follows:

$$\boldsymbol{e}_{xy} \in \{ \boldsymbol{e}_{xy}^d + \Delta\boldsymbol{\xi}_{xy} + \boldsymbol{e}' \mid \boldsymbol{e}' \in \mathbb{R}^2, \Delta\boldsymbol{\xi}_{xy} \cdot \boldsymbol{e}' > 0 \}. \tag{57}$$

Note that this set is independent of $\boldsymbol{e}_z$ and $\boldsymbol{\tau}_c$.

4.2. Modulation of eCMP Sets in the Context of Humanoid Push Recovery

The modulation of the eCMP sets in response to an external disturbance can be interpreted in the context of humanoid push recovery. In the following, we will vary the values of the input variables $\boldsymbol{e}_z$ and $\boldsymbol{\tau}_c$ in (52), (53), and (55). Depending on the input values, the set modulation can be interpreted as an ankle, hip, or height-variation strategy. The step strategy manifests through an extended contact area $\mathcal{S}_{xy}$ by changing the contact configuration and an adjusted DCM trajectory $\boldsymbol{\xi}^d$ in (57).

4.2.1. Ankle Strategy. ($\boldsymbol{e}_z = 0, \boldsymbol{\tau}_c = \boldsymbol{0}$). Using a pure ankle strategy, we assume a constant CoM height, i.e., the eCMP is placed on the ground ($\boldsymbol{e}_z = 0$). From (17), we can verify that the vertical CoM acceleration is zero when $\boldsymbol{e}_z = 0$ and the CoM has a height of $\boldsymbol{x}_z = \Delta z$. Additionally, for this strategy, it is typical to assume a constant angular momentum about the CoM, $\boldsymbol{\tau}_c = \boldsymbol{0}$.

CoP Constraint: By applying these assumptions to (52), we can verify that the eCMP coincides with the CoP position. Consequently, the eCMP is constrained to lie within the contact area $\mathcal{S}_{xy}$.

Translational Friction Constraint: Moreover, the edge length of the cross-section of the friction pyramid in (53) simplifies to $2\tilde{\mu}\boldsymbol{x}_z$, since $\boldsymbol{e}_z = 0$.

Rotational Friction Constraint: The eCMP set in (55) reduces to the convex hull of the cone-spanning vectors projected on the horizontal plane. The resulting eCMP sets are shown in the first row of Figure 10.

4.2.2. Hip Strategy. ($\boldsymbol{e}_z = 0, \boldsymbol{\tau}_c \neq \boldsymbol{0}$). The hip strategy refers to an active change of the system's angular momentum by inducing a torque about the CoM, which is typically realized by moving the robot's upper body. This strategy is particularly advantageous when the CoP constraint is active. It is usually combined with the ankle strategy, assuming a constant CoM height, $\boldsymbol{e}_z = 0$.

CoP Constraint: By substituting $\boldsymbol{e}_z = 0$ into (52), we can verify that the hip strategy shifts the eCMP set, while preserving the size of the contact area, by the offset of $-\frac{b^2}{m\boldsymbol{x}_z}(-\boldsymbol{\tau}_{c,y}, \boldsymbol{\tau}_{c,x})^T$.

Translational Friction Constraint: Since the translational friction constraint (53) is independent of the torque about the CoM, the corresponding eCMP set cannot be influenced by the hip strategy and is identical to that of the ankle strategy.

Rotational Friction Constraint: For the rotational friction constraint (55), the applied torque also causes a translational shift of the feasible eCMP set in the direction $\boldsymbol{N}_u^{-1}\boldsymbol{K}_2\boldsymbol{\tau}_c$. Since this shift is not necessarily parallel to the contact plane, the torque about the CoM results in a horizontal shift by the offset $(\boldsymbol{N}_u^{-1}\boldsymbol{K}_2\boldsymbol{\tau}_c)_{xy}$ and the size of the quadrilateral base is scaled by the factor $(\boldsymbol{N}_u^{-1}\boldsymbol{K}_2\boldsymbol{\tau}_c)_z$. It is important to note that, unlike the CoP constraint, the perpendicular torque about the CoM $\boldsymbol{\tau}_z$ also modulates the feasible eCMP set. The influence of torque about the CoM on the eCMP sets is shown in the middle row of Figure 10.

Note that in contrast to the ankle strategy, the effect of the hip strategy is temporally limited. The angular momentum cannot be increased and sustained indefinitely due to the system's kinematic and dynamic limitations. When the angular momentum is reduced again, a CoM torque with an inverted sign is induced, shifting the feasible eCMP set in the opposite direction.

4.2.3. Height-variation Strategy. ($\boldsymbol{e}_z < 0, \boldsymbol{\tau}_c = \boldsymbol{0}$). The height-variation strategy relates to modulating the feasible eCMP set by changing the CoM height. In particular, lowering the eCMP ($\boldsymbol{e}_z < 0$) results in increased upward acceleration of the CoM, thereby expanding the feasible horizontal eCMP set. The physical intuition behind this strategy is that higher vertical contact force enables higher transferable horizontal forces and torques. The height-variation strategy shifts the cross-section of the 3D sets below the contact surface to a height of $\boldsymbol{e}_z$.

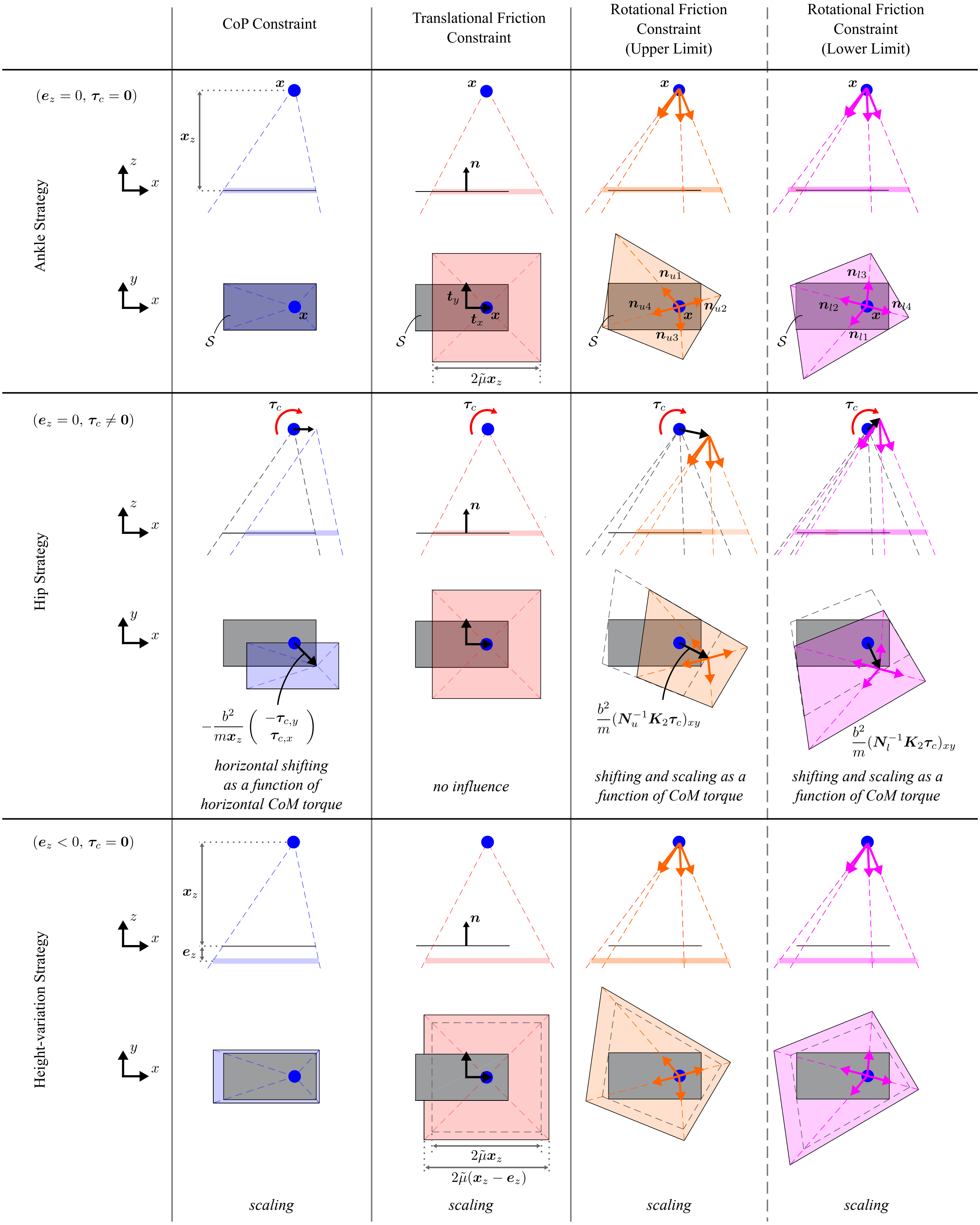

Figure 10. Visualization of eCMP sets in both side and top-down views. The first column corresponds to the CoP constraint in (52), the second column shows the translational friction constraint from (53), and the last two columns represent the upper and lower rotational friction constraints (55). The first row illustrates the ankle strategy, the second row shows the influence of a torque about the CoM corresponding to the hip strategy, and the last row depicts the influence of a lowered vertical eCMP position as a height-variation strategy. The gray dashed lines in the middle and lower rows represent the initial ankle set $(e_z = 0,\ \tau_c = 0)$, to better visualize the effects of the respective strategy.

CoP Constraint: By substituting $\boldsymbol{e}_z < 0$ and $\boldsymbol{\tau}_c = \boldsymbol{0}$ into (52), the height-variation strategy results in an increased feasible eCMP set with the size of the contact area, scaled by the factor $1 - \frac{\boldsymbol{e}_z}{\boldsymbol{x}_z}$ and horizontally shifted by the offset $\frac{\boldsymbol{e}_z}{\boldsymbol{x}_z}\boldsymbol{x}_{xy}$.

Translational Friction Constraint: The edge length of the corresponding eCMP set in (53) is extended by the value $-2\tilde{\mu}\boldsymbol{e}_z$ compared to the ankle strategy.

Rotational Friction Constraint: Similar to the translational friction constraint, a height-variation strategy scales the set of the rotational friction constraint (55) in the directions of the vectors that span the convex hull by increasing the magnitude of η_u. The corresponding sets are visualized in the lower row of Figure 10.

Note that the height-variation strategy is particularly important when the translational friction constraint is the limiting factor, as inducing angular momentum or taking a step (which increases the contact area) has no effect in such cases. Possible scenarios are locomotion on slippery ground (with a low friction coefficient) or configurations with a large contact area, such as double support. Similar to the hip strategy, accelerating the CoM upward to expand the horizontal eCMP set is temporally limited due to kinematic constraints, followed by a shrinking of the feasible eCMP set.

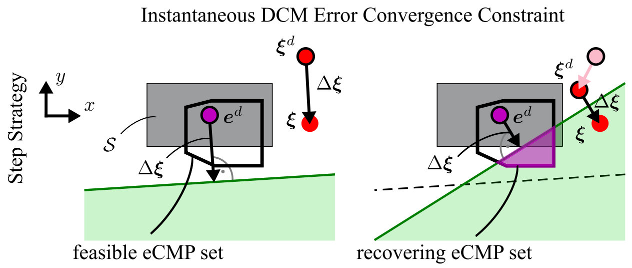

Figure 11. Visualization from a top-down view of the eCMP set corresponding to the instantaneous DCM error convergence constraint in (57), as well as the influence of the step strategy on this set. The left side illustrates the initial state with a significant DCM error $\Delta\boldsymbol{\xi}$. For this state, the feasible eCMP set, defined as the intersection of all contact constraint sets, is shown, while the recovering eCMP set is empty. The right side shows the state after a step adjustment and a corresponding DCM reference update (the initial desired DCM position is shown in pink). As a result, the DCM error is reduced, and the eCMP set, determined by the DCM error convergence constraint (green area), is modulated due to the change in the $\Delta\boldsymbol{\xi}$ vector. Consequently, the recovering eCMP set is no longer empty, and an eCMP position exists that ensures contact and dynamic stability. The gray dashed line indicates the boundary of the eCMP set before the DCM reference trajectory adjustment. The time evolution of the DCM reference trajectory resulting from the step strategy can be found in Figure 17.

4.2.4. Step Strategy. In addition to the previous strategies, changing the contact configuration can also increase the feasible eCMP set. While the constraint resulting from the translational friction (53) depends solely on the CoM and vertical eCMP position, the eCMP sets related to the CoP constraint (52) and the rotational friction constraint (55) can be extended by increasing $\mathcal{S}_{xy}$.

Instantaneous DCM Error Convergence Constraint: Moreover, the step strategy modulates the eCMP set resulting from the DCM error convergence constraint (57). In particular, the DCM reference trajectory $\boldsymbol{\xi}^d$ is a function of the future step positions. Adjusting the step position influences the current DCM reference trajectory, altering the term $\Delta\boldsymbol{\xi}_{xy}$ in (57) and thereby modulating the corresponding feasible eCMP set until the recovering eCMP set is no longer empty, see Figure 11. Examples of such algorithms can be found in Jeong et al. (2019); Khadiv et al. (2020); Mesesan et al. (2021); Egle et al. (2023). One specific approach of step adjustment based on Mesesan et al. (2021) will be presented in Section 5.2.

In contrast to the hip and height-variation strategy, the step strategy is not temporally constrained by the need for a reduced feasible eCMP set to follow an increased one in the relevant direction. The step strategy can be applied arbitrarily often, provided that the system's kinematic and dynamic limits are not exceeded and the terrain permits adjustments to the step position.

All strategies can be combined to maximize the effect of increasing the feasible and recovering eCMP sets. Note that the hip, height-variation, and step strategy are generally coupled and influence each other through whole-body coupling effects. For instance, lowering the CoM height or moving the swing leg to take a step induces angular momentum itself, while generating angular momentum with the upper body can affect the overall CoM height of the system.

4.3. Numerical Computation of Horizontal Feasible eCMP Sets

The feasible sets presented in Section 3 can be computed analytically under the assumption of a single contact. Given two or more contacts, the distribution of desired CoM wrenches among the contacts complicates the computation of feasible eCMP sets due to the nullspace in the distribution. Typically, this problem is addressed by formulating the wrench distribution problem as a constrained quadratic program (QP), subject to the contact constraints defined for each contact. Note that the eCMP set corresponding to the instantaneous DCM error convergence constraint is independent of the contact configuration and thus can always be computed analytically.

As in Section 4.2, the algorithm for computing the horizontal feasible eCMP sets takes a given $\boldsymbol{e}_z$ and $\boldsymbol{\tau}_c$ as input and optimizes the contact forces and torques at each contact, which must sum to the given vertical eCMP position and torque about the CoM, to find the feasible eCMP set boundary. Note that the following algorithm computes the horizontal feasible eCMP sets for arbitrary values of the physical quantities $\boldsymbol{e}_z$ and $\boldsymbol{\tau}_c$, and is not tied to any specific control scheme at this stage. The eCMP is obtained directly from the contact forces by substituting the eCMP definition (16) into the resultant CoM force (11)

$$\boldsymbol{e} = \boldsymbol{x} - \frac{b^2}{m}\sum_{i=1}^{p}\boldsymbol{f}_i. \tag{58}$$

Correspondingly, based on (1), the contact wrenches relate to the resulting CoM torque as follows:

$$\boldsymbol{\tau}_c = \sum_{i=1}^{p} (\boldsymbol{f}_i \times \boldsymbol{x}_{ic} + \boldsymbol{\tau}_i). \tag{59}$$

We propose to formulate a QP that outputs a boundary point of the feasible eCMP set for a desired direction $\boldsymbol{a} \in \mathbb{R}^3$ in the horizontal plane, i.e., perpendicular to the gravity vector and in the nullspace consistent with the given $\boldsymbol{e}_z$ and $\boldsymbol{\tau}_c$. By sampling multiple directions on a circle, we obtain a boundary point approximation of the feasible set.

First, we define an unconstrained horizontal eCMP position $\boldsymbol{e}^u_{xy}$, which encodes the direction of $\boldsymbol{a}$ relative to the desired eCMP $\boldsymbol{e}^d_{xy}$:

$$\boldsymbol{e}^u_{xy} = \boldsymbol{e}^d_{xy} + \beta \boldsymbol{a}_{xy}. \tag{60}$$

Here, $\beta \geq 0$ is a large scalar value that ensures $\boldsymbol{e}^u_{xy}$ is outside the feasible set, allowing the QP to find its projection onto the boundary of the feasible set. We choose the desired eCMP as the origin, assuming it is planned to be located within the feasible eCMP set. Otherwise, a candidate point within the feasible set can be found from the analytical constraints for a single contact. Finally, the QP is formulated as follows:

$$\min_{\boldsymbol{f}_i,\, \boldsymbol{\tau}_i} \; ||\boldsymbol{e}^u_{xy} - \boldsymbol{e}^c_{xy}||_{Q_1} + \Big|\Big|\boldsymbol{e}_z - \boldsymbol{x}_z + \frac{b^2}{m}\sum_{i=1}^{p} \boldsymbol{f}_{i,z}\Big|\Big|_{Q_2}$$
$$+ \Big|\Big|\boldsymbol{\tau}_c - \sum_{i=1}^{p} (\boldsymbol{f}_i \times \boldsymbol{x}_{ic} + \boldsymbol{\tau}_i)\Big|\Big|_{Q_3} + \sum_{i=1}^{p} (||\boldsymbol{f}_i||_{Q_r} + ||\boldsymbol{\tau}_i||_{Q_r}), \tag{61}$$

with

$$\boldsymbol{e}^c_{xy} = \boldsymbol{x}_{xy} - \frac{b^2}{m}\sum_{i=1}^{p} \boldsymbol{f}_{i,xy}, \tag{62}$$

and solved subject to the contact constraints (2)-(5). Here, $\boldsymbol{e}^c_{xy}$ is the resulting constrained eCMP on the boundary of the feasible eCMP.

The first task $Q_1 > 0$ aims to realize the unconstrained horizontal eCMP, while the second and third tasks $Q_2, Q_3 >> 0$, which have the highest task weights, enforce that the given $\boldsymbol{e}_z$ and $\boldsymbol{\tau}_c$ are realized via (58) and (59). The last two tasks $Q_r > 0$ regulate the contact forces and torques. Note that the resulting constrained eCMP $\boldsymbol{e}^c_{xy}$ is an orthogonal projection onto the boundary of the feasible eCMP set, see Figure 12.

We choose contact wrenches as optimization variables because the contact constraints in Section 2.2 apply to them directly. This formulation also allows enforcing only a subset of constraints when desired. For example, to compute the eCMP set induced by the CoP constraint, we include only that constraint in the optimization.

The entire boundary of the feasible set can be sampled by rotating $\boldsymbol{a}$ around the vertical axis. Following Abdalla et al. (2023), an inner approximation of the set can also be constructed as a convex hull based on the direction vector and the projected boundary point.

5. Application to Push Recovery

So far, we have demonstrated how push recovery reaction strategies can modulate the feasible and recovering eCMP sets to ensure contact and dynamic stability. In this section, we propose a push recovery algorithm that leverages this knowledge for legged robot systems.

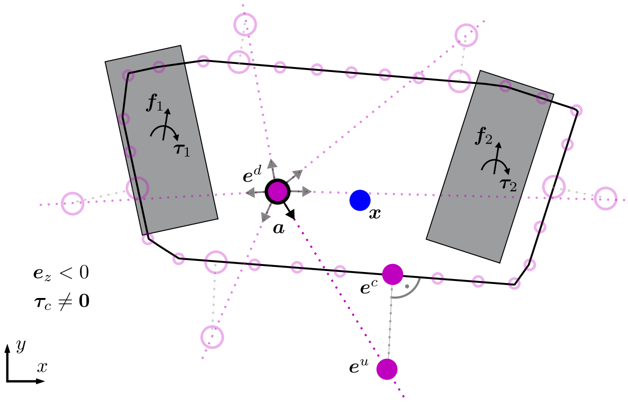

Figure 12. Visualization of feasible eCMP set computation under contact constraints in double support. The black polygon displays the boundary of the feasible eCMP set computed based on (61) in a state of non-zero torque about the CoM and an eCMP located below the ground. The circles illustrate the sampling of the entire set by rotating $\boldsymbol{a}$ around the vertical axis.

As discussed in Section 4, the ankle, hip, and height-variation strategies modulate the feasible eCMP set itself, while the step strategy adjusts the reference DCM trajectory. Consequently, we implement the first three strategies at a DCM control level, while the step strategy is computed at the step planning level. The step strategy is designed to compensate for as much of the DCM error as possible by the end of the step, whereas the hip and height-variation strategies are employed minimally, solely to prevent the DCM error from diverging. This distinction arises from the individual characteristics of the reaction strategies. The hip and height-variation strategies are time-limited because the induced angular momentum and vertical CoM acceleration must eventually be reduced. In contrast, the step strategy is not time-constrained and can be employed within the system's kinematic and dynamic limits, provided that the high-level task and terrain permit adjustments to the step position.

Note that our motivation for employing the height-variation strategy stems from the analysis in Section 4.2.3, as there are scenarios in which only the height-variation strategy can extend the feasible eCMP set, i.e., when the translational friction constraint is the limiting factor. All strategies are active simultaneously and operate in parallel. Their activation and scheduling are governed by the dynamic stability constraint, formalized in Section 3.4.

The common element among these strategies is the feasible eCMP set, discussed in Section 3.5, which results from a pure ankle strategy and is referred to as the *feasible ankle eCMP set.* An overview of the proposed planning and control architecture is presented in Figure 13.

5.1. Ankle, Hip and Height-Variation Strategy

The ankle, hip, and height-variation strategies are scheduled through the eCMP, which is sent to the whole-body controller. We refer to this quantity as the *commanded eCMP*. The commanded force, computed from the commanded

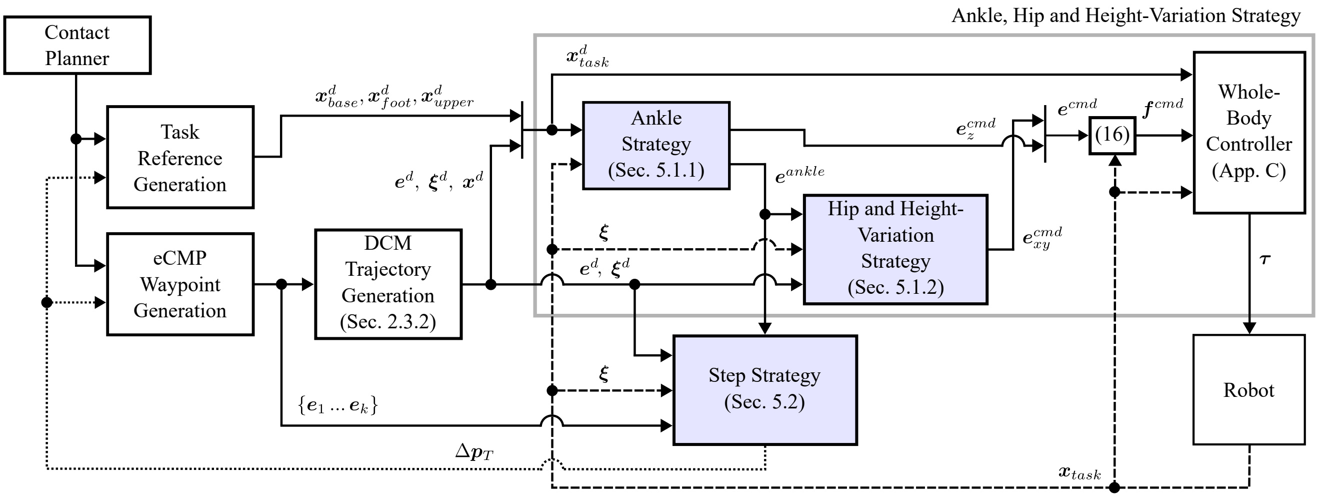

Figure 13. Overview of the proposed planning and control architecture, with the main contributions of this work highlighted in blue. The whole-body reference trajectory $\boldsymbol{x}^d_{task}$ consists of the references for the base orientation $\boldsymbol{x}^d_{base}$, the foot trajectories $\boldsymbol{x}^d_{foot}$, the upper-body motion $\boldsymbol{x}^d_{upper}$, and the CoM task. For brevity, not all system states are shown.

eCMP, is realized by the whole-body controller. We utilize a passivity-based whole-body controller that incorporates contact constraints and joint limit constraints. However, alternative whole-body controllers, such as those based on inverse dynamics, could also be employed. Note that we do not explicitly compute the required angular momentum or height variation to realize the commanded eCMP outside the feasible ankle eCMP set. Instead, the activation of the hip and height-variation strategy is realized by the direction and magnitude of the commanded horizontal eCMP, and the whole-body controller generates the required motion. In our whole-body controller, the horizontal linear CoM tracking task is assigned the highest priority in the task hierarchy, meaning it prioritizes realizing the commanded horizontal eCMP (or commanded horizontal CoM force) over other tasks. If the commanded eCMP lies within the feasible ankle eCMP set, the whole-body controller can generate it by simply adjusting the contact forces. However, if the commanded horizontal eCMP falls outside this set, the whole-body controller must adjust the feasible eCMP set by generating torque about the CoM or altering the CoM height. This may require relaxing lower-priority tasks such as the vertical CoM force task (i.e., tracking the commanded vertical eCMP) or the angular momentum task. More details about the whole-body controller can be found in Appendix C.

We propose an algorithm that positions the commanded eCMP to ensure dynamic stability while accounting for the feasible ankle set to avoid premature saturation of the system's kinematic and dynamic capacities through excessive angular momentum or CoM height variation. This proposed method replaces the original DCM controller (22) for computing the commanded eCMP.

5.1.1. Ankle Strategy. The ankle strategy is typically characterized by a zero vertical CoM acceleration and constant centroidal angular momentum. While this assumption is generally valid for balancing, we aim to extend this definition to general locomotion scenarios. Following a desired whole-body trajectory often results in a non-constant angular momentum, e.g., the motion of a swinging leg can generate a torque about the CoM. In addition, locomotion on uneven terrain may produce a non-zero vertical CoM acceleration. We extend the definition of the feasible ankle eCMP set, presented in Section 4.2, to the horizontal eCMP positions that are feasible given the commanded vertical eCMP e^{cmd}_z and the commanded torque about the CoM $\boldsymbol{\tau}^{cmd}_c$ which results from a tracking controller following the whole-body reference trajectory $\boldsymbol{x}^d_{task}$. In other words, the feasible eCMP set corresponding to the ankle strategy results from all realizable horizontal eCMP positions w.r.t. the contact constraints, in the nullspace of $\boldsymbol{e}^{cmd}_z$ and $\boldsymbol{\tau}^{cmd}_c$. In the proposed method, we compute $\boldsymbol{e}^{cmd}_z$ from the original DCM tracking controller (22), and $\boldsymbol{\tau}^{cmd}_c$ from a PD+ inspired tracking controller. Further details are provided in Appendix C, see (95)-(97). Consequently, the feasible ankle eCMP set is not necessarily the contact area but is shifted and scaled based on the commanded torque about the CoM and vertical eCMP, as shown in Figure 14. The black polygon illustrates the modulation of the ankle set for a non-constant angular momentum.

In the proposed push recovery algorithm, we do not need to compute the entire feasible ankle eCMP set; instead, we only need a single boundary point in the direction of the unconstrained eCMP

$$\boldsymbol{e}^u_{xy} = \boldsymbol{e}^{nom}_{xy} = \boldsymbol{e}^d_{xy} + (1 + bk_{\xi,nom})\Delta\boldsymbol{\xi}_{xy}. \tag{63}$$

Here, we introduce the nominal eCMP $\boldsymbol{e}^{nom}_{xy}$, which results from the original DCM tracking controller (22). The DCM control gains for the horizontal components are chosen to be identical, with $k_{\xi,nom} > 0$, ensuring that the nominal eCMP lies on a ray originating at the desired eCMP $\boldsymbol{e}^d_{xy}$ and extending in the direction of the DCM error $\Delta\boldsymbol{\xi}_{xy}$.

To ensure that the computed boundary point lies in the direction of the unconstrained eCMP, i.e., $\boldsymbol{a} = \Delta\boldsymbol{\xi}_{xy}/||\Delta\boldsymbol{\xi}_{xy}||_2$, we add an additional orthogonal task, weighted by $Q_4 > 0$, to the feasible eCMP set computation (Griffin et al. 2023). For this reason, we define the vector $\boldsymbol{d}$ that is orthogonal to $\boldsymbol{a}$ and opposed to the gravity vector, i.e., $\boldsymbol{d} = \boldsymbol{a} \times (0,\ 0,\ 1)^T$ and extend the QP

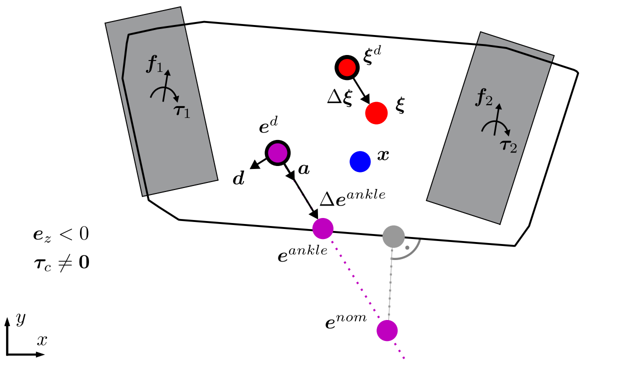

Figure 14. Illustration of the ankle eCMP computation, obtained by projecting the nominal eCMP onto the boundary of the feasible ankle eCMP set in the direction of the DCM error. For visualization purposes, the entire feasible ankle eCMP set is indicated as a black polygon. The gray point shows the QP solution when deactivating the orthogonal task Q_4.

from (61) as follows:

$$\min_{\boldsymbol{f}_i,\boldsymbol{\tau}_i} ||\boldsymbol{e}^{nom}_{xy} - \boldsymbol{e}^{ankle}||_{Q_1} + \left|\left|e^{cmd}_z - \boldsymbol{x}_z + \frac{b^2}{m}\sum_{i=1}^{p} \boldsymbol{f}_{i,z}\right|\right|_{Q_2} + \left|\left|\boldsymbol{\tau}^{cmd}_c - \sum_{i=1}^{p}(\boldsymbol{f}_i \times \boldsymbol{x}_{ic} + \boldsymbol{\tau}_i)\right|\right|_{Q_3} + ||\boldsymbol{d}_{xy}\cdot(\boldsymbol{e}^d_{xy} - \boldsymbol{e}^{ankle})||_{Q_4} + \sum_{i=1}^{p}(||\boldsymbol{f}_i||_{Q_r} + ||\boldsymbol{\tau}_i||_{Q_r}) \tag{64}$$

with

$$\boldsymbol{e}^{ankle} = \boldsymbol{x}_{xy} - \frac{b^2}{m}\sum_{i=1}^{p} \boldsymbol{f}_{i,xy} \tag{65}$$

and subject to the contact constraints (2)-(5). We refer to the resulting boundary point as the *ankle eCMP* $\boldsymbol{e}^{ankle}$. If the nominal eCMP lies within the feasible ankle set, the ankle eCMP coincides with the nominal eCMP $\boldsymbol{e}^{ankle} = \boldsymbol{e}^{nom}_{xy}$. Otherwise, it is projected onto the feasible ankle eCMP set in the direction of the DCM error within the nullspace of the commanded eCMP and torque about the CoM, realized through the task weighting $Q_2, Q_3 > Q_4 > Q_1 > Q_r$. It is important to note that, in the subsequent control implementation, we only use the resulting ankle eCMP (65) obtained from the ankle QP (64). The whole-body controller, which computes the final contact wrenches, is presented in Appendix C.

In the next step, we aim to evaluate whether the ankle eCMP can maintain dynamic stability. To achieve this, we introduce the deviation of the ankle from the desired eCMP

$$\Delta\boldsymbol{e}^{ankle} = \boldsymbol{e}^{ankle} - \boldsymbol{e}^d_{xy} \tag{66}$$

and evaluate the time derivative of the quadratic error function (48)

$$\dot{V}_{ankle} = \frac{1}{b}\left(\Delta\boldsymbol{\xi}_{xy}\cdot\Delta\boldsymbol{\xi}_{xy} - \Delta\boldsymbol{\xi}_{xy}\cdot\Delta\boldsymbol{e}^{ankle}\right). \tag{67}$$

If $\dot{V}_{ankle} < 0$, the ankle strategy is sufficient to ensure dynamic stability. Otherwise, additional reaction strategies are required to ensure that the DCM error is converging. Note that the entire push recovery algorithm, including solving the QP in (64), is executed once at each control cycle.

5.1.2. Hip and Height-Variation Strategy. The hip and height-variation strategies are designed to realize a minimum DCM error convergence rate to prevent the DCM error from diverging. To parameterize this minimum rate, we select a desired DCM control gain parameter smaller than the nominal value, $k_{\xi,nom} > k_{\xi,hhv} > 0$, to activate the hip and height-variation strategies. By inserting the DCM control law (20) into the time derivative of the quadratic error function (48), we derive the threshold value $\dot{V}_{hhv}$ as:

$$\dot{V}_{hhv} = -k_{\xi,hhv}\Delta\boldsymbol{\xi}_{xy}\cdot\Delta\boldsymbol{\xi}_{xy}. \tag{68}$$

If the ankle strategy alone cannot achieve the minimum DCM error convergence rate, i.e., if $\dot{V}_{ankle} > \dot{V}_{hhv}$, the hip and height-variation strategies are activated.

In this case, the commanded eCMP is shifted outside the feasible ankle set by the eCMP offset $\Delta\boldsymbol{e}^{hhv}$ to ensure the desired DCM error convergence rate:

$$\boldsymbol{e}^{cmd}_{xy} = \boldsymbol{e}^{ankle} + \Delta\boldsymbol{e}^{hhv}. \tag{69}$$

As discussed, a commanded eCMP outside the feasible ankle set requires the whole-body controller to generate angular momentum or change the height of the CoM in order to realize the corresponding horizontal CoM force.

Since the DCM control gains for the horizontal components are chosen to be identical, the commanded eCMP is shifted in the direction of the DCM error $\Delta\boldsymbol{\xi}$ until a convergence rate corresponding to $\dot{V}_{hhv}$ is reached:

$$\Delta\boldsymbol{e}^{hhv} = \lambda\Delta\boldsymbol{\xi}_{xy}. \tag{70}$$

Here, $\lambda \in \mathbb{R}$ is a scalar value that can be determined from the minimum convergence rate of the DCM error $\dot{V}_{hhv}$. By recalling (48) and inserting (66), (69), and (70), we obtain

$$\dot{V}_{hhv} = \frac{1}{b}(\Delta\boldsymbol{\xi}_{xy}\cdot\Delta\boldsymbol{\xi}_{xy} - \Delta\boldsymbol{\xi}_{xy}\cdot(\Delta\boldsymbol{e}^{ankle} + \lambda\Delta\boldsymbol{\xi}_{xy})). \tag{71}$$

Next, we compute the offset $\Delta\boldsymbol{e}^{hhv}$ by solving (71) for λ and inserting the definition of $\dot{V}_{hhv}$:

$$\Delta\boldsymbol{e}^{hhv} = \left(1 + bk_{\xi,hhv} - \frac{\Delta\boldsymbol{\xi}_{xy}\cdot\Delta\boldsymbol{e}^{ankle}}{\Delta\boldsymbol{\xi}_{xy}\cdot\Delta\boldsymbol{\xi}_{xy}}\right)\Delta\boldsymbol{\xi}_{xy}. \tag{72}$$

In the special case in which $\Delta\boldsymbol{e}^{ankle}$ is aligned with $\Delta\boldsymbol{\xi}_{xy}$, (69) and (72) reduce to

$$\boldsymbol{e}^{cmd}_{xy} = \boldsymbol{e}^d_{xy} + (1 + bk_{\xi,hhv})\Delta\boldsymbol{\xi}_{xy}. \tag{73}$$

Note that this alignment is not always guaranteed, since the weighted QP used to compute the ankle eCMP is not strictly hierarchical. Nevertheless, (72) ensures that $\boldsymbol{e}^{cmd}_{xy}$ corresponds to the orthogonal projection of $\boldsymbol{e}^{ankle}$ onto the plane associated with $\dot{V}_{hhv}$, thereby guaranteeing the minimum DCM error convergence rate.

In accordance with (68), we introduce the nominal DCM convergence rate $\dot{V}_{nom}$, based on the DCM control parameter $k_{\xi,nom}$ in (63). We then derive the final commanded eCMP law:

$$\boldsymbol{e}^{cmd}_{xy} = \begin{cases} \boldsymbol{e}^{nom}_{xy} & \text{if } \dot{V}_{nom} = \dot{V}_{ankle} \\ \boldsymbol{e}^{ankle} & \text{if } \dot{V}_{ankle} \leq \dot{V}_{hhv} \\ \boldsymbol{e}^{ankle} + \Delta\boldsymbol{e}^{hhv} & \text{otherwise} \end{cases}. \tag{74}$$

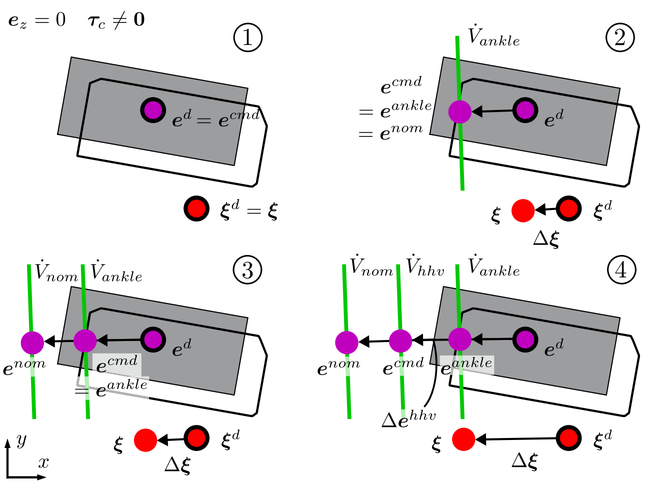

Figure 15. Illustration of the activation of a hip and height-variation strategy. The scenario shows the commanded eCMP placement based on (74), in response to a DCM error caused by a disturbance. The black polygon represents the boundary of the ankle eCMP set. The four cases (①-④) correspond to the vertical dashed lines in Figure 16.

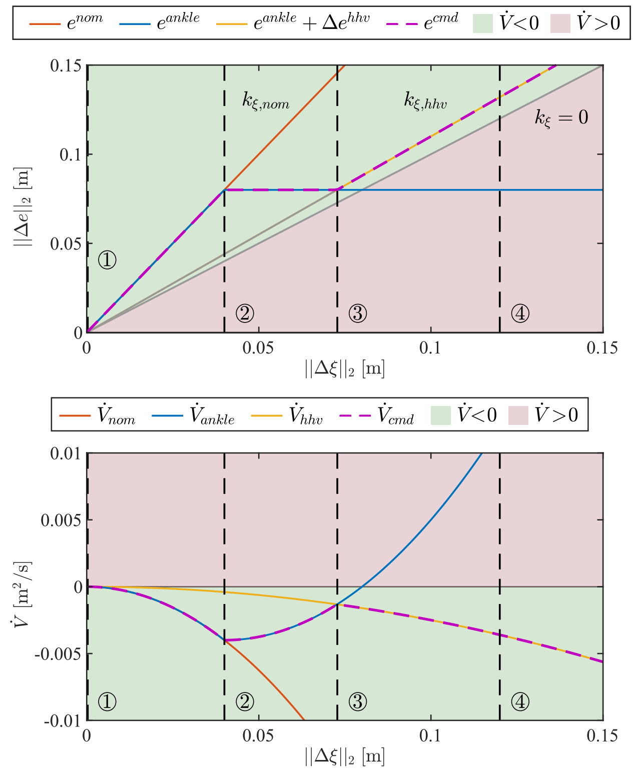

Figure 16. Top: The absolute deviation of the eCMP position from the desired eCMP as a function of the absolute DCM error. The slopes of the origin lines correspond to the DCM control gains. A DCM control parameter greater than zero results in an instantaneous error convergence (green area), whereas a parameter less than zero causes the DCM error to diverge (red area). The commanded eCMP law (74) is represented by the dashed purple line. The vertical dashed lines indicate the case distinctions (①-④) as shown in Figure 15.
Bottom: The time derivatives of the quadratic DCM error function corresponding to the eCMP positions of the top plot. The purple dashed line indicates the realized rates following the commanded eCMP behavior. It can be verified that the rate is always negative, ensuring that the DCM error is converging. Note that only the xy-components of all quantities are considered.

Figure 15 illustrates the activation of the various strategies. It can be verified that $\Delta \boldsymbol{e}^{hhv} = \boldsymbol{0}$ when $\dot{V}_{ankle} = \dot{V}_{hhv}$, ensuring that the resulting $\boldsymbol{e}^{cmd}_{xy}$ is continuous, as shown at position ③ in Figure 16. If the nominal eCMP is within the ankle set, it is directly commanded to the whole-body controller (between ① and ②). When the nominal eCMP is outside the ankle set, but the ankle eCMP can achieve a DCM convergence rate that is below the threshold value of $\dot{V}_{hhv}$, the ankle eCMP is commanded (between ② and ③). If this condition is not met, an offset is added to the ankle eCMP to ensure the minimum convergence rate (to the right of ③, with ④ shown as an example).

The computation of the commanded eCMP presented here only considers the horizontal components for the reasons mentioned above. The vertical component of the commanded eCMP results from the original DCM control law, i.e., $\boldsymbol{e}^{cmd}_z = \boldsymbol{e}^{nom}_z$. Finally, the corresponding CoM force $\boldsymbol{f}^{cmd}$, which is commanded to the whole-body controller, is computed based on $\boldsymbol{e}^{cmd}$ and (16). A summary of the computation steps for the ankle, hip, and height-variation strategy is provided in Algorithm 1.

As outlined by Englsberger et al. (2015), the eCMP corresponding to the nominal $k_{\xi,nom}$ can be directly commanded to the whole-body controller. However, doing so would immediately activate the hip and height-variation strategies as soon as the ankle strategy fails to achieve the nominal convergence rate, even if a slower convergence rate would suffice. Given the time-sensitive nature of the hip and height-variation strategies, this could lead to premature saturation of the system's kinematics and dynamics, adversely affecting the modulation of the eCMP set. In contrast, our proposed commanded eCMP law in (74) allows $k_{\xi,hhv}$ to be set independently. This decouples the activation of the hip and height-variation strategy from the original DCM controller.

As a design choice, the proposed controller places the commanded eCMP in the direction of the nominal eCMP based on the original DCM control law (63). Consequently, the recovering eCMP set is constrained to a ray originating at $\boldsymbol{e}^{ankle}$ parallel to the DCM error, represented as a purple dashed line in Figure 8. All eCMPs on a given plane corresponding to one value of $\dot{V}$ provide the same instantaneous convergence rate; however, not all drive the DCM directly back to the feasible ankle set (considering balancing). By constraining the commanded eCMP to lie on a ray in the direction of the DCM error, we ensure that the DCM returns to the feasible ankle set, as the desired DCM position is typically planned to be feasible. While this may not be the shortest path back to the feasible ankle set, nor the path that minimizes the use of angular momentum or height variation, it offers a conservative solution that guarantees the DCM will return to its desired position on a direct path.

5.2. *Step Strategy*

In our proposed control framework, the step strategy aims to compensate for the DCM error that the ankle strategy cannot correct until the end of the step. The goal is to adjust the next touchdown position to correct the DCM error until the subsequent step is taken. The step strategy integrates with the

Algorithm 1 Push Recovery Algorithm for the Ankle, Hip and Height-Variation Strategy

// *Compute commanded vertical eCMP and torque about the CoM from tracking controller*
  $\boldsymbol{e}_z^{cmd} \leftarrow$ (22), $\boldsymbol{\tau}_c^{cmd} \leftarrow$ (95)-(97)
// *Solve ankle QP s.t. contact constraints (2)-(5)*
  $\boldsymbol{e}^{ankle} \leftarrow$ (64), (65)
// *Compute eCMP offset (hip and height-variation strategy)*
  $\Delta\boldsymbol{e}^{hhv} \leftarrow$ (72)
// *Compute commanded horizontal eCMP*
  $\boldsymbol{e}_{xy}^{cmd} \leftarrow$ (74)
// *Concatenate commanded eCMP components*
  $\boldsymbol{e}^{cmd} \leftarrow (\boldsymbol{e}_{xy}^{cmd,T},\ \boldsymbol{e}_z^{cmd})^T$
// *Compute commanded CoM force for the whole-body controller*
  $\boldsymbol{f}^{cmd} \leftarrow$ (16)

other strategies by adjusting the DCM reference trajectory, thereby influencing the recovering eCMP set, see Figure 11. In this section, we present a step strategy based on our previous work (Mesesan et al. 2021). However, this method could be replaced in the presented push recovery pipeline with alternative DCM reference adaption algorithms, such as those proposed by Jeong et al. (2019) and Egle et al. (2023). Unlike these approaches, our method leverages information about the feasible eCMP set by taking into account the position of the ankle eCMP. In the following, only the horizontal components (xy-direction) of all quantities are considered. For simplicity, explicit labeling of the variables is omitted.

5.2.1. Step Strategy during Walking. The step strategy uses the deviation of the ankle eCMP from the desired eCMP $\Delta\boldsymbol{e}^{ankle}$ from (66) and the DCM error $\Delta\boldsymbol{\xi}$ as inputs. It then adjusts the next touchdown location, which corresponds to the subsequent eCMP waypoint. We reformulate (19) for the horizontal components in error space to establish a relationship between the DCM error and eCMP adjustments

$$\Delta\boldsymbol{\xi}^T = \boldsymbol{C}_\xi\left[\Delta\boldsymbol{e}_1,\ \Delta\boldsymbol{e}_2,\ \Delta\boldsymbol{e}_3,\ \ldots,\ \Delta\boldsymbol{e}_k,\ \Delta\boldsymbol{\xi}_k\right]^T. \quad (75)$$

Note that we only provide the derivations for single support; however, this approach also applies to double support phases. For further details, please refer to Mesesan et al. (2021). We associate the current eCMP waypoint $\boldsymbol{e}_1$ with the ankle strategy. The subsequent eCMP waypoint $\boldsymbol{e}_2$ corresponds to the next touchdown location and is therefore associated with the step strategy.

The goal at the eCMP replanning level is to compensate for as much of the DCM error as possible by shifting the current eCMP waypoint $\boldsymbol{e}_1$ (ankle strategy). If this adjustment is insufficient, the subsequent eCMP waypoint $\boldsymbol{e}_2$ will be adjusted to account for the remaining error (step strategy). Consequently, all eCMP waypoints, except for $\boldsymbol{e}_1$ and $\boldsymbol{e}_2$, as well as the final DCM, should remain unchanged ($\Delta\boldsymbol{e}_3 = ... = \Delta\boldsymbol{e}_k = \Delta\boldsymbol{\xi}_k = \boldsymbol{0}$).

We compute the displacement of the first waypoint $\Delta\boldsymbol{e}_1$ needed to fully compensate for the DCM error by the end of the current step, assuming no further perturbations occur. By reformulating (75) and setting all eCMP waypoint shifts,

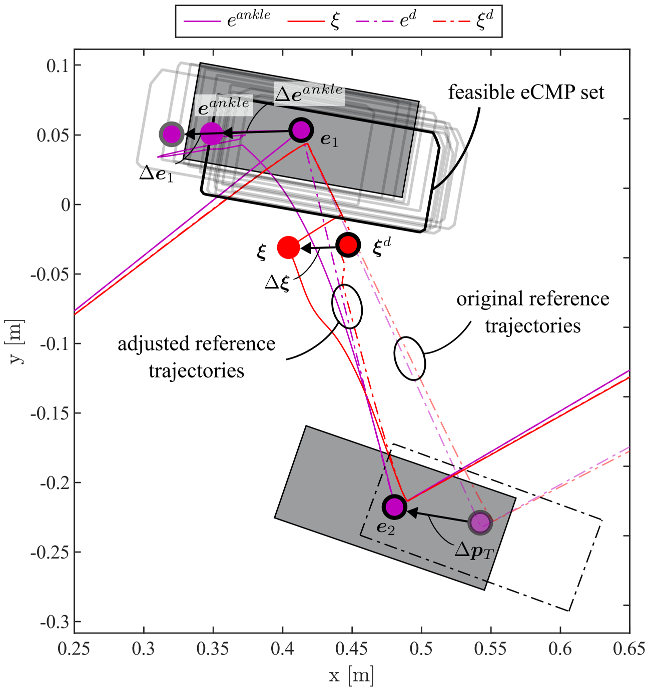

Figure 17. Illustration of the step strategy during walking: The robot is pushed during the single support phase. The hip and height-variation strategies are not active. The light black polygons display the changing feasible eCMP set over time due to the non-constant angular momentum, while the dark black polygon indicates the feasible eCMP set for an exemplary state. The corresponding DCM positions for this state are marked by red dots, while the eCMP quantities are shown by purple dots. The required eCMP displacement of the first waypoint $\Delta\boldsymbol{e}_1$ exceeds the ankle eCMP $\Delta\boldsymbol{e}^{ankle}$. Therefore, the next eCMP waypoint $\Delta\boldsymbol{e}_2$ is adjusted to compensate for the remaining DCM error. The corresponding DCM and eCMP reference trajectories are then updated based on the new eCMP waypoint $\boldsymbol{e}_2$.

except the first one, to zero, we obtain the following relation:

$$\Delta\boldsymbol{e}_1 = \frac{1}{\boldsymbol{C}_{\xi,1}}\Delta\boldsymbol{\xi}. \quad (76)$$

Here, $\boldsymbol{C}_{\xi,1}$ relates to the first scalar entry of the vector $\boldsymbol{C}_\xi$ in (75). Note that $0 < \boldsymbol{C}_{\xi,1} < 1$ can be shown (Mesesan et al. 2018, 2021). Since we compute the DCM reference trajectory backward in time, we can determine a finite-time solution for the required offset to drive the DCM error to zero. The amount of $\Delta\boldsymbol{e}_1$ that can be achieved by an actual ankle strategy has already been computed as $\Delta\boldsymbol{e}^{ankle}$ (66), which represents the boundary point on the feasible eCMP set.

Note that while the step strategy is always active, it is only applied when the required adjustment in (76) is larger than the eCMP waypoint shift based on the ankle strategy, i.e., $\Delta\boldsymbol{e}_1 > \Delta\boldsymbol{e}^{ankle}$. In this scenario, an additional eCMP waypoint adjustment of $\Delta\boldsymbol{e}_2$ is required to compensate for the DCM error. The step strategy is computed independently for the x- and y-directions.

We choose $\Delta\boldsymbol{e}_1 = \Delta\boldsymbol{e}^{ankle}$ and solve for the second waypoint in (75) and obtain for the step adjustment

$$\Delta\boldsymbol{e}_2 = \frac{1}{\boldsymbol{C}_{\xi,2}}(\Delta\boldsymbol{\xi} - \boldsymbol{C}_{\xi,1}\Delta\boldsymbol{e}^{ankle}). \quad (77)$$

The scalar $C_{\xi,2}$ is the second entry of the vector C_ξ, and it can again be verified that $0 < C_{\xi,2} < 1$, based on the convex properties discussed by Mesesan et al. (2018).

Finally, we introduce the next touchdown position of the swing leg $p_T \in \mathbb{R}^2$, which coincides with the corresponding horizontal planned footstep location. The vertical component of the footstep location is adjusted based on terrain information. Ideally, the step adjustment can be directly transferred to the touchdown position, i.e., $\Delta p_T = \Delta e_2$. However, to account for the system's kinematic limits, the maximum adjustment of the touchdown position is constrained based on simplified approximations of the maximum leg length, swing foot velocity, and self-collision avoidance:

$$\Delta p_T = \min(\Delta p_T^{max}, \max(\Delta p_T^{min}, \Delta e_2)). \tag{78}$$

Note that the DCM reference trajectory ξ^d and the reference trajectory of the swing leg are recomputed at each time step based on the new eCMP waypoint Δe_2 and touchdown position to ensure a continuous adjustment, see Figure 17. The step strategy affects the scheduling of the ankle, hip, and height-variation strategies shown in Figure 16 by shifting the desired DCM ξ^d in the direction of the actual DCM ξ. This corresponds to a leftward shift of the commanded eCMP along the purple dashed line, as the step strategy reduces the absolute DCM error $||\Delta\xi||_2$.

5.2.2. Step Strategy during Standing. The step strategy during walking assumes that future steps and the corresponding eCMP waypoints have already been planned. To activate the step strategy while standing, a step-in-place motion is initiated when the ankle strategy is considered saturated. This is the case when the time derivative of the quadratic error function $\dot{V}_{ankle}$ (67) corresponding to the ankle eCMP exceeds a certain threshold, i.e., $\dot{V}_{ankle} > \dot{V}_{step}$. The threshold $\dot{V}_{step}$ is derived according to $\dot{V}_{hhv}$ in (68), with the DCM control parameter $k_{\xi,step} > 0$. In balancing scenarios, a $k_{\xi,step}$ value close to zero will cause the ankle strategy to be considered saturated just before the DCM reaches the boundary of the contact area. By selecting $k_{\xi,step} > k_{\xi,hhv}$, the step strategy is triggered before the hip and height-variation strategies are active.

Note that the step strategy is not part of the whole-body reaction strategies of Section 5.1. The threshold $\dot{V}_{step}$ merely acts as a discrete trigger to initiate a step-in-place motion.

5.3. Order of Strategy Activation

During walking, the free tuning parameters are $k_{\xi,nom}$ and $k_{\xi,hhv}$. The first parameter is typically set to $k_{\xi,nom} = 1/b$, as this is the only value that ensures critical damping of the DCM error dynamics (Englsberger 2016). The hip and height-variation strategy parameter $k_{\xi,hhv}$ is chosen to be close to zero to ensure a minimum DCM convergence rate while avoiding excessive use of angular momentum or CoM height variation. Note that the step strategy, as well as the hip and height variation strategies, can be independently deactivated.

The ankle strategy is always active, shifting the commanded eCMP within the feasible eCMP set as a function of a DCM error. The step strategy continuously evaluates, from an eCMP waypoint perspective, whether the applied ankle eCMP adjustment can reduce the DCM error to zero by the end of the step. If the adjustment is insufficient, the step strategy shifts the next touchdown location until the DCM error is reduced to zero, or the touchdown shift saturates due to system limits. The DCM reference is directly updated according to the new eCMP waypoint. In addition, the hip and height-variation strategies continuously assess whether the ankle eCMP alone can achieve a minimum convergence rate; if not, these strategies become active. Reducing the DCM error to zero typically necessitates a larger adjustment of the commanded eCMP than merely attaining a minimum convergence rate. As a result, the step strategy saturates before the hip and height-variation strategies are activated.

6. Simulation and Experimental Results

The proposed algorithm is evaluated through simulation and extensive experiments with the humanoid robot TORO (Englsberger et al. 2014). TORO features 25 torque-controlled joints, six per limb and one connecting the torso to the waist. Additionally, it has two position-controlled servo motors in the neck. The robot has a height of 1.74 m, weighs 79.2 kg, and is equipped with an inertial measurement unit (IMU) located in the torso. TORO's rectangular feet measure 19.0 cm in length and 9.5 cm in width.

The whole-body controller, which is presented in Appendix C, operates at a control frequency of 1 kHz, while the low-level joint torque controller is executed at a rate of 3 kHz (Albu-Schäffer et al. 2007). The constrained QPs formulated in this work are solved by using the online active-set optimization algorithm qpOASES (Ferreau et al. 2008).

During the experiments, the robot is pushed directly by a human; therefore, we estimate the applied disturbances using a momentum-based observer, as described in De Luca et al. (2006) and Englsberger (2016). This observer integrates the sum of the known and estimated perturbation forces acting on the CoM and compares the result to the measured linear momentum. The estimated CoM perturbation force is then updated based on the difference between the measured and estimated linear momentum. Note that this estimation is used solely to analyze the applied disturbances and is not utilized in the proposed algorithms.

We select the nominal DCM controller gain to be $k_{\xi,nom} = 4\,\frac{1}{\mathrm{s}}$. In balancing scenarios, the minimum DCM controller gain, which activates the hip and height-variation strategies, is set to $k_{\xi,hhv} = 1\,\frac{1}{\mathrm{s}}$. For walking scenarios, the value is reduced to $k_{\xi,hhv} = 0.1\,\frac{1}{\mathrm{s}}$. Footage of the experiments conducted can be found in the supplementary video.

6.1. Simulation #1: Comparison of Different Strategy Combinations

To assess the effectiveness of the reaction strategies, we evaluate various combinations of the approaches discussed in simulation using OpenHRP (Kanehiro et al. 2004), examining their ability to recover from pushes of varying directions and magnitudes. We evaluate the following combinations of reaction strategies, as shown in Figure 18:

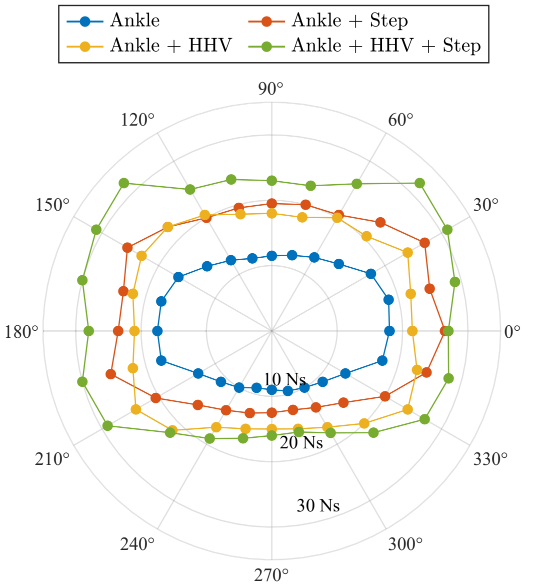

Figure 18. Simulation #1: Comparing the maximum recoverable pushes during walking in place for different strategy combinations.

1. *Ankle Strategy:* In this variant, the robot relies solely on the ankle strategy to resist external disturbances. The commanded eCMP is restricted to lie within the feasible ankle set. This is realized by setting Δe^{hhv} in (70) to zero, i.e., the whole-body controller generates the commanded horizontal CoM force solely by adjusting the contact forces at the feet.
2. *Ankle and Step Strategy:* This combination extends variant #1 by enabling the step strategy, as described in Section 5.2.
3. *Ankle, Hip and Height-Variation (HHV) Strategy:* In this variant, the control approach proposed in (74) is employed. If the ankle strategy alone is insufficient to maintain dynamic stability, the commanded eCMP is placed outside the feasible ankle set.
4. *Ankle, Hip and Height-Variation, and Step Strategy:* This variant combines all strategies and corresponds to the proposed method and order of strategy activation presented in this work.

We evaluate the maximum recoverable pushes during walking in place, with a single support time of $T_{SS} = 0.7$ s and a double support time of $T_{DS} = 0.2$ s. Each push lasts 0.1 s and is applied 0.25 s after the start of the swing phase, while the robot stands on its right leg. The push force is applied at the hip, and its direction is swept through 360° in increments of 15°. A push at 180° corresponds to a push from the front, in the negative x-direction.

It can be observed that variant #1, which employs only the ankle strategy, can compensate for the lowest impulse magnitude, with a mean recoverable impulse of 13.5 Ns. This is expected since the commanded eCMP can only be modulated within the feasible ankle set. Because the robot's foot is longer than it is wide, the resulting maximum recoverable impulse profile, shown in Figure 18, is increased along the 0°-180° direction. In variant #2, using both the ankle and step strategies uniformly increases the maximum recoverable pushes to a mean of 20.2 Ns. However, within the range of 225°-315°, the step strategy's performance is limited due to potential self-collisions between the swing and stance legs. Note that by the time the push is finished, 50% of the swing phase has already passed, leaving only about 0.35 s for the step strategy to adjust the next touchdown position. Variant #3 enhances disturbance rejection by generating angular momentum and adjusting the CoM height, thereby expanding the feasible eCMP set. The mean recoverable impulse is increased to 20.3 Ns.

Our proposed method, variant #4, combines the strengths of the individual strategies and substantially increases the maximum recoverable disturbances in all directions, resulting in an average recoverable impulse of 25.2 Ns. This corresponds to an increase of 86.7%, 24.8%, and 24.1% relative to variants #1-#3, respectively.

6.2. *Experiment #1: Balancing on Uneven Terrain*

In the first experiment, the robot balances on uneven terrain with non-coplanar foot orientation, while the step strategy is deactivated. Figure 19 shows snapshots of the robot's pose and its reaction to a frontal push with a maximum force of 102.7 N and an impulse of 33.4 Ns at $t = 0.58$ s.

The time evolution of the feasible eCMP set is shown in Figure 20. The displayed sets are computed based on the QP formulation in (64) using a rotating direction vector and incorporating all contact constraints. The black contour indicates the boundary of the modulated feasible eCMP, which is computed based on the CoM wrench that the whole-body controller actually realized. The gray contour represents the ankle eCMP set computed based on the commanded CoM wrench in (64). Note the sets are computed for visualization purposes only; the push recovery algorithm requires only the ankle eCMP in the direction of the commanded eCMP w.r.t. the desired eCMP.

The ankle set (gray contour) illustrates the feasible eCMP set that could be achieved if the robot solely relies on the ankle strategy to counteract a push. However, the modulated set (black contour) represents the feasible eCMP set realized by employing additional reaction strategies. The green line indicates the boundary of the set of instantaneous DCM error convergence. Based on (48), it represents all eCMP positions for which the time derivative of the quadratic DCM error is zero, i.e., $\dot{V} = 0$. The green line is only plotted for $||\Delta\boldsymbol{\xi}||_2 > 0.01$ m. To ensure dynamic stability, the commanded eCMP needs to be placed in the half-plane that does not contain the desired eCMP position. Contact stability is guaranteed when the commanded eCMP is within the feasible eCMP set. Both contact and dynamic stability are ensured when the eCMP is located within the recovering eCMP set, represented by the purple area. The control law in (74) constrains the commanded eCMP on a ray (shown as a purple dashed line) originating at $\boldsymbol{e}^{ankle}$ in the direction of the DCM error.

The disturbance is pushing the DCM toward the boundary of the contact area. Once the DCM leaves the feasible ankle eCMP set (gray contour), the robot can only maintain an upright balance when the feasible eCMP set is modulated to place the eCMP so that the measured DCM is located between the commanded eCMP and the desired DCM

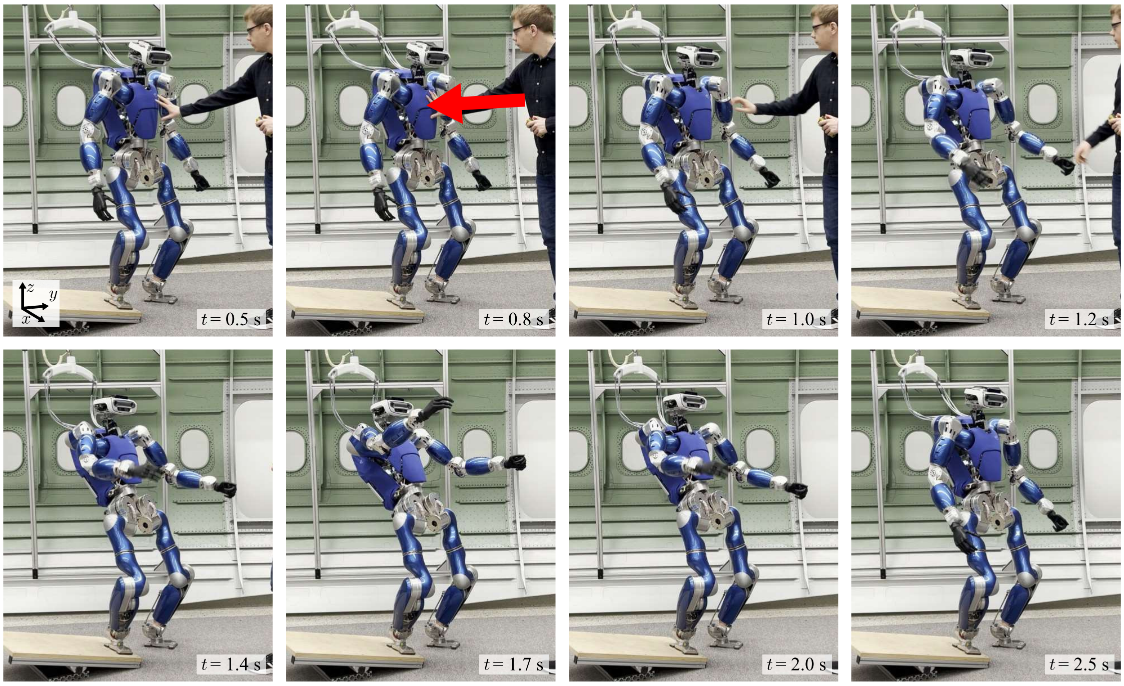

Figure 19. Snapshots of experiment #1: The robot is balancing on uneven terrain while being pushed from the front.

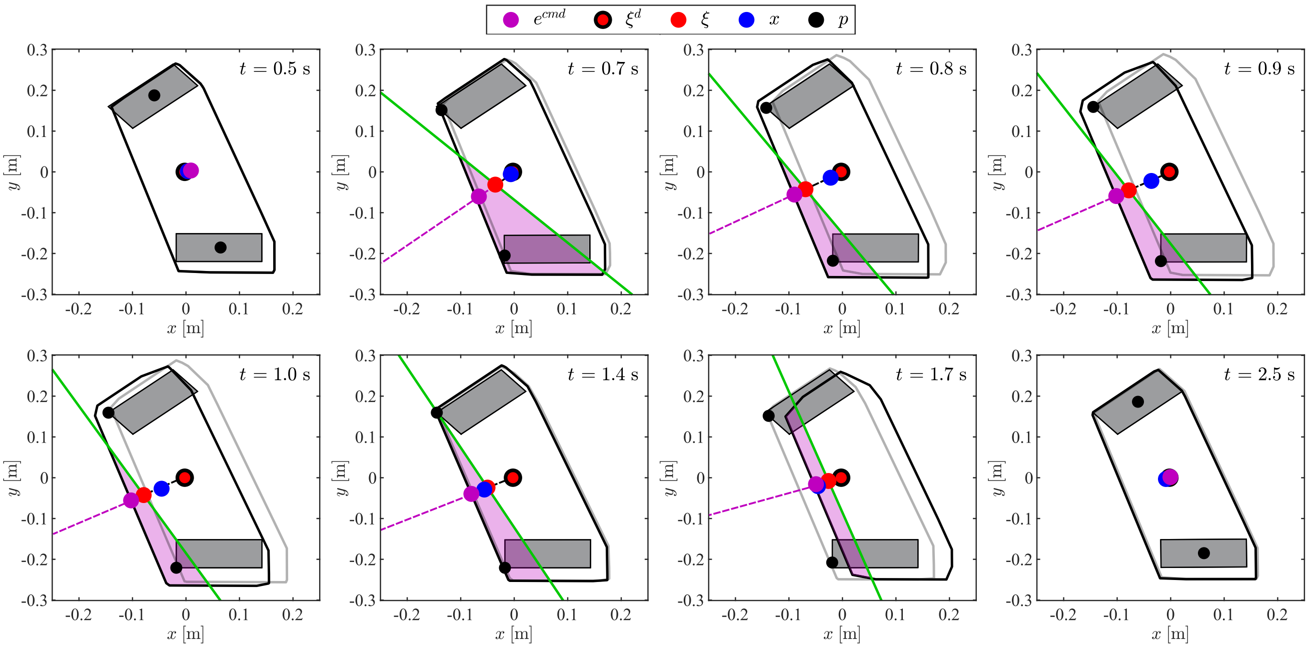

Figure 20. Results of experiment #1: A top-down view of the feasible eCMP sets for a balancing scenario on uneven terrain. The black dots represent the CoP positions of the respective foot. The purple dots indicate the commanded eCMP, while the blue dots correspond to the CoM position. The red dots illustrate the DCM positions. The black circled dots indicate the desired values of the respective quantities. The black contour represents the set boundary of the modulated feasible eCMP, while the gray contour displays the ankle eCMP set. The purple area indicates the recovering eCMP set. The commanded eCMP is placed outside the ankle set along the purple dashed line in response to an external push to ensure DCM error convergence. The whole-body controller generates angular momentum and a CoM height change to modulate the eCMP set accordingly. After compensating for the push, the angular momentum and height change must be reduced, causing the eCMP set to shift in the opposite direction.

(for example, at $t = 0.8$ s). For the balancing scenario in Figure 20, the desired eCMP, DCM, and CoM positions coincide for a stable rest position. The point quantities are plotted over time in Figure 21. The corresponding values for the time derivative of the quadratic DCM error function are provided in Figure 22.

The first snapshot at $t = 0.5$ s in Figure 20 shows the robot in a resting configuration. At this moment, the ankle set is not modulated, meaning the black and gray contours coincide. The second snapshot at $t = 0.7$ s shows the DCM approaching the edge of the feasible ankle eCMP set. The nominal, ankle, and commanded eCMP coincide until the nominal eCMP reaches the boundary of the feasible ankle

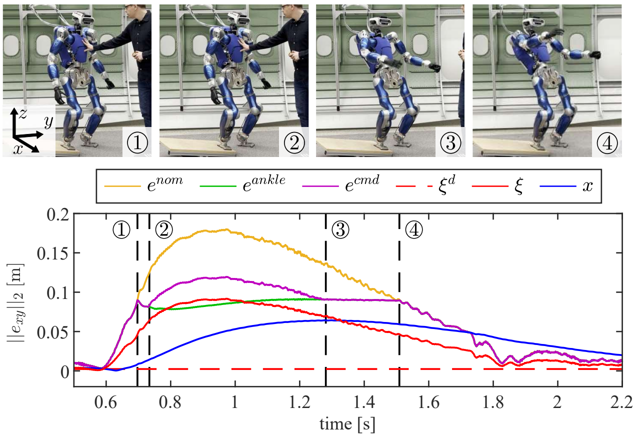

Figure 21. Results of experiment #1: The DCM quantities are plotted over time. The nominal eCMP resulting from the original DCM control law (22), the ankle eCMP resulting from the ankle set QP (64), and the commanded eCMP (74) resulting from the push recovery algorithm are presented. In addition, the desired and measured DCM position, as well as the measured CoM position, are shown. Note that the desired eCMP and CoM positions, which coincide with the DCM position for the horizontal coordinates, are not shown here.

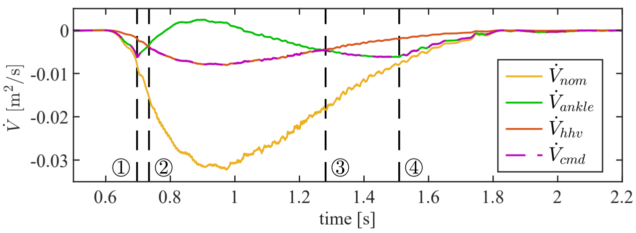

Figure 22. Results of experiment #1: Time derivative of quadratic DCM error function corresponding to the eCMP values in Figure 21. When $\dot{V}_{ankle} > \dot{V}_{hhv}$, a reaction strategy in addition to the ankle strategy needs to be activated to ensure DCM error convergence at a minimum rate of $\dot{V}_{hhv}$.

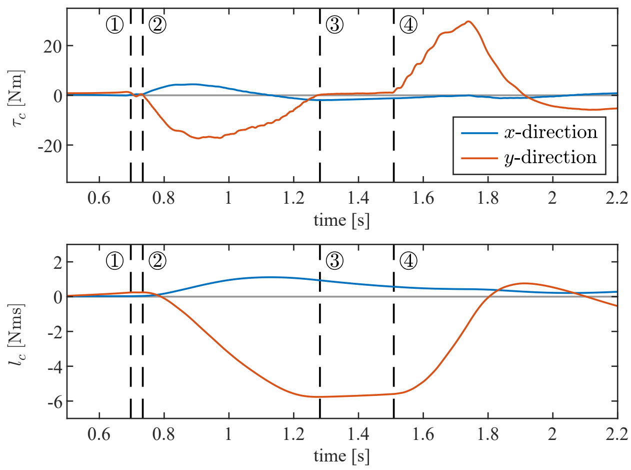

Figure 23. Results of experiment #1: Torque about the CoM and centroidal angular momentum in the x- and y-directions.

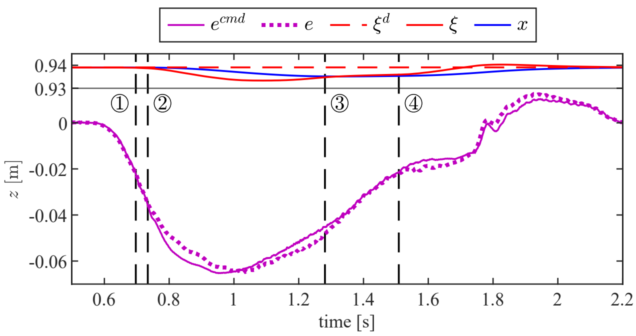

Figure 24. Results of experiment #1: Vertical components of the DCM quantities. The eCMP generated by the whole-body controller (purple dotted line) closely follows the commanded eCMP, as an extensive height-variation strategy is not required. The desired CoM position, which coincides with the desired DCM position, is omitted for clarity.

set, as shown at ① in Figure 21. Once the nominal eCMP is outside the feasible ankle set, the ankle and commanded eCMP coincide as long as the ankle eCMP is sufficient to realize the desired DCM convergence rate (from ① until ②). The commanded eCMP is placed at the border of the feasible ankle eCMP set in the direction of the DCM error as long as the time derivative of the quadratic DCM error corresponding to the ankle eCMP is smaller than a minimum value, i.e., $\dot{V}_{ankle} < \dot{V}_{hhv}$, see Figure 22.

Once the ankle eCMP cannot ensure the desired DCM error convergence rate, an offset based on (72) is added to the ankle eCMP (from ② until ③) and the commanded eCMP is placed outside the feasible ankle eCMP set. During this period, the whole-body controller induces angular momentum to modulate the eCMP set accordingly, in order to render the commanded eCMP feasible, see Figure 23. The corresponding snapshots ($t = 0.8$ s, $t = 0.9$ s, and $t = 1.0$ s) show that the modulated eCMP set no longer coincides with the ankle eCMP set.

Figure 24 shows that the height-variation strategy is not substantially engaged in this scenario, since the hip strategy alone was sufficient for push recovery. The realized vertical eCMP (purple dotted line), generated by the whole-body controller, closely follows the commanded vertical eCMP (purple line), which compensates for the vertical DCM error caused by the disturbance. The extent to which each strategy is employed depends on the individual task weights in the whole-body controller.

Figure 25 shows the CoM forces corresponding to the respective eCMPs. From ① to ③, the nominal horizontal CoM forces cannot be achieved; however, the whole-body controller accurately realizes the commanded horizontal CoM force. Since the height-variation strategy is not required, the realized vertical CoM force closely follows the nominal one.

It can be verified in Figure 22 that the commanded eCMP guarantees a strictly negative $\dot{V}_{cmd} < 0$, which ensures a convergence of the DCM error. Since $\dot{V}_{ankle} > 0$ for a period of time between ② and ③, an ankle strategy alone would not have been sufficient to counteract the disturbance. This corresponds to the period of time when the DCM error is outside the feasible ankle set, as shown in Figure 21.

After ③, Figure 21 shows that the ankle and commanded eCMP coincide again. At this stage, the ankle strategy is once more sufficient to ensure the desired DCM error convergence. However, as shown in Figure 23, the previously induced angular momentum is only reduced after ④. This

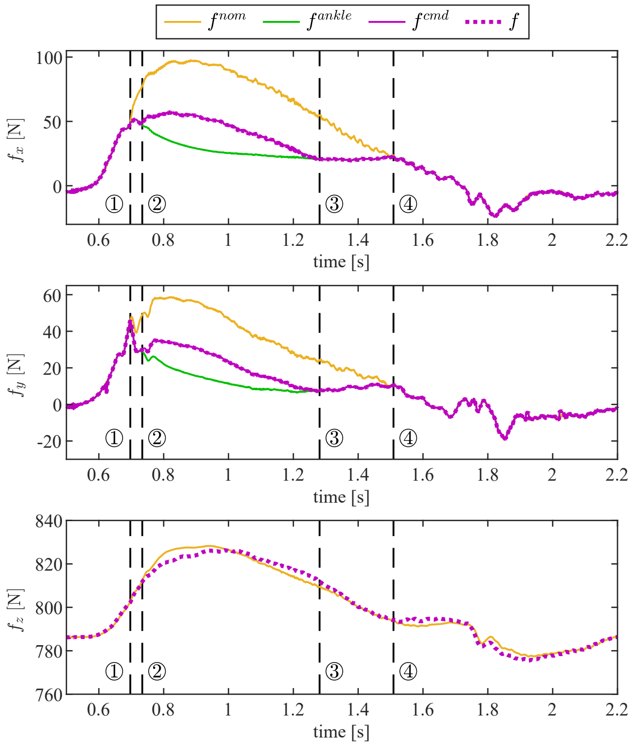

Figure 25. Results of experiment #1: CoM forces corresponding to the eCMP quantities shown in Figure 21. The purple dotted line represents the actual CoM force realized by the whole-body controller. Note that, for the vertical CoM force, $\boldsymbol{f}_z^{cmd} = \boldsymbol{f}_z^{nom}$ applies.

is because, within the whole-body controller, between ③ and ④, the horizontal CoM task leaves no nullspace for the posture task to reduce the previously generated angular momentum. Attempting to reduce the angular momentum would cause an opposite shift and scaling of the eCMP set, conflicting with the realization of the commanded horizontal eCMP.

Once the nominal eCMP and ankle eCMP coincide again (at ④), the push has been sufficiently recovered, allowing the posture task to become active. The accumulated angular momentum then begins to be reduced, causing an opposite shift and scaling of the eCMP set, as observed in Figure 20 at $t = 1.7$ s. As a result, during this period, the ankle eCMP computed in (64) may lie outside the modulated feasible eCMP set. However, since DCM error convergence has the highest priority, the push recovery strategy is scheduled independently of the influence of the posture recovery task. The final snapshot in Figure 19 at $t = 2.5$ s shows the robot in the fully recovered state.

6.3. Experiment #2: Balancing on Roller Board

In the second experiment, the robot balances on a roller board in a double support configuration while disturbances are applied to the roller board. This scenario demonstrates the reaction of the proposed push recovery approach when disturbances are not directly applied to the robot but are instead transmitted through a strong ground surface acceleration. Compared to experiment #1, the external force has a higher magnitude since the disturbance is more impulsive when overcoming the static friction of the roller board. The CoM experiences a disturbance of a maximum force of 221.5 N and an impulse of 29.5 Ns at $t = 1.12$ s, while the DCM error reaches an absolute deviation of 0.168 m at $t = 1.25$ s. The roller board is accelerated into a negative x-direction, corresponding to a push on the robot in a positive x-direction. This effect can be verified by comparing the reaction of the robot in Figure 26 to the results from experiment #1.

The friction coefficient between the roller board and the ground is experimentally determined to be $\mu = 0.09$. For comparison, the default friction coefficient in our parameter setting is $\mu = 0.4$. To ensure that the robot remains balanced without relative motion between the roller board and the ground, thereby avoiding further disturbances, we use this reduced friction coefficient within the contact constraints of the feet. Moreover, to prevent the CoP from reaching the tipping point of the roller board, the maximum and minimum CoP constraints in x-direction are reduced to $p_x^{max} = 0.05$ m and $p_x^{min} = -0.05$ m.

Figure 27 shows the feasible horizontal eCMP sets for the initial resting state at $t = 1.0$ s in the upper row and the disturbed state at $t = 1.25$ s in the lower row. To visualize the influence of the respective contact constraints, the first column shows the CoP constraint, the second column provides the translational Coulomb friction constraint, and the rotational Coulomb friction constraint is provided in the third column. The feasible eCMP set resulting from the combination of all contact constraints is plotted in the last column. The individual sets are computed based on (64), with only the respective contact constraint active. Corresponding to Figure 20, the dark-colored contours indicate the boundary of the modulated eCMP set, while the light-colored contours represent ankle sets.

To be physically feasible, the commanded eCMP must be within the set defined by every contact constraint, as shown in the lower row of Figure 27. It is noteworthy that the height-variation strategy is essential in this scenario due to the relatively low friction coefficient. The subplot corresponding to the translational friction constraint (second column, lower row) reveals that the DCM is outside the feasible ankle eCMP set. Without modulating the corresponding set, the commanded eCMP could not be placed in such a way that a return of the DCM to the feasible ankle set is guaranteed. As discussed in Section 4, the set related to the translational friction constraint can only be modulated by a height-variation strategy, i.e., by lowering the eCMP. While generating additional angular momentum extends the feasible sets corresponding to the CoP and rotational friction constraint, it cannot modulate the translational friction constraint. Consequently, the robot would not have recovered from this disturbance without employing the height-variation strategy.

The change of the vertical CoM height is shown in Figure 28. When the contact constraints are activated (indicated by ①), the eCMP set must be modulated to ensure that the commanded horizontal eCMP remains feasible. Consequently, the realized eCMP (purple dotted line), generated by the whole-body controller, deviates from the commanded eCMP (purple line) and is lowered to expand the feasible eCMP set, thereby producing an upward acceleration of the CoM. A minimum value of -0.46 m is

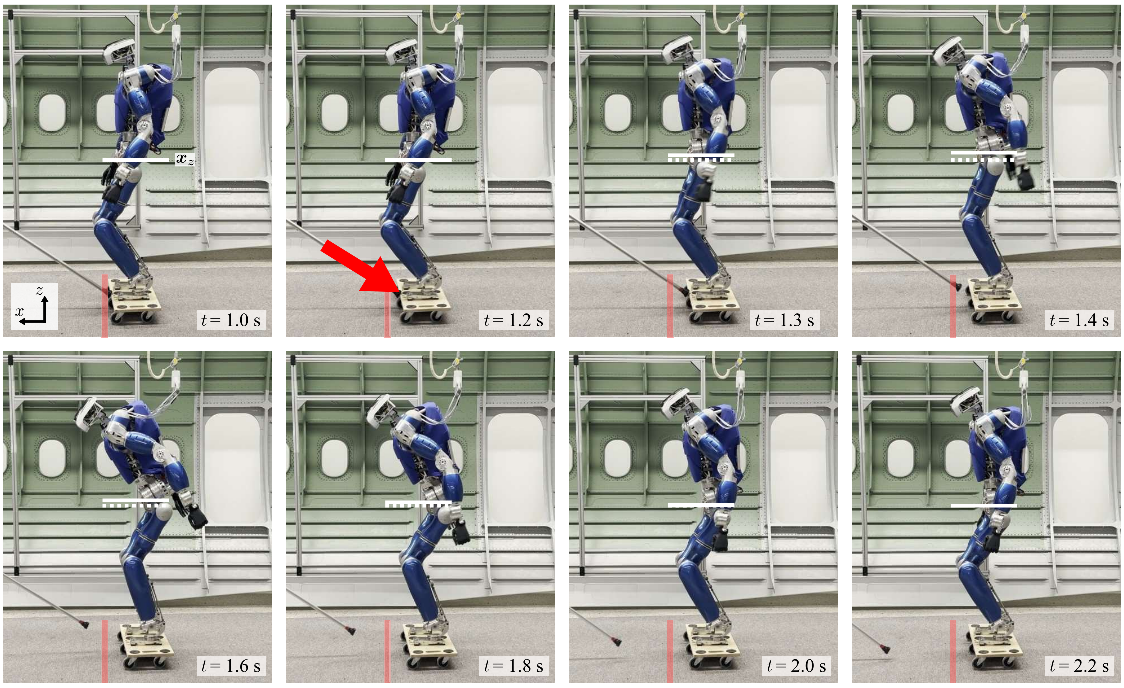

Figure 26. Snapshots of experiment #2: The robot balances on a roller board with a reduced friction coefficient. An impulsive disturbance is applied to the roller board. Due to the low friction coefficient, the height-variation strategy is particularly important. The white bar indicates the CoM height, while the red bar provides a visual reference for assessing the motion of the roller board.

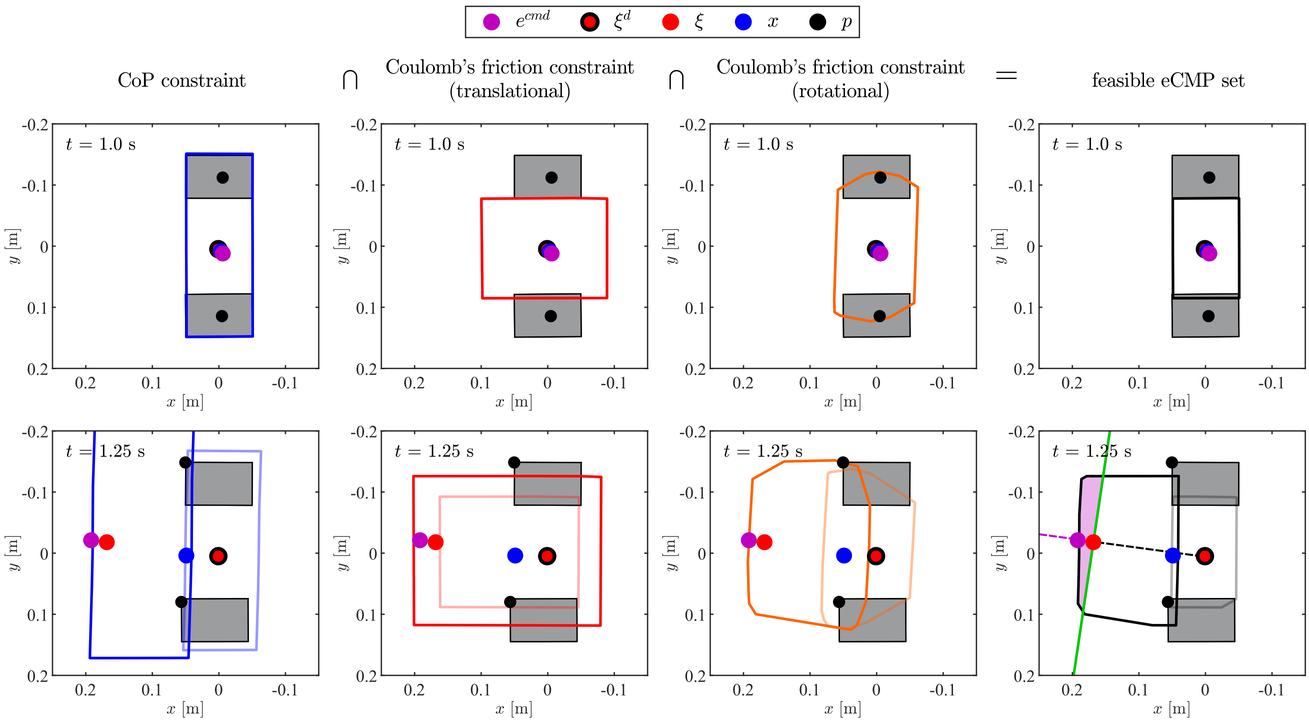

Figure 27. Results of experiment #2: Top-down view of the feasible eCMP sets for a balancing scenario on a roller board with reduced friction coefficient. Note that the x- and y-axes are reversed to align with the coordinate system in Figure 26. The dark contours of each color indicate the set boundary of the modulated feasible eCMP, while the lighter contours display the ankle eCMP set of each contact constraint. Each column shows the respective feasible eCMP set in both undisturbed and disturbed states.

reached at ②, corresponding to the peak of the DCM error. Once the push is mitigated, the CoM velocity decreases as the eCMP is raised above ground level (between ③ and ④). After ④, the CoM position converges back to its reference value. The corresponding CoM forces are presented in Figure 29.

The induced torque about the CoM and the corresponding centroidal angular momentum around the y-axis are shown in Figure 30. Starting from ①, the torque about the CoM is positive, shifting the feasible eCMP set corresponding to the CoP constraint in positive x-direction (see the first column, lower row in Figure 27). The maximum torque is

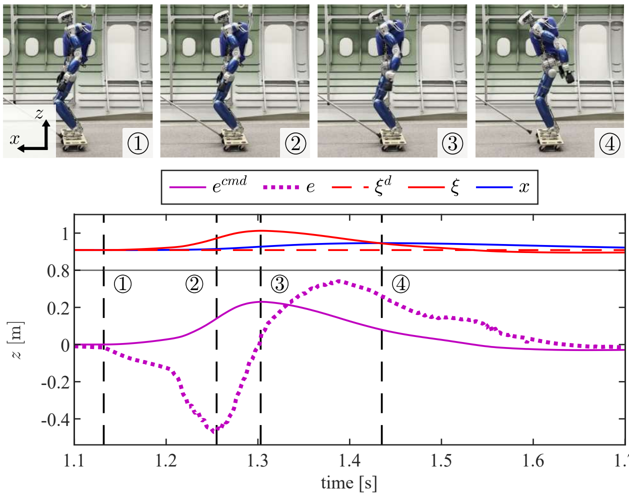

Figure 28. Results of experiment #2: Vertical components of DCM quantities. To extend the feasible eCMP set, the vertical eCMP generated by the whole-body controller (purple dotted line) deviates from the commanded one (purple line) and is lowered to below ground level to produce an upward CoM acceleration. Note that the desired CoM position, which coincides with the desired DCM position, is not shown here.

reached at ②, which corresponds to the maximum shift of the feasible eCMP set. To reduce the centroidal angular momentum to zero again, a negative torque is generated from ③ to ④, causing the feasible eCMP set to shift in negative x-direction again. Once the angular momentum is reduced, the robot returns to its reference posture, generating angular momentum of the opposite sign but with a smaller amplitude. This is shown in the last three snapshots of Figure 26.

Note that both the height-variation strategy and the hip strategy begin at time instant ① and reach their peak at ②, in order to modulate the feasible eCMP set in the required direction. However, the reduction in induced CoM height change and angular momentum depends on the individual task weight within the whole-body controller and occurs at varying speeds.

6.4. *Experiment #3: Walking*

The third scenario showcases the interaction between the ankle, hip, and height-variation strategy in combination with the step strategy. The robot is commanded to walk forward in positive x-direction with a step length of 0.15 m, corresponding to a stride length of 0.3 m. The single support time is $T_{SS} = 0.9$ s, and the double support time $T_{DS} = 0.3$ s. At $t = 5.23$ s, the robot is pushed with a maximum force of 100.0 N and an impulse of 32.3 Ns in negative x-direction.

Snapshots of the experiment are presented in Figure 31. A top-down visualization of the feasible eCMP sets is shown in Figure 32. It can be observed that the feasible ankle set is shifted during the single support phase. This behavior results from angular momentum generated by the whole-body motion, particularly the swing-leg and hip movements.

Figure 33 shows the DCM quantities plotted over time in the x-direction. The gray-shaded areas represent the double support phases. As a result of the push at ①, the DCM and CoM positions deviate from their references

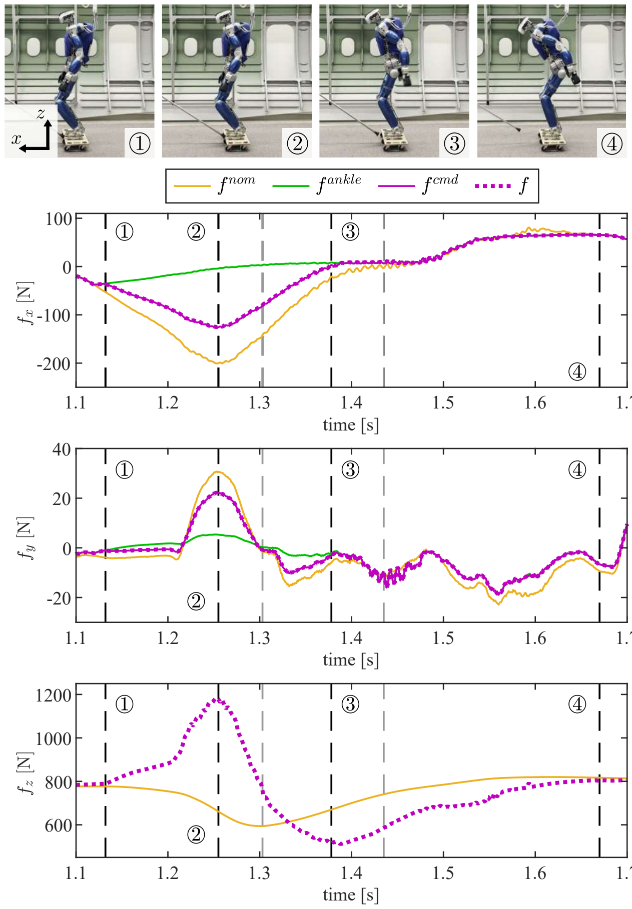

Figure 29. Results of experiment #2: CoM forces corresponding to the respective eCMP quantities. The purple dotted line represents the CoM force realized by the whole-body controller. The vertical CoM force relates to the vertical eCMP shown in Figure 28. Note that, for the vertical CoM force, $\boldsymbol{f}_z^{cmd} = \boldsymbol{f}_z^{nom}$ applies.

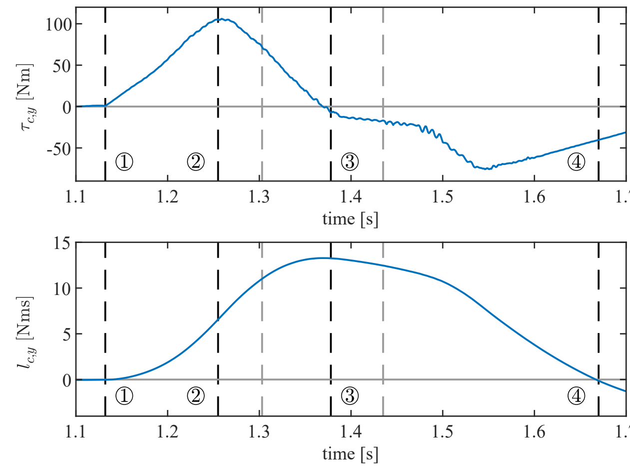

Figure 30. Results of experiment #2: Torque about the CoM and centroidal angular momentum around the y-axis. The gray dashed lines indicate the positions of ③ and ④ in Figure 28.

but subsequently return to them, due to the application of reaction strategies. Between ② and ③, the DCM reference is adjusted through the step strategy in the direction of the DCM error.

A segment of the timeline during which the disturbance occurs is presented in Figure 34. In this figure, all quantities

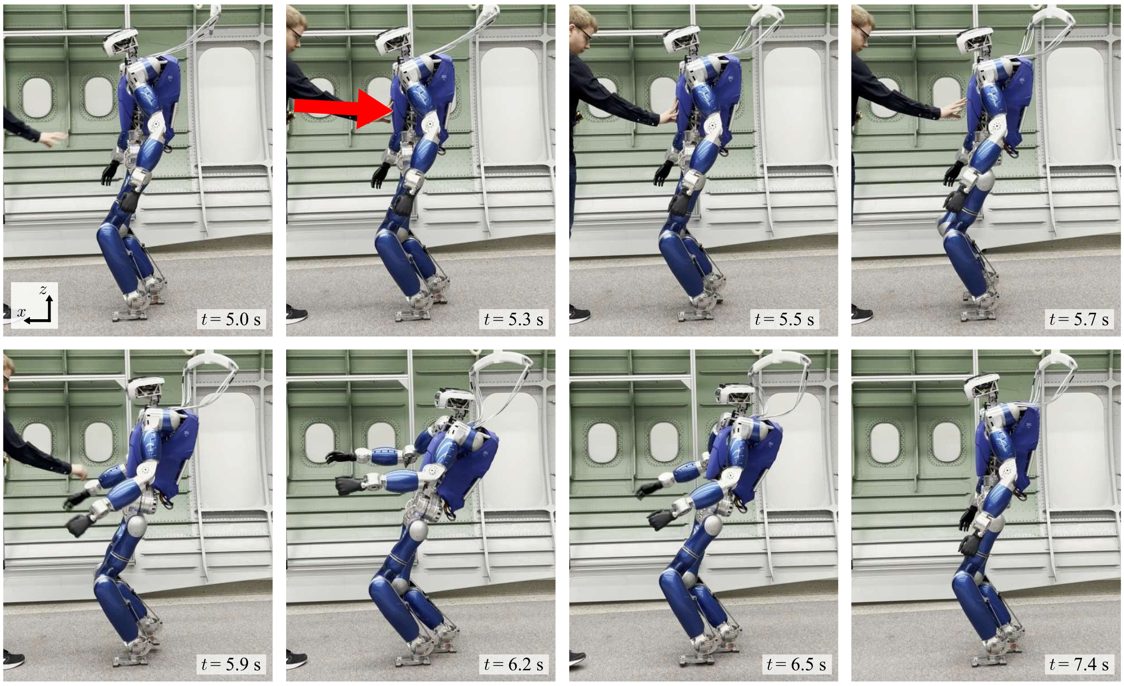

Figure 31. Snapshots of experiment #3: The robot is pushed from the front while walking.

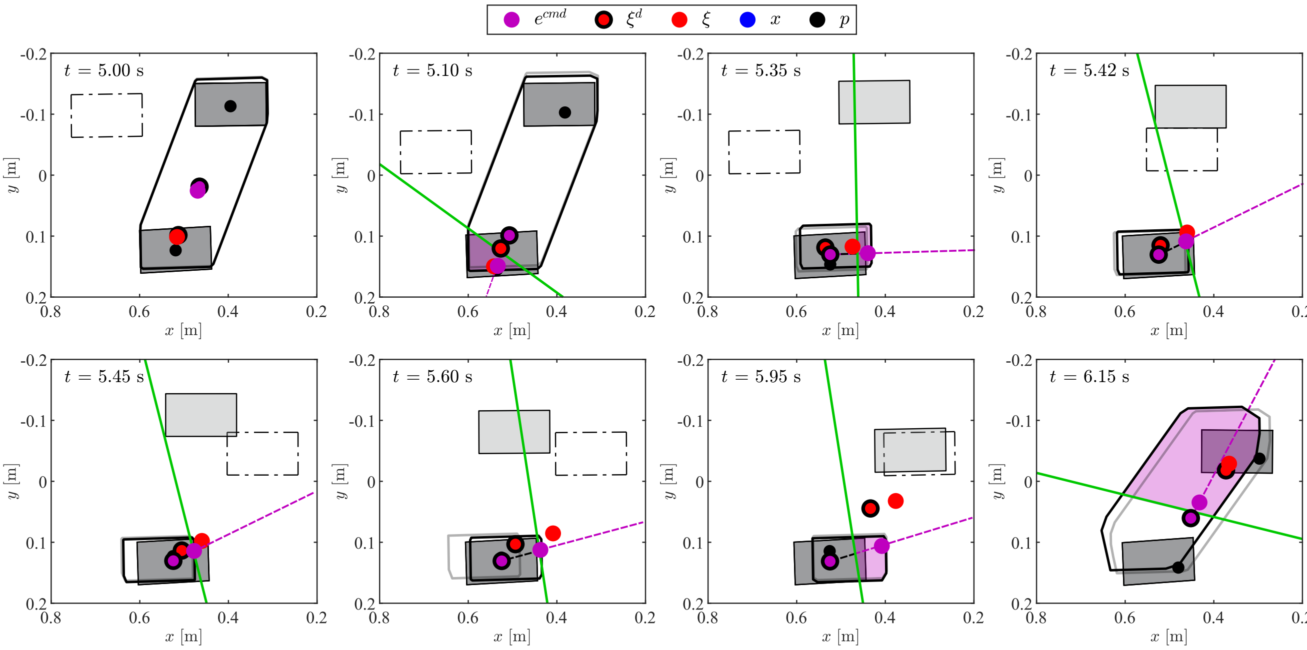

Figure 32. Results of experiment #3: Top-down view of the feasible eCMP sets for a walking scenario utilizing an ankle, hip, height-variation, and step strategy. Note that the x- and y-axes are reversed to align with the coordinate system in Figure 31. The black contour indicates the set boundary of the modulated feasible eCMP, while the gray contour displays the ankle eCMP set. The dark gray rectangles indicate the feet' positions in contact with the environment, the light gray areas represent the current position of the swing leg, and the dashed rectangles mark the planned touchdown position of the swing leg. All eCMP positions along the green line correspond to $\dot{V} = 0$. The purple area highlights the recovering eCMP set. The commanded eCMP is placed along the purple dashed line based on the strategy schedule. For clarity, the CoM position is omitted here.

are presented in error space. The push occurs during the swing phase of the right foot. To compensate for the disturbance, the step strategy is activated at first by adjusting the touchdown position of the swing leg. Figure 34 shows the required eCMP waypoint displacement $\Delta \boldsymbol{e}_1$ based on (76), which is necessary to fully correct the DCM error by the end of the current step. Additionally, the feasible ankle eCMP displacement $\Delta \boldsymbol{e}^{ankle}$ based on (66) is presented. The magnitudes of both quantities increase in response to the push at ①. Once $\Delta \boldsymbol{e}_1$ coincides with $\Delta \boldsymbol{e}^{ankle}$, the ankle strategy is saturated, which occurs at ②.

The DCM error that cannot be corrected by the ankle strategy alone is compensated for by adjusting the next eCMP waypoint, with the DCM reference trajectory being updated instantaneously. As long as the step strategy is not saturated, $\Delta \boldsymbol{e}_1$ moves along the $\Delta \boldsymbol{e}^{ankle}$ boundary, as it

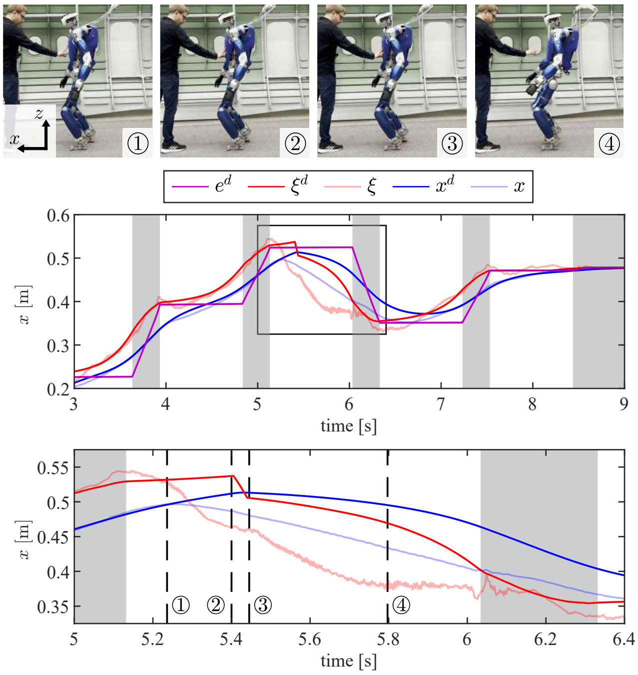

Figure 33. Results of experiment #3: DCM quantities plotted over time in x-direction. The gray-highlighted areas indicate the double support phases. The lower plot shows a segment of the timeline, marked by the black rectangle in the upper plot. For clarity, the desired eCMP is omitted in the lower plot. After the push occurs at ①, the DCM and CoM values deviate from their references. Between ② and ③, the DCM reference is adjusted using the step strategy to minimize the DCM error.

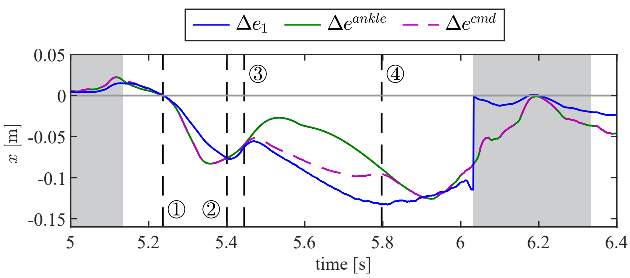

Figure 34. Results of experiment #3: Step strategy quantities presented in error space. At ②, the ankle strategy is considered saturated, as the required eCMP waypoint adjustment $\Delta \boldsymbol{e}_1$ coincides with the feasible ankle eCMP displacement $\Delta \boldsymbol{e}^{ankle}$. Between ② and ③, the step strategy is active and adjusts the next touchdown location. At ③, the step strategy is saturated due to kinematic and dynamic limits in the touchdown position adjustment. Between ③ and ④, the hip and height-variation strategies are active.

can be observed between ② and ③. However, once the maximum allowable adjustment to the touchdown position is reached, Δe_1 exceeds $\Delta \boldsymbol{e}^{ankle}$, as shown at ③. At this point, the step strategy is considered saturated as the robot has reached its kinematic limits and can no longer adjust the reference trajectory to compensate for the DCM error.

Figure 35 illustrates that the planned touchdown position of the right foot is changed from $\boldsymbol{p}_T = 0.69$ m at ② to $\boldsymbol{p}_T = 0.34$ m at ③. The swing leg trajectory of the right foot $\boldsymbol{r}$ is planned to reach $\boldsymbol{p}_T$ at the moment of touchdown and is recomputed based on the updated touchdown position.

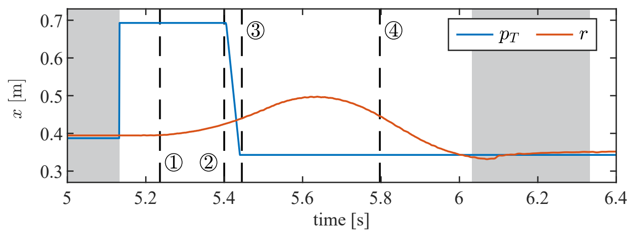

Figure 35. Results of experiment #3: Planned touchdown position and foot trajectory of the right foot in x-direction. The swing leg trajectory is planned to reach the desired touchdown position at the end of the swing phase. The desired touchdown position is updated according to the step strategy.

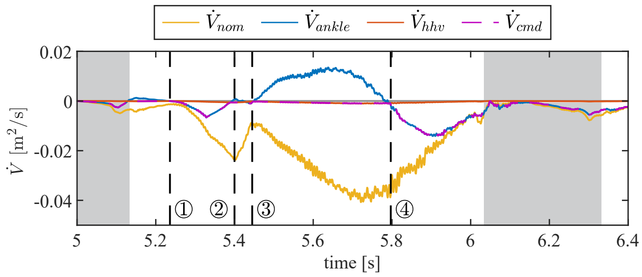

Figure 36. Results of experiment #3: Time derivative of quadratic DCM error function based on the updated DCM trajectory. When $\dot{V}_{ankle} > \dot{V}_{hhv}$, the hip and height-variation strategies are activated to ensure the convergence of the DCM error. This occurs between ③ and ④.

Based on Figure 36, we observe the effect of the adjusted DCM reference trajectory between ② and ③, where a reduced DCM error leads to a reduction in the magnitude of $\dot{V}_{nom}$. However, the step strategy alone is insufficient, as the ankle convergence rate becomes positive ($\dot{V}_{ankle} > 0$), indicating the DCM error diverges between ③ and ④, despite the adaptation of the DCM trajectory based on the new touchdown position.

To ensure DCM error convergence, the commanded eCMP is shifted outside the feasible eCMP ankle set by $\Delta \boldsymbol{e}^{hhv}$, as described in (72), through the generation of angular momentum and altering the height of the CoM. This is further illustrated in Figure 34 between ③ and ④, where $\Delta \boldsymbol{e}^{ankle}$ no longer coincides with $\Delta \boldsymbol{e}^{cmd}$. Also, the snapshot at $t = 5.60$ s in Figure 32 shows a deviation between the modulated and ankle eCMP sets. After ④, the ankle strategy is again sufficient to drive the DCM error to zero. This recovery was only achieved through the combined use of all reaction strategies.

6.5. *Experiment #4: Multi-contact Balancing*

The fourth scenario involves a multi-contact configuration in which the robot balances in double support while grasping a metal rod with its right hand. In this scenario, the step strategy is deactivated. This application is inspired by a typical bus scenario in which the bus suddenly accelerates or decelerates, causing standing passengers to try to maintain their balance by holding onto the vertical bars provided for that purpose. Figure 37 shows snapshots of the experiment. The contact of the right hand is modeled as a point contact with a contact normal pointing away from the robot, with an upper force limit (push) of 35 N and a lower limit (pull)

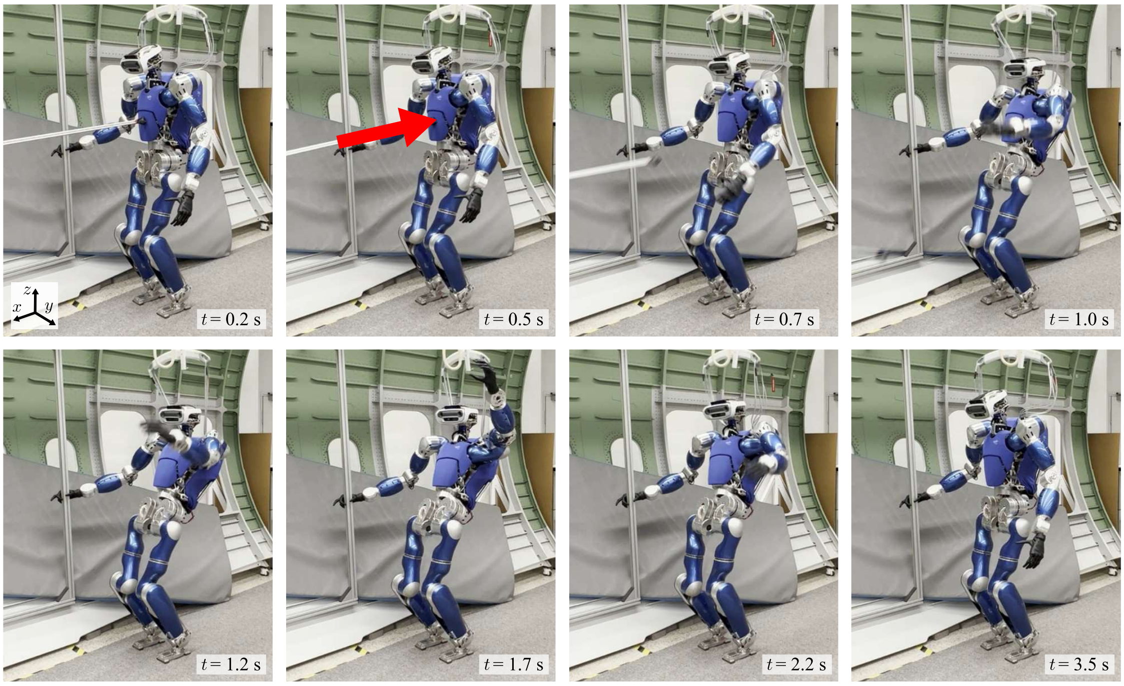

Figure 37. Snapshots of experiment #4: The robot is balancing in double support with an additional hand contact while being pushed from the front.

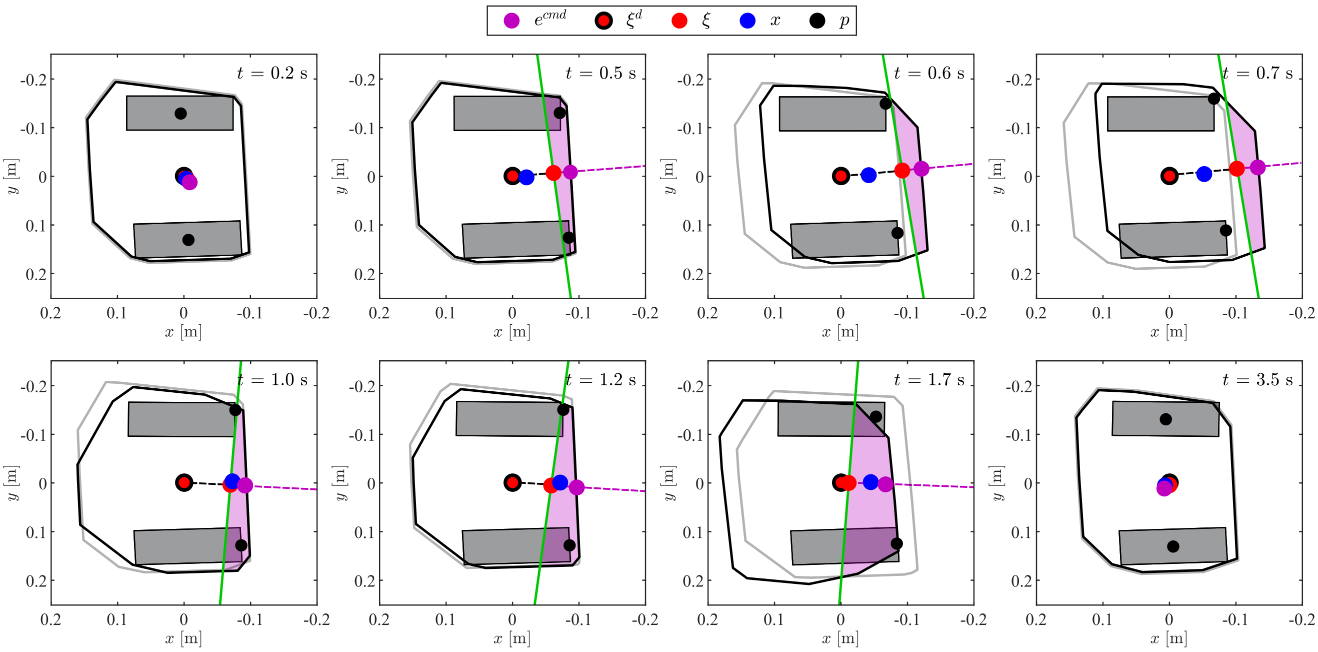

Figure 38. Results of experiment #4: Top-down view of the feasible eCMP sets for a multi-contact balancing scenario, including double support and additional hand contact. Note that the x- and y-axes are reversed to align with the coordinate system in Figure 37. The black contours indicate the set boundary of the modulated feasible eCMP, while the gray contours display the ankle eCMP set. The recovering eCMP set is illustrated by the purple area. The hand contact is modeled as a point contact with a force closure grasp with a maximum push force of 35 N and a minimum pull force of -5 N. The hand contact is located at the coordinates (0.3, -0.6, 1.1) m. Due to the additional contact, the feasible eCMP set is larger than the convex hull of the feet. The extension in the positive x-direction is larger due to a higher pushing force compared to the pulling one.

of -5 N. These constraints result from hardware limitations in the arm and hand of the robot. The additional end effector is added to the ankle QP in (64). The proposed whole-body control strategies (ankle, hip, and height-variation) can be used with an arbitrary number of end effectors in contact with the environment. Due to the additional hand contact at (0.3, -0.6, 1.1) m, the feasible eCMP set substantially exceeds the convex hull of the feet, as can be observed in the top-down visualization in Figure 38. The push is applied at $t = 0.3$ s in negative x-direction with a maximum force of 82.6 N and an impulse of 34.7 Ns.

Since the CoP constraint is the limiting factor in this scenario, the robot generates angular momentum using its free left arm and waist to modulate the feasible eCMP, ensuring convergence of the DCM error. This is illustrated in the snapshots at $t = 0.6$ s and $t = 0.7$ s. After the DCM returned to the feasible ankle set, the torque about the CoM is reduced to zero, as shown in the snapshots at $t = 1.0$ s and $t = 1.2$ s. However, the generated angular momentum must then be reduced to bring the robot to a halt. This requires applying torque about the CoM in the opposite sign to the previous one, causing the feasible eCMP set to shift in the opposite direction, as seen at $t = 1.7$ s. Subsequently, the posture task of the whole-body controller ensures that the robot returns to its reference pose, as shown in the snapshots at $t = 2.2$ s and $t = 3.5$ s.

7. Discussion

To discuss the advantages and limitations of the proposed method, we need to differentiate between the two main contributions of this work: the geometric analysis and computation of the feasible eCMP sets in Section 3, including their modulation based on reaction strategies in Section 4, and the push recovery algorithm for scheduling these reaction strategies in Section 5.

7.1. Geometric Analysis of eCMP Sets

7.1.1. 3D-DCM Framework. We selected the 3D-DCM framework for our analysis because it transforms forces, accelerations, and velocities into geometrically intuitive three-dimensional points in Cartesian space. By computing the feasible eCMP sets, we obtain the set of CoM forces that can be achieved in the current state of the robot without violating contact constraints, whereas the recovering eCMP set additionally guarantees dynamic stability. Derived directly from the centroidal CoM dynamics, the 3D-DCM dynamics are an intrinsic property of the multi-body dynamics and are valid for all robots.

7.1.2. Geometric Interpretation via Contact Wrench Parametrization. We derive the geometric interpretation of feasible eCMP sets from the contact wrench parametrization. This approach ensures that the formulated contact constraints naturally correspond to the three types of unintended contact breaking of surface contacts: slipping (translational Coulomb friction constraint), tilting (CoP constraint), and rotational slipping (rotational Coulomb friction constraint). By using a base vector parametrization with contact forces at the vertices of the contact area, the contact constraints can be expressed equivalently in the wrench parametrization. However, only the translational Coulomb friction constraint is explicitly formulated for the contact forces, while the other constraints result only indirectly from this. As a result, there is no direct relationship between the formulated constraints and the three types of unintended contact breaking in surface contacts. Consequently, the individual eCMP sets cannot be computed simply by deactivating the other contact constraints. This leads to the problem of obtaining only the final feasible eCMP set, without any indication of which of the three constraint types is active.

Our approach offers the flexibility to visualize either all or a subset of the contact constraints. By analyzing feasible eCMP sets corresponding to various contact constraints, we gain valuable insights into which reaction strategy is advantageous in different scenarios. For example, in situations with constant angular momentum, the rotational friction constraint becomes redundant. Conversely, in scenarios with a low friction coefficient, height variation is more likely to be required, as discussed in Section 6.3. We elaborated that the hip strategy shifts the sets corresponding to the CoP constraint and shifts and scales the set related to the rotational friction constraint, while the set for the translational friction constraint remains unaffected. The height-variation strategy results in a scaling of the corresponding sets. In combination with the recovering eCMP set derived from the instantaneous DCM error convergence constraint, we can evaluate potential eCMP position w.r.t. contact and dynamic stability.

7.1.3. Contact Model Limitations. One limitation of the proposed method is that the validity of the feasible eCMP sets depends on the accuracy of the underlying contact model, particularly on the precise identification of the friction coefficient. We use an experimentally determined friction coefficient, which typically yields a conservative estimate. Moreover, in this work, the rotational friction constraint is specifically formulated for rectangular contact areas; extending it to arbitrary contact shapes is left for future work.

7.1.4. DCM Time Constant. In Section 4, we analyze the modulation of feasible eCMP sets for humanoid push recovery under a constant DCM time factor b. This assumption is justified because the 3D-DCM exhibits decoupled, identical dynamics along all three axes, allowing the eCMP to be positioned freely in space. Applying the geometric analysis and the associated modulation of feasible eCMP sets to a time-varying b, as discussed in Hopkins et al. (2014), is a promising direction for future work.

7.1.5. Computational Complexity. One limitation of the proposed numerical computation of the feasible eCMP set is its relatively higher computational burden compared to approaches developed for motion generation using the double description method (Caron et al. 2015a), including those proposed by Caron and Kheddar (2017) and Audren and Kheddar (2018). This increased complexity arises from approximating the feasible set by computing a set of points projected onto the boundary of the respective sets. However, our method is designed explicitly for push recovery applications. As described in Section 5.1.1, for real-time execution, we only require a single boundary point of the feasible set in the direction of the nominal eCMP. This results in a single QP execution per control cycle, making the method highly efficient. The computational burden for obtaining the feasible eCMP set can be reduced by constructing an inner approximation of the set as a convex hull, following the idea of Abdalla et al. (2023).

7.1.6. Applications Beyond Push Recovery. In addition to push recovery applications, the geometric analysis of feasible eCMP sets can be used for post hoc analysis to answer the question: “Why did the robot behave as it did?” By visualizing these sets, the method offers explainability for black-box algorithms, such as reinforcement learning agents, providing valuable insights into the design of their respective cost functions and the implicit mechanisms they utilize.

Furthermore, the feasible eCMP sets can be used for 3D-DCM-based multi-contact motion planning under contact and dynamic stability constraints. We intend to pursue this direction in our future work.

7.2. Push Recovery Algorithm

7.2.1. Reaction Strategy Characteristics and Activation Order. The hip and height-variation strategies are inherently time-limited, because any induced angular momentum and CoM acceleration must later be reduced; they should therefore be used judiciously. By contrast, the step strategy is not time-constrained, but it requires terrain that permits step position adjustments. The proposed algorithm integrates these complementary strategies within a unified scheduling framework based on the instantaneous DCM error convergence.

Due to the different characteristics of the strategies, a natural activation schedule emerges. Typically, the step strategy becomes active once the ankle strategy reaches saturation. Simultaneously, the hip and height-variation strategies assess whether the applied ankle and step strategies are sufficient to ensure a minimum DCM error convergence; if not, they are activated. The tuning parameter $k_{\xi,hhv}$ determines when the hip and height-variation strategies activate. A larger value causes these strategies to activate earlier, allowing them to contribute more significantly to reducing the DCM error, rather than merely preventing its divergence. In walking scenarios, the hip and height-variation strategies primarily function to prevent DCM error from diverging until the next step is taken. As a result, $k_{\xi,hhv}$ is set to zero; however, for experiments, a small value greater than zero is used to account for potential tracking errors of the system. In balancing scenarios without the option of taking a step, the hip and height-variation strategies are required to return the DCM to a state from which the ankle strategy can reduce the DCM error to zero. Therefore, a value of $k_{\xi,hhv}$ greater than zero is required.

7.2.2. Modular Integration of the Step Strategy. The step strategy can be added and activated modularly. In this work, we integrate an extension of the step strategy presented in Mesesan et al. (2021); however, other DCM-based step adjustment methods, such as those presented by Jeong et al. (2019) and Griffin et al. (2023), can be used instead. In the presented framework, step adjustment is implemented without step time adjustment but can be easily extended using methods such as the one proposed by Egle et al. (2023), without requiring any adjustments to the current pipeline. We plan to incorporate this functionality in future work.

Note that, unlike the step adjustment algorithms mentioned above, which treat the foot area as the feasible ankle set, our push recovery algorithm computes the actual feasible ankle set. We achieve this by solving the ankle QP (64) for the current robot state, thereby providing a more accurate basis for deciding which reaction strategy to activate and to what extent.

7.2.3. Instantaneous Decision Making. Methods that incorporate a preview of future states, such as those based on model predictive control (Choe et al. 2023; Kim et al. 2023), typically rely on reduced models or simplifications, often equating foot area with the feasible ankle set. In contrast, we opt for instantaneous decision making, which enables us to utilize whole-body dynamics information in the ankle QP and the scheduling of the reaction strategies.

8. Conclusion

In this work, we proposed a geometric analysis of contact constraints and dynamic stability within the 3D-DCM framework, encoding feasible external CoM forces as eCMP sets. We derived an analytical relationship describing how these sets are modulated by push recovery strategies, including ankle, hip, height-variation, and step strategies. The developed framework can be applied both for online push recovery and for post hoc analysis of robot motion, enhancing the understanding of reaction strategies.

Based on the feasible eCMP sets, we developed a push recovery scheduling algorithm for the aforementioned strategies. This method can be used for robots balancing in multi-contact scenarios or during the single and double support phases of walking. The proposed approach was validated through extensive experiments with the humanoid robot TORO, including scenarios involving balancing on uneven terrain, walking, and multi-contact configurations.

Declaration of conflicting interests

The author(s) declared no potential conflicts of interest with respect to the research, authorship, and/or publication of this article.

Supplemental material

Supplemental material for this article is available online.

Notes

1. Here, $\mathrm{cone}(\mathcal{S}-\boldsymbol{x})$ denotes the conical hull of the set $\mathcal{S}-\boldsymbol{x}$, i.e., $\mathrm{cone}(\mathcal{S}-\boldsymbol{x}) = \left\{ \sum_{j=1}^{k} \alpha_j(\boldsymbol{p}_j - \boldsymbol{x}) \mid \boldsymbol{p}_j \in \mathcal{S}, \alpha_j \geq 0, k \in \mathbb{N} \right\}$.
2. A set $\mathcal{C} \subseteq \mathbb{R}^3$ is called a cone if, for every $\boldsymbol{x} \in \mathcal{C}$ and $\alpha \geq 0$, the condition $\alpha\boldsymbol{x} \in \mathcal{C}$ holds.
3. We assume a sufficiently large friction coefficient $\tilde{\mu}$. If $\tilde{\mu}$ is too small, the intersection set may no longer form a cone with a quadrilateral base. To simplify visualization, we exclude this case. The required $\tilde{\mu}$ can be computed based on neighboring plane normals, which must not become parallel, e.g., $|\boldsymbol{n}_{upp} \cdot \boldsymbol{n}_{upm}| \neq ||\boldsymbol{n}_{upp}||_2||\boldsymbol{n}_{upm}||_2$.
4. Here, $\mathrm{conv}(\mathcal{S})$ describes the convex hull of the set $\mathcal{S}$, i.e., $\mathrm{conv}(\mathcal{S}) = \left\{ \sum_{j=1}^{k} \alpha_j \boldsymbol{p}_j \mid \boldsymbol{p}_j \in \mathcal{S}, \alpha_j \geq 0, \sum_{j=1}^{k} \alpha_j = 1, k \in \mathbb{N} \right\}$.

References

Abdalla A, Focchi M, Orsolino R and Semini C (2023) An efficient paradigm for feasibility guarantees in legged locomotion. *IEEE Transactions on Robotics* 39(5): 3499–3515.

Aftab Z, Robert T and Wieber PB (2012) Ankle, hip and stepping strategies for humanoid balance recovery with a single model predictive control scheme. In: *Proceedings of the 12th IEEE-RAS International Conference on Humanoid Robots*. pp. 159–164.

Albu-Schäffer A, Haddadin S, Ott C, Stemmer A, Wimböck T and Hirzinger G (2007) The DLR lightweight robot: design and control concepts for robots in human environments. *Industrial Robot* 34(5): 376–385.

Atkeson CG and Stephens BJ (2007) Multiple balance strategies from one optimization criterion. In: *Proceedings of the 7th IEEE-RAS International Conference on Humanoid Robots*. pp. 57–64.

Audren H and Kheddar A (2018) 3-D robust stability polyhedron in multicontact. *IEEE Transactions on Robotics* 34(2): 388–403.

Caron S and Kheddar A (2017) Dynamic walking over rough terrains by nonlinear predictive control of the floating-base inverted pendulum. In: *Proceedings of the IEEE/RSJ International Conference on Intelligent Robots and Systems*. pp. 5017–5024.

Caron S, Pham QC and Nakamura Y (2015a) Leveraging cone double description for multi-contact stability of humanoids with applications to statics and dynamics. In: *Proceedings of Robotics: Science and Systems*.

Caron S, Pham QC and Nakamura Y (2015b) Stability of surface contacts for humanoid robots: Closed-form formulae of the contact wrench cone for rectangular support areas. In: *Proceedings of the IEEE International Conference on Robotics and Automation*. pp. 5107–5112.

Caron S, Pham QC and Nakamura Y (2017) ZMP support areas for multicontact mobility under frictional constraints. *IEEE Transactions on Robotics* 33(1): 67–80.

Cheng KB, Tanabe H, Chen WC and Chiu HT (2018) Role of heel lifting in standing balance recovery: A simulation study. *Journal of Biomechanics* 67: 69–77.

Choe J, Kim JH, Hong S, Lee J and Park HW (2023) Seamless reaction strategy for bipedal locomotion exploiting real-time nonlinear model predictive control. *IEEE Robotics and Automation Letters* 8(8): 5031–5038.

Dai H and Tedrake R (2016) Planning robust walking motion on uneven terrain via convex optimization. In: *Proceedings of the 16th IEEE-RAS International Conference on Humanoid Robots*. pp. 579–586.

De Luca A, Albu-Schäffer A, Haddadin S and Hirzinger G (2006) Collision detection and safe reaction with the DLR-III lightweight manipulator arm. In: *Proceedings of the IEEE/RSJ International Conference on Intelligent Robots and Systems*. pp. 1623–1630.

Del Prete A, Tonneau S and Mansard N (2018) Zero step capturability for legged robots in multicontact. *IEEE Transactions on Robotics* 34(4): 1021–1034.

Dietrich A and Ott C (2020) Hierarchical impedance-based tracking control of kinematically redundant robots. *IEEE Transactions on Robotics* 36(1): 204–221.

Egle T, Englsberger J and Ott C (2023) Step and timing adaptation during online DCM trajectory generation for robust humanoid walking with double support phases. In: *Proceedings of the 22nd IEEE-RAS International Conference on Humanoid Robots*. pp. 1–8.

Englsberger J (2016) *Combining reduced dynamics models and whole-body control for agile humanoid locomotion*. PhD Thesis, Technische Universitaet Muenchen, Germany.

Englsberger J, Ott C and Albu-Schäffer A (2015) Three-dimensional bipedal walking control based on divergent component of motion. *IEEE Transactions on Robotics* 31(2): 355–368.

Englsberger J, Werner A, Ott C, Henze B, Roa MA, Garofalo G, Burger R, Beyer A, Eiberger O, Schmid K and Albu-Schäffer A (2014) Overview of the torque-controlled humanoid robot TORO. In: *Proceedings of the 14th IEEE-RAS International Conference on Humanoid Robots*. pp. 916–923.

Ferreau HJ, Bock HG and Diehl M (2008) An online active set strategy to overcome the limitations of explicit MPC. *International Journal of Robust and Nonlinear Control* 18(8): 816–830.

Geyer H, Seyfarth A and Blickhan R (2006) Compliant leg behavior explains basic dynamics of walking and running. *Proceedings of the Royal Society B: Biological Sciences* 273: 2861–2867.

Griffin R, Foster J, Fasano S, Shrewsbury B and Bertrand S (2023) Reachability aware capture regions with time adjustment and cross-over for step recovery. In: *Proceedings of the 22nd IEEE-RAS International Conference on Humanoid Robots*. pp. 1–8.

Grizzle J, Abba G and Plestan F (2001) Asymptotically stable walking for biped robots: analysis via systems with impulse effects. *IEEE Transactions on Automatic Control* 46(1): 51–64.

Henze B (2020) *Whole-Body Control for Multi-Contact Balancing of Humanoid Robots*. PhD Thesis, Technische Universitaet Muenchen, Germany.

Henze B, Roa MA and Ott C (2016) Passivity-based whole-body balancing for torque-controlled humanoid robots in multi-contact scenarios. *The International Journal of Robotics Research* 35(12): 1522–1543.

Hinata R and Nenchev DN (2018) Balance stabilization with angular momentum damping derived from the reaction null-space. In: *Proceedings of the 18th IEEE-RAS International Conference on Humanoid Robots*. pp. 188–195.

Hirukawa H, Hattori S, Harada K, Kajita S, Kaneko K, Kanehiro F, Fujiwara K and Morisawa M (2006) A universal stability criterion of the foot contact of legged robots - adios ZMP. In: *Proceedings of the IEEE International Conference on Robotics and Automation*. pp. 1976–1983.

Hofmann A, Popovic M and Herr H (2009) Exploiting angular momentum to enhance bipedal center-of-mass control. In: *Proceedings of the IEEE International Conference on Robotics and Automation*. pp. 4423–4429.

Hopkins MA, Hong DW and Leonessa A (2014) Humanoid locomotion on uneven terrain using the time-varying divergent component of motion. In: *Proceedings of the 14th IEEE-RAS International Conference on Humanoid Robots*. pp. 266–272.

Horak F and Nashner L (1986) Central programming of postural movements: adaptation to altered support-surface configurations. *Journal of Neurophysiology* 55: 1369–1381.

Hyon S, Osu R and Otaka Y (2009) Integration of multi-level postural balancing on humanoid robots. In: *Proceedings of the IEEE International Conference on Robotics and Automation*. pp. 1549–1556.

Jeong H, Lee I, Oh J, Lee KK and Oh JH (2019) A robust walking controller based on online optimization of ankle, hip, and stepping strategies. *IEEE Transactions on Robotics* 35(6): 1367–1386.

Kajita S, Kanehiro F, Kaneko K, Fujiwara K, Harada K, Yokoi K and Hirukawa H (2003) Biped walking pattern generation by using preview control of zero-moment point. In: *Proceedings of the IEEE International Conference on Robotics and Automation*. pp. 1620–1626.

Kajita S, Kanehiro F, Kaneko K, Yokoi K and Hirukawa H (2001) The 3D linear inverted pendulum mode: a simple modeling for a biped walking pattern generation. In: *Proceedings of the IEEE/RSJ International Conference on Intelligent Robots and Systems*. pp. 239–246.

Kanehiro F, Hirukawa H and Kajita S (2004) OpenHRP: Open architecture humanoid robotics platform. *The International Journal of Robotics Research* 23(2): 155–165.

Khadiv M, Herzog A, Moosavian SAA and Righetti L (2020) Walking control based on step timing adaptation. *IEEE Transactions on Robotics* 36(3): 629–643.

Kim MJ, Lim D, Park G and Park J (2023) Foot stepping algorithm of humanoids with double support time adjustment based on capture point control. In: *Proceedings of the IEEE International Conference on Robotics and Automation*. pp. 12198–12204.

Koolen T, Bertrand S, Thomas G, de Boer T, Wu T, Smith J, Englsberger J and Pratt J (2016) Design of a momentum-based control framework and application to the humanoid robot Atlas. *International Journal of Humanoid Robotics* 13: 1650007:1–1650007:34.

Koolen T, de Boer T, Rebula J, Goswami A and Pratt J (2012) Capturability-based analysis and control of legged locomotion, part 1: Theory and application to three simple gait models. *The International Journal of Robotics Research* 31(9): 1094–1113.

Lee SH and Goswami A (2012) A momentum-based balance controller for humanoid robots on non-level and non-stationary ground. *Autonomous Robots* 33: 399–414.

Liu J, Chen H, Wensing PM and Zhang W (2021) Instantaneous capture input for balancing the variable height inverted pendulum. *IEEE Robotics and Automation Letters* 6(4): 7421–7428.

Maki BE and McIlroy WE (1997) The role of limb movements in maintaining upright stance: the "change-in-support" strategy. *Physical Therapy* 77: 488–507.

Mesesan G, Englsberger J, Garofalo G, Ott C and Albu-Schäffer A (2019) Dynamic walking on compliant and uneven terrain using DCM and passivity-based whole-body control. In: *Proceedings of the 19th IEEE-RAS International Conference on Humanoid Robots*. pp. 25–32.

Mesesan G, Englsberger J, Henze B and Ott C (2017) Dynamic multi-contact transitions for humanoid robots using divergent component of motion. In: *Proceedings of the IEEE International Conference on Robotics and Automation*. pp. 4108–4115.

Mesesan G, Englsberger J and Ott C (2021) Online DCM trajectory adaptation for push and stumble recovery during humanoid locomotion. In: *Proceedings of the IEEE International Conference on Robotics and Automation*. pp. 12780–12786.

Mesesan G, Englsberger J, Ott C and Albu-Schäffer A (2018) Convex properties of center-of-mass trajectories for locomotion based on divergent component of motion. *IEEE Robotics and Automation Letters* 3(4): 3449–3456.

Mesesan G, Schuller R, Englsberger J, Ott C and Albu-Schäffer A (2023) Unified motion planner for walking, running, and jumping using the three-dimensional divergent component of motion. *IEEE Transactions on Robotics* 39(6): 4443–4463.

Mesesan G, Schuller R, Englsberger J, Roa MA, Lee J, Ott C and Albu-Schäffer A (2025) Motion planning for humanoid locomotion: Applications to homelike environments. *IEEE Robotics and Automation Magazine* 32(1): 35–48.

Orin DE and Goswami A (2008) Centroidal momentum matrix of a humanoid robot: Structure and properties. In: *Proceedings of the IEEE/RSJ International Conference on Intelligent Robots and Systems*. pp. 653–659.

Orsolino R, Focchi M, Caron S, Raiola G, Barasuol V, Caldwell DG and Semini C (2020) Feasible region: An actuation-aware extension of the support region. *IEEE Transactions on Robotics* 36(4): 1239–1255.

Ott C, Roa MA and Hirzinger G (2011) Posture and balance control for biped robots based on contact force optimization. In: *Proceedings of the 11th IEEE-RAS International Conference on Humanoid Robots*. pp. 26–33.

Paden B and Panja R (1988) Globally asymptotically stable 'PD+' controller for robot manipulators. *International Journal of Control* 47(6): 1697–1712.

Pijnappels M, Kingma I, Wezenberg D, Reurink G and van Dieën JH (2010) Armed against falls: the contribution of arm movements to balance recovery after tripping. *Experimental Brain Research* 201: 689–699.

Popovic MB, Goswami A and Herr H (2005) Ground reference points in legged locomotion: Definitions, biological trajectories and control implications. *The International Journal of Robotics Research* 24(12): 1013–1032.

Pratt J, Carff J, Drakunov S and Goswami A (2006) Capture point: A step toward humanoid push recovery. In: *Proceedings of the 6th IEEE-RAS International Conference on Humanoid Robots*. pp. 200–207.

Pratt J, Koolen T, de Boer T, Rebula J, Cotton S, Carff J, Johnson M and Neuhaus P (2012) Capturability-based analysis and control of legged locomotion, part 2: Application to M2V2, a lower-body humanoid. *The International Journal of Robotics Research* 31(10): 1117–1133.

Righetti L, Buchli J, Mistry M, Kalakrishnan M and Schaal S (2013) Optimal distribution of contact forces with inverse-dynamics control. *The International Journal of Robotics Research* 32(3): 280–298.

Runge CF, Shupert CL, Horak FB and Zajac FE (1999) Ankle and hip postural strategies defined by joint torques. *Gait Posture* 10(2): 161–170.

Sardain P and Bessonnet G (2004) Forces acting on a biped robot. center of pressure-zero moment point. *IEEE Transactions on Systems, Man, and Cybernetics - Part A: Systems and Humans* 34(5): 630–637.

Schuller R, Mesesan G, Englsberger J, Lee J and Albu-Schäffer A (2026) Centroidal angular momentum-aware planning for legged locomotion integrating 3D-DCM and swing-leg trajectory optimization. *IEEE Robotics and Automation Letters* : 1–8.

Schuller R, Mesesan G, Englsberger J, Lee J and Ott C (2021) Online centroidal angular momentum reference generation and motion optimization for humanoid push recovery. *IEEE Robotics and Automation Letters* 6(3): 5689–5696.

Schuller R, Mesesan G, Englsberger J, Lee J and Ott C (2022) Online learning of centroidal angular momentum towards enhancing DCM-based locomotion. In: *Proceedings of the IEEE International Conference on Robotics and Automation*. pp. 10442–10448.

Sentis L and Khatib O (2005) Synthesis of whole-body behaviors through hierarchical control of behavioral primitives.

International Journal of Humanoid Robotics 2: 505–518.

Shafiee M, Romualdi G, Dafarra S, Chavez FJA and Pucci D (2019) Online DCM trajectory generation for push recovery of torque-controlled humanoid robots. In: *Proceedings of the 19th IEEE-RAS International Conference on Humanoid Robots*. pp. 671–678.

Sreenath K, Park HW, Poulakakis I and Grizzle JW (2011) A compliant hybrid zero dynamics controller for stable, efficient and fast bipedal walking on MABEL. *The International Journal of Robotics Research* 30(9): 1170–1193.

Takao S, Yokokohji Y and Yoshikawa T (2003) Fsw (feasible solution of wrench) for multi-legged robots. In: *Proceedings of the IEEE International Conference on Robotics and Automation*. pp. 3815–3820.

van Hofslot BJ, Griffin R, Bertrand S and Pratt J (2019) Balancing using vertical center-of-mass motion: A 2-D analysis from model to robot. *IEEE Robotics and Automation Letters* 4(4): 3247–3254.

Vukobratović M and Stepanenko J (1972) On the stability of anthropomorphic systems. *Mathematical Biosciences* 15(1): 1–37.

Zambella G, Schuller R, Mesesan G, Bicchi A, Ott C and Lee J (2023) Agile and dynamic standing-up control for humanoids using 3D divergent component of motion in multi-contact scenario. *IEEE Robotics and Automation Letters* 8(9): 5624–5631.

Appendix

A. Index to multimedia extensions

Table 1. Index to multimedia extensions.

Exten.	Media type	Description
#1	Video	Experiments with the humanoid robot TORO

B. Rotational Coulomb Friction Constraint

In this section, we present the derivation of the upper and lower limits on the perpendicular contact torque (5) as described by Caron et al. (2015b). All quantities are expressed w.r.t. the contact frame, and we define the contact wrench $\boldsymbol{w} = (\boldsymbol{f}^T,\ \boldsymbol{\tau}^T)^T$ at the center of the rectangular contact surface. We also introduce four contact force vectors $\boldsymbol{f}_i^c \in \mathbb{R}^3$ with $i \in \{1,2,3,4\}$, located at each of the corners. The corner forces are subject to the linearized friction pyramid:

$$\begin{aligned} |\boldsymbol{f}_{x,i}^c| &\leq \tilde{\mu}\boldsymbol{f}_{z,i}^c \\ |\boldsymbol{f}_{y,i}^c| &\leq \tilde{\mu}\boldsymbol{f}_{z,i}^c \end{aligned} \tag{79}$$

and the unilaterality constraint:

$$\boldsymbol{f}_{z,i}^c > 0. \tag{80}$$

When mapped to the center of the contact surface, the force vectors at the corners sum up to the contact wrench

$$\begin{pmatrix} \boldsymbol{f} \\ \boldsymbol{\tau} \end{pmatrix} = \sum_{i=1}^{4} \begin{pmatrix} \boldsymbol{f}_i^c \\ -\boldsymbol{x}_{c,i} \times \boldsymbol{f}_i^c \end{pmatrix}, \tag{81}$$

where $\boldsymbol{x}_{c,i} = (\pm p_x^{max},\ \pm p_y^{max},\ 0)^T$ is the vector from the i-th corner to the center of the rectangular foot. Based on the eight inequality constraints resulting from (79) and the corner force mapping (81), eight inequality constraints for the contact wrench can be obtained to prevent rotational slippage

$$\begin{aligned} (-\tilde{\mu},-\tilde{\mu},-1)\,\boldsymbol{\tau} &\geq \left(p_y^{max}, p_x^{max}, -\tilde{\mu}(p_x^{max}+p_y^{max})\right)\boldsymbol{f} \\ (-\tilde{\mu},\tilde{\mu},-1)\,\boldsymbol{\tau} &\geq \left(p_y^{max}, -p_x^{max}, -\tilde{\mu}(p_x^{max}+p_y^{max})\right)\boldsymbol{f} \\ (\tilde{\mu},-\tilde{\mu},-1)\,\boldsymbol{\tau} &\geq \left(-p_y^{max}, p_x^{max}, -\tilde{\mu}(p_x^{max}+p_y^{max})\right)\boldsymbol{f} \\ (\tilde{\mu},\tilde{\mu},-1)\,\boldsymbol{\tau} &\geq \left(-p_y^{max}, -p_x^{max}, -\tilde{\mu}(p_x^{max}+p_y^{max})\right)\boldsymbol{f} \\ (\tilde{\mu},\tilde{\mu},1)\,\boldsymbol{\tau} &\geq \left(p_y^{max}, p_x^{max}, -\tilde{\mu}(p_x^{max}+p_y^{max})\right)\boldsymbol{f} \\ (\tilde{\mu},-\tilde{\mu},1)\,\boldsymbol{\tau} &\geq \left(p_y^{max}, -p_x^{max}, -\tilde{\mu}(p_x^{max}+p_y^{max})\right)\boldsymbol{f} \\ (-\tilde{\mu},\tilde{\mu},1)\,\boldsymbol{\tau} &\geq \left(-p_y^{max}, p_x^{max}, -\tilde{\mu}(p_x^{max}+p_y^{max})\right)\boldsymbol{f} \\ (-\tilde{\mu},-\tilde{\mu},1)\,\boldsymbol{\tau} &\geq \left(-p_y^{max}, -p_x^{max}, -\tilde{\mu}(p_x^{max}+p_y^{max})\right)\boldsymbol{f}. \end{aligned} \tag{82}$$

By solving for $\boldsymbol{\tau}_z$, we obtain explicit upper and lower limits for the rotational friction constraint, which are expressed as eight separate inequality constraints. The first four constraints correspond to the upper limit, while the last four constraints relate to the lower limit. For further details, please refer to Caron et al. (2015b). These constraints can also be expressed as explicit upper and lower limits for the perpendicular contact torque

$$\begin{aligned} \boldsymbol{\tau}_z^{max} =& \tilde{\mu}(p_x^{max} + p_y^{max})\boldsymbol{f}_z \\ &- |p_y^{max}\boldsymbol{f}_x + \tilde{\mu}\boldsymbol{\tau}_x| - |p_x^{max}\boldsymbol{f}_y + \tilde{\mu}\boldsymbol{\tau}_y| \end{aligned} \tag{83}$$

and

$$\begin{aligned} \boldsymbol{\tau}_z^{min} =& -\tilde{\mu}(p_x^{max} + p_y^{max})\boldsymbol{f}_z \\ &+ |p_y^{max}\boldsymbol{f}_x - \tilde{\mu}\boldsymbol{\tau}_x| + |p_x^{max}\boldsymbol{f}_y - \tilde{\mu}\boldsymbol{\tau}_y|. \end{aligned} \tag{84}$$

C. Whole-body Controller

In this section, we present the passivity-based whole-body controller and its integration with the DCM framework. The controller optimizes contact wrenches and reference task accelerations embedded in a quadratic program and outputs desired joint torques to realize the intended motion. When the commanded horizontal eCMP cannot be realized solely by modulating the contact wrenches, the whole-body controller generates angular momentum or adjusts the robot's height to achieve the required forces at the CoM. The push recovery algorithm presented in Section 5 can also be combined with a different whole-body controller (Sentis and Khatib 2005; Righetti et al. 2013; Koolen et al. 2016) to track the commanded eCMP (74) or the commanded CoM force.

We employ a passivity-based whole-body controller due to its proven robustness and performance (Mesesan et al. 2019; Schuller et al. 2021), and extend its original formulation (Ott et al. 2011; Henze et al. 2016) to increase flexibility in task specification. In this work, we introduce a formulation that integrates the wrench distribution problem with kinematic-based optimization in task space. This approach enables the simultaneous formulation of potentially conflicting tasks and the optimization of whole-body motions using either a subset or the complete set of task-space degrees of freedom (DoF).

C.1. Whole-body Dynamics Modeling

In Section 2.1, we focused on the centroidal dynamics of the system, which is sufficient for reasoning about contact stability and DCM error convergence. However, computing the desired joint torques requires modeling the full system dynamics. We consider the dynamic model of a robot with a free-floating base and n torque-controlled joints, with joint angles denoted by $\boldsymbol{q} \in \mathbb{R}^n$. Let $\boldsymbol{x} \in \mathbb{R}^3$ represent the position of the CoM frame $\mathcal{C}$, and let $\boldsymbol{R}_b \in SO(3)$ denote the orientation of the base frame $\mathcal{B}$ relative to the world frame $\mathcal{W}$. The corresponding linear and angular velocities, $\dot{\boldsymbol{x}} \in \mathbb{R}^3$ and $\boldsymbol{\omega}_b \in \mathbb{R}^3$, are stacked to form the velocity vector $\boldsymbol{\nu}_c = (\dot{\boldsymbol{x}}^T, \boldsymbol{\omega}_b^T)^T$. The total number of degrees of freedom of the system is $\bar{n} = n + 6$.

The dynamics of the robot can be written as

$$\boldsymbol{M}\ddot{\boldsymbol{q}}_c + \boldsymbol{C}\dot{\boldsymbol{q}}_c + \boldsymbol{g}_c = \boldsymbol{S}^T\boldsymbol{\tau} + \boldsymbol{\tau}^{ext} \tag{85}$$

with $\dot{\boldsymbol{q}}_c = (\boldsymbol{\nu}_c^T, \dot{\boldsymbol{q}}^T)^T$, and $\boldsymbol{M} \in \mathbb{R}^{\bar{n}\times\bar{n}}$ and $\boldsymbol{C} \in \mathbb{R}^{\bar{n}\times\bar{n}}$ being the inertia and Coriolis/centrifugal matrices, respectively. The gravity vector is denoted by $\boldsymbol{g}_c = (-m\boldsymbol{g}^T, \boldsymbol{0}_{n+3}^T)^T \in \mathbb{R}^{\bar{n}}$. The joint torques of the actuators are indicated by $\boldsymbol{\tau} \in \mathbb{R}^n$, and the selection matrix $\boldsymbol{S} = [\boldsymbol{0}_{n\times 6}, \boldsymbol{I}_{n\times n}] \in \mathbb{R}^{n\times\bar{n}}$ accounts for the unactuated base. The generalized external forces acting on the system are represented by $\boldsymbol{\tau}^{ext} \in \mathbb{R}^{\bar{n}}$.

Linking to the centroidal dynamics in (1), we introduce the generalized momentum $\boldsymbol{h}_c = (\boldsymbol{p}_c^T, \boldsymbol{l}_c^T)^T$ as

$$\boldsymbol{h}_c = \boldsymbol{M}_c\dot{\boldsymbol{q}}_c \tag{86}$$

with $\boldsymbol{M}_c \in \mathbb{R}^{6\times\bar{n}}$ being the upper six rows of $\boldsymbol{M}$. Note that $\boldsymbol{M}_c$ is analogous to the centroidal momentum matrix (Orin and Goswami 2008). The centroidal angular momentum (CAM) $\boldsymbol{l}_c$ is obtained by expanding (86) to

$$\boldsymbol{l}_c = \boldsymbol{M}_\omega\dot{\boldsymbol{q}}_c, \tag{87}$$

where $\boldsymbol{M}_\omega \in \mathbb{R}^{3\times\bar{n}}$ corresponds to the lower three rows of $\boldsymbol{M}_c$.

C.2. Task-space Definitions

An operational task space with r tasks is introduced. The corresponding coordinates $\boldsymbol{x}_k \in \mathbb{R}^{m_k}$ are defined with the respective task dimensions m_k for $k = 1, \dots, r$. The task-space velocities are defined as

$$\dot{\boldsymbol{x}}_k = \boldsymbol{J}_k\dot{\boldsymbol{q}}_c, \tag{88}$$

where $\boldsymbol{J}_k \in \mathbb{R}^{m_k\times\bar{n}}$ is the Jacobian of the k-th task. Following the work of Dietrich and Ott (2020), the two assumptions are made regarding the definition of the task space: (i) all tasks are feasible, and the total task dimensions equal the number of DoF of the system

$$\sum_{k=1}^{r} m_k = \bar{n}, \tag{89}$$

and (ii) the examined workspace contains no singular configurations. The final task-space velocity vector $\dot{\boldsymbol{x}}_{task}$ and Jacobian $\boldsymbol{J}_{task}$ are obtained by stacking the individual task velocities and Jacobians:

$$\underbrace{\begin{pmatrix} \dot{\boldsymbol{x}}_1 \\ \vdots \\ \dot{\boldsymbol{x}}_r \end{pmatrix}}_{\dot{\boldsymbol{x}}_{task}} = \underbrace{\begin{pmatrix} \boldsymbol{J}_1 \\ \vdots \\ \boldsymbol{J}_r \end{pmatrix}}_{\boldsymbol{J}_{task}} \dot{\boldsymbol{q}}_c. \tag{90}$$

Under the task-space definition assumptions (i) and (ii), $\boldsymbol{J}_{task}$ is invertible throughout the examined workspace.

The selection of the task space can vary depending on the application scenario; however, some tasks are considered predefined in the field of legged robots, as presented by Mesesan et al. (2019). For example, a 6-DoF CoM tracking task is essential for maintaining balance in the context of legged locomotion:

$$\boldsymbol{\nu}_c = \underbrace{\begin{bmatrix} \boldsymbol{I}_{6\times 6} & \boldsymbol{0}_{6\times n} \end{bmatrix}}_{\boldsymbol{J}_c} \dot{\boldsymbol{q}}_c. \tag{91}$$

Another key objective of legged systems is the generation of contact wrenches between the system and the environment, which is formulated as an end-effector task. The task-relevant contact points are typically selected at the robot's feet or hands. The corresponding task-space velocities are defined as follows:

$$\boldsymbol{\nu}_{grf} = \underbrace{\begin{bmatrix} \boldsymbol{J}_{grf,c} & \boldsymbol{J}_{grf,q} \end{bmatrix}}_{\boldsymbol{J}_{grf}} \dot{\boldsymbol{q}}_c \tag{92}$$

with $\boldsymbol{\nu}_{grf} \in \mathbb{R}^{m_{grf}}$ containing the translational and rotational end-effector velocities, and the Jacobians $\boldsymbol{J}_{grf,c} \in \mathbb{R}^{m_{grf}\times 6}$, and $\boldsymbol{J}_{grf,q} \in \mathbb{R}^{m_{grf}\times n}$. Note that the task dimension m_{grf} depends on the contact configuration.

The remaining DoF are formulated as a generalized impedance task of dimension $m_{imp} = n - m_{grf}$. The corresponding task velocities are defined as

$$\dot{\boldsymbol{x}}_{imp} = \underbrace{\begin{bmatrix} \boldsymbol{J}_{imp,c} & \boldsymbol{J}_{imp,q} \end{bmatrix}}_{\boldsymbol{J}_{imp}} \dot{\boldsymbol{q}}_c \tag{93}$$

with $\dot{\boldsymbol{x}}_{imp} \in \mathbb{R}^{m_{imp}}$, $\boldsymbol{J}_{imp,c} \in \mathbb{R}^{m_{imp}\times 6}$, and $\boldsymbol{J}_{imp,q} \in \mathbb{R}^{m_{imp}\times n}$. This task may include Cartesian tracking of end effectors not in contact with the environment, such as the swing leg during walking or joint-space tasks. In the latter case, the corresponding Jacobian simplifies to $\boldsymbol{J}_{imp,c} = \boldsymbol{0}_{m_{imp}\times 6}$ and $\boldsymbol{J}_{imp,q} = \boldsymbol{S}_{imp}$, where $\boldsymbol{S}_{imp}$ is a joint selection matrix.

C.3. Desired CoM Wrench

The main idea of the passivity-based whole-body controller is to formulate a desired CoM wrench and distribute it among the end effectors in contact with the environment. Inspired by a PD+ control structure (Paden and Panja 1988), the desired CoM wrench is composed of pseudo-feedforward, impedance, and gravity-compensation terms. The linear CoM force is computed from the commanded eCMP (74)

$$\boldsymbol{f}_c^{cmd} = \frac{m}{b^2}(\boldsymbol{x} - \boldsymbol{e}^{cmd}). \tag{94}$$

For clarity, we introduce the subscript "c" to denote the CoM wrench, extending the notation used in Section 2.

As shown by Englsberger (2016) and Mesesan et al. (2019), the DCM controller implements a CoM tracking task using a PD+ control scheme with gravity compensation for a certain gain coupling based on the DCM control gain.

The rotational component of the desired CoM wrench is generated by a base orientation tracking controller, which consists of a pseudo-feedforward and an impedance term:

$$\boldsymbol{\tau}_c^{cmd} = \boldsymbol{\tau}_c^{ff} + \boldsymbol{\tau}_c^{imp}. \tag{95}$$

The feedforward term is computed from the desired task velocities and accelerations. By substituting the joint-space coordinates in (85) with task-space coordinates obtained via inverse kinematics, and selecting rows four to six corresponding to the angular velocity of the base, we obtain

$$\boldsymbol{\tau}_c^{ff} = \boldsymbol{M}_\omega^* \ddot{\boldsymbol{x}}_{task}^d + \boldsymbol{C}_\omega^* \dot{\boldsymbol{x}}_{task}^d \tag{96}$$

with $\boldsymbol{M}_\omega^* = \boldsymbol{M}_\omega \boldsymbol{J}_{task}^{-1}$ and $\boldsymbol{C}_\omega^* = \boldsymbol{M}_\omega \dot{\boldsymbol{J}}_{task}^{-1} + \boldsymbol{C}_\omega \boldsymbol{J}_{task}^{-1}$. The impedance terms ensure tracking of the base orientation and rotational velocity

$$\boldsymbol{\tau}_c^{imp} = \boldsymbol{\tau}_r(\boldsymbol{\Sigma}_b, (\boldsymbol{R}_b^d)^T \boldsymbol{R}_b) + \boldsymbol{B}_b \Delta\boldsymbol{\omega}_b \tag{97}$$

with $\Delta\boldsymbol{\omega}_b = \boldsymbol{\omega}_b - \boldsymbol{\omega}_b^d$. The rotational stiffness matrix $\boldsymbol{\Sigma}_b \in \mathbb{R}^{3\times3}$ and the rotational damping matrix $\boldsymbol{B}_b \in \mathbb{R}^{3\times3}$ are both symmetric and positive definite. The Cartesian orientation of the hip is controlled by the term $\boldsymbol{\tau}_r(\boldsymbol{\Sigma}_b, (\boldsymbol{R}_b^d)^T \boldsymbol{R}_b)$ (Ott et al. 2011), which emulates a rotational spring.

The contact wrenches associated with the end-effector task for generating ground reaction forces, which are intended to sum up to the CoM wrench, are denoted as $\boldsymbol{w}_{grf} \in \mathbb{R}^{m_{grf}}$. To improve readability, we add the subscript "grf" to the notation introduced in Section 2.1. The generalized forces resulting from the impedance task $\boldsymbol{f}_{imp} \in \mathbb{R}^{m_{imp}}$ are computed based on the deviation of the system from its reference. Wrenches corresponding to Cartesian tracking tasks are realized through a Cartesian impedance formulation, whereas joint-space tasks are implemented using a joint-space impedance.

C.4. Optimization Problem Formulation

We propose a formulation for the constrained QP, which simultaneously solves the wrench distribution problem of the passivity-based whole-body controller and a kinematic-based task optimization at the desired trajectory level.

The kinematic optimization provides the flexibility to formulate conflicting tasks by optimizing the desired task-space accelerations $\ddot{\boldsymbol{x}}_{task}^d$ when required. Compared to the original passivity-based whole-body controller (Henze et al. 2016; Mesesan et al. 2019), this approach enables the QP to modify a selected subset of the desired task-space accelerations to achieve its optimization goals, for example, generating angular momentum through upper-body motion to realize the desired CoM force. Optimizing in task space has the advantage that a subset of the task-space variables can be excluded from the optimization, for example, the Cartesian trajectories of the end effectors in contact with the environment, without the necessity of adding additional kinematic constraints.

The optimization variables are the contact wrenches $\boldsymbol{w}_{grf}^{opt}$, and the task accelerations $\ddot{\boldsymbol{x}}_{task}^{opt}$. The tasks are formulated as residuals $\boldsymbol{\delta}_j \in \mathbb{R}^{n_j}$, where n_j denotes the dimension of the j-th optimization task and j is an element of the stack of tasks (SOT). The prioritization among the tasks is determined by the individual task weighting matrices $\boldsymbol{Q}_j \in \mathbb{R}^{n_j\times n_j}$, which must be symmetric and positive definite. The resulting QP formulation is defined as follows:

$$\min_{\boldsymbol{w}_{grf}^{opt}, \ddot{\boldsymbol{x}}_{task}^{opt}} \sum_{j\in\text{SOT}} \frac{1}{2}\boldsymbol{\delta}_j^T \boldsymbol{Q}_j \boldsymbol{\delta}_j. \tag{98}$$

The QP is solved subject to the contact constraints formulated in Section 2.2, as well as kinematic and dynamic constraints in joint and task space. In the following, we present the stack of tasks optimized in the QP.

C.4.1. CoM Task. The CoM task ensures that the sum of CoM-mapped contact wrenches matches the commanded CoM wrench:

$$\boldsymbol{\delta}_c = \begin{pmatrix} \boldsymbol{f}_c^{cmd} \\ \boldsymbol{\tau}_c^{cmd} \end{pmatrix} - \begin{bmatrix} \boldsymbol{J}_{grf,c}^T & \boldsymbol{J}_{imp,c}^T \end{bmatrix} \begin{pmatrix} \boldsymbol{w}_{grf}^{opt} \\ \boldsymbol{f}_{imp} \end{pmatrix}. \tag{99}$$

The feedforward terms in the desired CoM wrench provide the coupling between the wrench distribution problem and the kinematics-based optimization. The QP can adjust the desired task acceleration to support tracking of the desired CoM wrench.

C.4.2. Contact Wrench Task. An additional task is introduced, which aims to generate the desired contact wrenches $\boldsymbol{w}_{grf}^d$, as provided by a high-level planner:

$$\boldsymbol{\delta}_w = \boldsymbol{w}_{grf}^{opt} - \boldsymbol{w}_{grf}^d. \tag{100}$$

In most cases, $\boldsymbol{w}_{grf}^d$ is chosen to be zero, thereby simplifying the task to a pure regulation problem that minimizes the Euclidean norm of the contact wrenches (Ott et al. 2011; Henze et al. 2016; Mesesan et al. 2019).

C.4.3. Reference Acceleration Task. This task tracks a reference acceleration for the task-space coordinates adjusted within the optimization:

$$\boldsymbol{\delta}_x = \ddot{\boldsymbol{x}}_{task}^{opt} - \ddot{\boldsymbol{x}}_{task}^{ref}. \tag{101}$$

The reference acceleration ensures that the optimized trajectory returns to the desired one. It is defined as

$$\ddot{\boldsymbol{x}}_{task}^{ref} = \ddot{\boldsymbol{x}}_{task}^d - \boldsymbol{D}_x(\dot{\boldsymbol{x}}_{task}^{opt} - \dot{\boldsymbol{x}}_{task}^d) - \boldsymbol{K}_x(\boldsymbol{x}_{task}^{opt} - \boldsymbol{x}_{task}^d), \tag{102}$$

where $\boldsymbol{D}_x \in \mathbb{R}^{\bar{n}\times\bar{n}}$ and $\boldsymbol{K}_x \in \mathbb{R}^{\bar{n}\times\bar{n}}$ are diagonal and positive definite.

C.4.4. Angular Momentum Task. Angular momentum plays a crucial role in humanoid locomotion, for example, during walking and disturbance reactions. Since the planner generates desired whole-body trajectories without considering multi-body dynamics, the resulting trajectories may not be consistent with a desired CAM objective, such as regulating the rate of change of the CAM to zero during walking. By reformulating (87) in task-space coordinates and taking the time derivative, we obtain

$$\dot{\boldsymbol{l}}_c = \boldsymbol{M}_\omega^* \ddot{\boldsymbol{x}}_{task} + \dot{\boldsymbol{M}}_\omega^* \dot{\boldsymbol{x}}_{task} \tag{103}$$

with $\boldsymbol{M}_{\omega}^{*} = \boldsymbol{M}_{\omega}\boldsymbol{J}_{task}^{-1}$ and $\dot{\boldsymbol{M}}_{\omega}^{*} = \boldsymbol{M}_{\omega}\dot{\boldsymbol{J}}_{task}^{-1} + \dot{\boldsymbol{M}}_{\omega}\boldsymbol{J}_{task}^{-1}$. The angular momentum task is formulated as the residual

$$\boldsymbol{\delta}_l = \dot{\boldsymbol{l}}_c^{opt} - \dot{\boldsymbol{l}}_c^{ref} \tag{104}$$

and the rate of change of the CAM of the optimized trajectories is computed as

$$\dot{\boldsymbol{l}}_c^{opt} = \boldsymbol{M}_{\omega}^{*}\ddot{\boldsymbol{x}}_{task}^{opt} + \dot{\boldsymbol{M}}_{\omega}^{*}\dot{\boldsymbol{x}}_{task}^{opt}. \tag{105}$$

The reference rate of change of CAM is designed to track the desired CAM $\boldsymbol{l}_c^d$ provided by a high-level planner:

$$\dot{\boldsymbol{l}}_c^{ref} = \dot{\boldsymbol{l}}_c^{d} - \boldsymbol{K}_l\left(\boldsymbol{M}_{\omega}^{*}\dot{\boldsymbol{x}}_{task}^{opt} - \boldsymbol{l}_c^d\right). \tag{106}$$

Here, $\boldsymbol{K}_l \in \mathbb{R}^{3\times3}$ is diagonal and positive definite.

C.5. *Torque Computation*

After solving the constrained QP (98), the control torques commanded to the system are computed based on the optimized contact wrenches and task accelerations. Based on the lower n rows of the system dynamics (85) and by applying (90), we obtain

$$\boldsymbol{\tau} = \boldsymbol{M}_q^{*}\ddot{\boldsymbol{x}}_{task}^{opt} + \boldsymbol{C}_q^{*}\dot{\boldsymbol{x}}_{task}^{opt} - \begin{bmatrix} \boldsymbol{J}_{grf,q}^T & \boldsymbol{J}_{imp,q}^T \end{bmatrix} \begin{pmatrix} \boldsymbol{w}_{grf}^{opt} \\ \boldsymbol{f}_{imp} \end{pmatrix} \tag{107}$$

with $\boldsymbol{M}_q^{*} = \boldsymbol{M}_q\boldsymbol{J}_{task}^{-1}$ and $\boldsymbol{C}_q^{*} = \boldsymbol{M}_q\dot{\boldsymbol{J}}_{task}^{-1} + \boldsymbol{C}_q\boldsymbol{J}_{task}^{-1}$.

C.6. *Implementation Details*

The whole-body controller formulation enables kinematic-level optimization over a subset of task-space accelerations. The selection of this subset depends on the contact configuration and high-level task objectives.

In the context of reactive legged locomotion, end effectors that are constrained to maintain or establish contact with the environment are excluded from the optimization variables. Since eCMP tracking has the highest priority in humanoid locomotion, we aim to prevent the whole-body controller from modifying the reference horizontal CoM acceleration in the case of conflicting tasks or constraints. Therefore, the horizontal CoM accelerations are excluded from the variables optimized within the QP.

The remaining task variables selected for optimization include the rotational accelerations of the base, the DoF of free end effectors, and the vertical CoM acceleration. The first two are used to induce angular momentum when necessary, thereby accounting for the hip strategy. The vertical CoM acceleration is directly related to the desired vertical eCMP through (14) and (18), and thus corresponds to the height-variation strategy. However, there is no strict separation between the strategies within the optimization. The QP identifies the best trade-off based on task weighting, as well as contact, kinematic, and dynamic constraints. In experiments #1, #2, and #3, the DoF of both arms are selected for optimization. In experiment #4, only the DoF of TORO's left arm are included in the optimization, while the right arm is used to generate contact forces with the environment. The rotational accelerations of the base and the vertical CoM acceleration are incorporated into the optimization in all experiments.

The different strategies are activated through the direction and magnitude of the commanded horizontal CoM force provided to the whole-body controller via the commanded eCMP. Tracking the commanded CoM force has the highest priority; therefore, the CoM task is assigned the highest weight in the stack of tasks in (98). This task is fulfilled as long as it does not conflict with the implemented constraints. At the second priority level are the rotational components of the CoM wrench and the centroidal angular momentum task. The lowest priority, next to the ground reaction force task, is the reference acceleration task. This task is the first to be sacrificed when the CoM force cannot be generated solely through modulating the ground reaction force. The corresponding weighting matrices satisfy the following relation: $\boldsymbol{Q}_{c,1:2} > \boldsymbol{Q}_{c,3} > \boldsymbol{Q}_{c,4:6}$, $\boldsymbol{Q}_l > \boldsymbol{Q}_x > \boldsymbol{Q}_w$. Note that the ratio between the hip and height-variation strategies, i.e., which strategy is used more extensively, can be influenced by the corresponding entries of $\boldsymbol{Q}_x$.